The characteristics of Titanium-nickel alloys produced by powder technology

Thesis

THE CHARACTERISTICS OF

TITANIUM-NICKEL ALLOYS PRODUCED BY POWDER TECHNOLOGY

A thesis submitted for the degree of

Doctor of Philosophy of

The Open University

by

Monday Igharo, MSc. (Birmingham)

Materials Science Discipline

The Open University

Author's number: HDM 66493

January, 1987

Date of submission: January 1987

Date of award: 7 March 1987

PREFACE

This thesis is submitted for the degree of Doctor of Philosophy of the Open University. It describes the research performed in the Materials Science Discipline between December 1983 and December 1986 under the supervision of Dr. J.V. Wood. Except where reference has been made to the work of other investigators, this work has been executed entirely by myself without collaboration. None of this work has been submitted for a degree or other qualifications at any other University or Institution.

Part of this work has been presented at three conferences (Powder Metallurgy Conference, October 1985 at Eastbourne; The 1985 Fall Meeting of the Materials Research Society, December 1985; and the Materials Week '86 Meeting of the ASM, Orlando, USA, October 1986) and published in the Conference Proceedings. Two reports have also been published in volumes 28 (1985) and 29 (1986) in 'Powder Metallurgy'.

M. Igharo,
Materials Science Discipline
The Open University,
January, 1987.

ACKNOWLEDGEMENTS

I would particularly like to express my gratitude to Dr. J.V. Wood for his invaluable guidance, supervision and constant encouragement throughout the course of this work.

My thanks are due to the research and technical staff of the Materials Science Discipline, especially Messrs Colin Gagg, Ian Norman and Gordon Imlach, and Mrs. Naomi Williams for their assistance in the use of equipment.

I would also like to thank Professors C.W.A. Newey and C.N. Reid for the provision of laboratory facilities.

I am grateful to Dr. Hayes of Inco International and Mr. Giddley of Deeside Titanium for providing the powders used in this investigation.

I gratefully acknowledge a research studentship by the Open University without which this work would not have been undertaken.

I would also like to thank Misses Boma Braide and Anita Stannard for typing this thesis.

Lastly, I must express my gratitude to my family for their never ending moral support.

ABSTRACT

A range of titanium-nickel alloys near the equiatomic composition have been processed by cold compaction and vacuum sintering. The effects of compaction pressure, sintering temperature and powder particle size on dimensional changes and densities of sintered compacts are presented. The influence of composition and heat treatment on microhardness and transformation temperature (M_s) is described.

During sintering, anisotropy of dimensional change occurs, with expansion in the radial and contraction in the axial direction of cylindrical compacts. Greater porosity is found in the sintered samples compared to that in the as-pressed condition. It is proposed that these observations are connected with the dissimilar interdiffusion rates of Ti and Ni, the segregation of powder particles in the green compacts and the occurrence of a transient liquid phase during sintering above 955°C. Subsequent hot isostatic pressing of the sintered material allows densification to near full density.

The transformation temperatures and hardness of TiNi alloys containing excess amounts of nickel (> 51 at -% Ni) are sensitive to cooling rate after solid state heat treatment, which is in contrast with samples of the exact equiatomic composition. This phenomenon has been related to the decrease in the homogeneity range of TiNi compound

with temperature, resulting in either the formation of second phase precipitates in the slow cooled samples or the production of a supersaturated structure in water quenched material.

The pressed and sintered specimens display a well defined shape memory behaviour. The extent of shape recovery observed, following deformation and heating through the reverse transformation range, is explained in terms of the volume of pores in the sintered compacts.

Ribbons of equiatomic TiNi alloy have been rapidly solidified by the chill block melt spinning technique under an argon atmosphere. The effects of rapid solidification processing and subsequent heat treatments on the transformation behaviour are presented. The crystal structures at room temperature have been analysed by X-ray powder diffraction and thin foil transmission electron microscopy. Some of the ribbons have been chopped and ball milled to produce prealloyed particulate from which compacts have been prepared by cold compaction followed by vacuum sintering. The consolidation response of the prealloyed powder is compared with that of elemental blends.

The grain size of the rapidly solidified material is found to be at least an order of magnitude smaller than those observed in wrought specimens. The M_s temperature of TiNi alloy is depressed by rapid solidification processing, thus allowing the R-phase to be observed in addition to the high temperature parent phase. This depression has been correlated with the fine grain structure of the spun ribbon.

Sintering temperatures in excess of those employed for elemental blends are required for the prealloyed particles. This is related to the dominant effect of the alloy formation energy in elemental powders sample. However, while the volume of porosity increases with sintering temperature in elemental mixture compacts, densification takes place in the case of RS prealloyed specimens. In spite of the need for a higher sintering temperature for RS prealloyed compacts, the resulting grain size is smaller.

CONTENTS

CHAPTER 4 POWDER METALLURGY PROCESSING

CHAPTER 5 RAPID SOLIDIFICATION PROCESSING

CHAPTER 6 EXPERIMENTAL DETAILS

CHAPTER 8 PROPERTIES OF SINTERED TiNi COMPACTS

CHAPTER 9 EFFECT OF RAPID SOLIDIFICATION PROCESSING ON THE PROPERTIES OF EQUIATOMIC TiNi ALLOY

CHAPTER 1

INTRODUCTION

The study of the shape memory effect (SME) has become a field of intensive research since its discovery in equiatomic TiNi alloy by Buehler and his associates[1] about 23 years ago. The phenomenon is such that when a specimen is deformed at a low temperature it regains its original shape on subsequent heating to a moderately high temperature. A detailed analysis of this behaviour has led to the recognition of the following two specific effects;

(i) Pseudoelasticity, where a sample which has been deformed beyond its apparent yield point isothermally restores its predeformed shape on removing the applied load.

(ii) A two-way memory in which a specimen shows a reversible dimensional change on both heating and cooling. (This will not be dealt with in the present work.)

Historically, although the SME has been popularised by the report on TiNi, the phenomenon was first observed by Chang and Read[2] in Au-Cd alloy in 1951 followed by a report on In-Tl system two years later[3]. The effect has now been observed in several alloy systems. Among these are Cu-Al-Ni[4], Cu-Zn[5], Cu-Al[6], Ni-Al[7], and Fe-Pt[8]. A common property of these alloys is that all undergo a crystallographically reversible, thermoelastic martensitic transformation on cooling from the high temperature phase. Most SME alloys have an ordered structure, the only exception being the

indium-thallium alloy[9]. Their martensites are either twinned or faulted[10].

In spite of the large number of alloy systems which show the SME, only TiNi and Cu-base alloys are available commercially. Among these two groups, TiNi alloys possess superior mechanical properties in terms of ductility and fatigue life, but because they are relatively expensive to process, their uses tend to be restricted to specialised applications such as the air craft hydraulic tube couplings described in Chapter 3.1. Cu-base alloys, by contrast, are used for more general applications[11] including traditional joining devices (for example, rivets, cotter pins), electrical and circuit connectors, and temperature sensing devices which activate electrical or mechanical systems at predetermined temperatures. This difference is mainly a result of the high cost of fabricating titanium alloys by conventional methods. Thus unless an alternative cost effective route is established, TiNi alloys cannot be employed to their full advantage.

The process of powder metallurgy (P/M) offers the potential for producing near-net shapes with reduced processing costs. Another technique which is capable of producing fine grain materials in the form of wire, ribbon or powder directly from the molten state, thereby reducing the production steps and costs is rapid solidification. The manufacture of TiNi alloys by these methods has not been investigated in detail.

The purpose of the present research was to study the characteristics of some TiNi shape memory alloys prepared by both rapid solidification and powder metallurgy techniques. The properties studied are microstructure, transformation behaviour, mechanical properties and consolidation response.

As the shape memory behaviour is normally associated with a reversible martensitic reaction, a knowledge of the characteristics of this type of transformation is of fundamental importance when dealing with shape memory alloys. Hence in Chapter 2 a review of previous work on the properties of thermoelastic martensitic phase changesis presented. The phase transition, crystal structures, and other transformation phenomena of titanium-nickel of approximately equiatomic concentration are examined in Chapter 3.

Chapter 4 considers the relevant technology of powder metallurgy, and summarises the results of earlier theoretical and experimental studies on the mechanism of compaction and sintering of metal powders. In Chapter 5 the topics of rapid solidification which are specific to the present study on crystalline material are summarised. This has been done under the three headings of Principles, Effects and Consolidation.

Experimental techniques of specimen preparation and characterisation in the present work are described in Chapter 6. The results of an investigation involving the compaction and sintering of Ti-Ni elemental powders are presented in Chapters 7 and 8. Chapter 9

describes the results of a detailed study of the effect of rapid solidification on the properties of equiatomic TiNi alloy. In addition, the consolidation behaviour of the solidified material is compared with that of elemental blends.

Chapter 10 lists the main conclusions deduced from the results of this research and indicates possible directions of future work.

CHAPTER 2

FUNDAMENTALS OF THE MARTENSITIC TRANSFORMATION

?.1 Introduction

It is generally recognised that the essence of the shape memory behaviour depends upon an alloy's ability to undergo a thermoelastic martensitic reaction. The effect is observed when a material is deformed in the martensitic condition followed by heating into a high temperature phase field. In this chapter, the character of the transformation for thermoelastic martensites is considered.

2.2 The Martensitic Transformation

The term martensitic transformation refers to any solid state phase change in which the growth of the transition product (called martensite) occurs by the systematic co-ordinated movement of atoms of the parent phase. The distance through which individual atoms moves being less than one lattice spacing[12]. The neighbours of any given atom are the same in the final structure as in the original configuration except that the relative positions are different. Thus, if the parent phase is ordered, the final structure is also ordered, but because there is a change of lattice, the volume and shape of the transformed material is different. The total shape change of the crystal lattice is assumed to be equivalent to an invariant plane strain consisting of a pure shear occurring parallel to the habit (or

twinning) plane and contraction or expansion normal to this plane. An invariant plane strain is one in which all lattice points in the object move in the same direction through distances proportional to their separation from some fixed plane. The martensite plates formed in a parent crystal lie parallel to a crystallographic plane of high indices, called the habit plane (for example $\{225\}_\gamma$ in high carbon steels)[12].

2.3 Driving Force for the Martensitic Transition

The phase transition is caused by the difference between the free energies of the two structures in the system. Since there is no composition change involved, an alloy undergoing the transformation is thermodynamically considered as a single component system. Hence, the free energies of the parent (p) and martensite (m) phases are usually represented as shown in Figure 2.1[13].

T_o is the equilibrium temperature at which the free energies of the two phases are equal.

Cooling below T_o is necessary before the formation of martensite is thermodynamically possible, since only then is the chemical driving force for the reaction p→m given by

$$\Delta G_c^{p\rightarrow m} = G^m - G^p \qquad 2.1$$

is negative. The net free energy change is always less than $\Delta G_c^{p\rightarrow m}$ because the interfacial energy associated with the formation of

a martensite nucleus, and the elastic strain energy associated with the shape change and the constraints of the surrounding parent matrix, absorb a proportion of the free energy released by the transformation[12]. Under this condition of resistive energy, the net free energy ΔW is given by[14]:

$$\Delta W = \Delta G_c^{p\to m} + \Delta G_{nc}^{p\to m} \qquad 2.2$$

where $\Delta G_{nc}^{p\to m}$ is the non-chemical energy term representing all the opposing forces. Thus, some degree of undercooling, ΔT ($\Delta T = T_o - M_s$) is necessary to give enough driving force to initiate the phase change. M_s is the temperature to which the alloy must be cooled for the start of martensite formation.

At temperatures above M_s, martensite may also be formed by the application of external stress. This is because the mechanical work given by the product of the applied stress and the corresponding strain associated with the transition helps to counteract the effect of the internal stress, thereby making it possible to attain the critical driving force for nucleating martensite at temperature above M_s[15]. Hence, apart from M_s, martensitic alloys are characterised by other parameters such as:

M_f, the temperature at which martensite formation ends;

M_d, the highest temperature at which martensite can be induced by the application of stress;

A_s, A_f and A_d, the respective temperatures corresponding to M_s, M_f and M_d during the reverse transformation from martensite to the high temperature parent phase; and

T_o, the equilibrium temperature already defined.

The relationships between these factors are presented in Figure 2.2[16]. The figure is a schematic representation of the variation of the amount of martensite with temperature in the absence of stress. The exact position of A_d relative to other parameters is not known. Its existence is only based on the hypothesis that since the forward transformation to martensite is assisted by the application of stress, by analogy, the reverse reaction must also be affected by applying stress[17].

The location of T_o has been studied, by many investigators (e.g. Refs. 18, 19). In the case of the "burst" type of martensitic transformation, to be considered in Section 2.4.1, the stored elastic strain energy is insignificant and both the forward and the reverse transition require different nucleation sites. For example, an initial Fe-Ni single crystal of the high temperature phase becomes polycrystalline after the subsequent forward and the reverse transformation[9]. Thus, A_s is greater than M_s and T_o is usually placed half way between M_s and A_s[18]. However, in the thermoelastic reaction, which will be discussed in section 2.4.2, the transformation shape change is accommodated elastically and the build-up of elastic strain energy can influence the transition temperatures by assisting

the chemical driving force for the reverse transformation. Tong and Wayman[19] have found that A_s may be lower than M_s as shown in Figure 2.2. Consequently, Tong, and Wayman, proposed that T_o can be estimated from

$$T_o = \frac{1}{2}(M_s + A_f) \qquad 2.3$$

where $M_s < A_f$

This equation is based on the assumption that the stored elastic energy has no significant effect on the net free energy required to nucleate the first plate of martensite at M_s; thus, M_s must be lower than T_o. It is also assumed that the influence of the elastic strain field on the last martensite plate to revert to the parent phase at A_f is negligible compared with that encountered by those formed earlier. Further characteristics of martensitic reaction will be reviewed in the next section.

2.4 Characteristics of the Martensitic Transformation

When an alloy which is capable of forming martensite is cooled to the M_s temperature in the absence of applied stress, the reaction may take place isothermally or athermally. The isothermal case, in which the formation of martensite proceeds at a constant temperature, is not relevant to the present study and will not be discussed further. Athermal transition occurs only after cooling below M_s. The total amount of martensite formed being a function of the

temperature to which the specimen is cooled. There are two types of athermal transformation: spontaneous (or burst) and thermoelastic. Each will now be considered in turn.

2.4.1 The Spontaneous or Burst Reaction

The phase change is said to be a spontaneous or burst if during the transition the chemical driving force considerably exceeds the opposing energy. This situation arises in alloy systems in which there is ample resistance to the formation of nuclei[12]. High undercoolings (typically 100 - 200 K as compared with 5 - 50 K for thermoelastic martensites)[20] are required. Once an active nucleus exists it grows rapidly to a full size martensite plate at a velocity approaching the speed of sound. Using resistivity changes to monitor the growth of individual plates of martensite, in for example Fe - Ni alloys, speeds of 800 to 1100 ms^{-1} have been measured[21]. The rate of reaction depends on the number of nuclei and the size of the martensite plate and is not determined by the cooling rate. In view of the large driving force involved, the shape strain accompanying the reaction is sufficient to cause plastic deformation during the growth process. Accordingly, the parent/martensite interface becomes disrupted by the debris resulting from plastic yielding, the interface loses its coherency and the interfacial motions are not reversible[22]. The martensites of most ferrous alloys, which do not display the SME, are formed by the burst type of reaction. In addition to a high undercooling and substantial shape change, (about 4%), this transition is characterised by a large hysteresis (A_s - M_s). For

example, in Fe - 30%Ni alloy the temperature hysteresis is of the order of 400 K[12]. Thermal hysteresis and the degree of undercooling are measures of the ease with which martensite formation can be initiated.

2.4.2 The Thermoelastic Reaction

In the thermoelastic transformation, a given plate of martensite forms and grows continuously as the temperature is lowered and shrinks by the exact reverse path as the temperature is raised. The rate of growth and shrinkage being dependent on the rate of temperature change[13]. This nature of thermoelastic reaction was first reported in 1949 by Kurdjumov and Khandros[23] in Cu-base alloys. They also found that the plate of martensite which formed first was the last to revert to the parent phase during the reverse transformation. At any temperature during cooling below M_s the growth of martensite proceeds until the strain energy generated is in equilibrium with the chemical driving force, when growth ceases. On further cooling, additional free energy is available, allowing growth of the plate to continue until another equilibrium point is reached.

The formation of thermoelastic martensite is associated with small undercoolings, ΔT (where $\Delta T = T_o - M_s$) as previously indicated. This means that the driving force for the transformation is low, since the function $G^{p \rightarrow m}$ varies with the undercooling according to[24]:

$$\Delta G^{p \to m} = \Delta H^{p \to m} \frac{(T_o - M_s)}{T_o} \qquad 2.4$$

where $\Delta H^{p \to m}$ is the enthalpy of transformation. This is consistent with experimental observations. For example, in TiNi equiatomic alloy, $\Delta G^{p \to m}$ has been found to be about 92 J mole^{-1}, which is significantly lower than the value (840 J mole^{-1}) obtained in "burst" martensites, such as Fe-28%Ni[24]. The reason for the relatively small driving force in this reaction is not clear. A popular view is that it is due to the nucleation of martensite in a soft lattice. An anomalous decrease in the shear elastic constant of the parent phase near the M_s has been reported for all shape memory alloys[25,26]. The values found in thermoelastic alloys are about an order of magnitude lower (about 10 GPa) than those of alloys which exhibit the "burst" reaction (about 100 GPa)[20]. Since this measures the resistance to deformation when a shearing stress is applied across a (110) plane in a [110] direction[20,25,26], it is supposed that a low value can allow transformation deformation to take place in the {110} <110> system at a small driving force. The thermal hysteresis is also considerably smaller (typically 4 - 35 K)[9] than for the burst type of transformation (e.g. 400 K for Fe - 30%Ni alloy). In addition, the shape change involved in the thermoelastic transition is about 0.4 per cent, which is significantly less than those for steels (about 4%) displaying the burst type of reaction[9], and so can be elastically accommodated[13,22]. Consequently, the martensite/parent matrix interface remains coherent and the interfacial motions are reversible. As pointed out earlier, all SME alloys transform by this process.

On account of the small driving force for the transition, the stress necessary to nucleate martensite is accordingly low and thermoelastic martensite can be easily formed by the application of external stress. In the case of the burst reaction, extensive plastic deformation of the parent phase occurs before the applied stress reaches a level sufficient to promote the phase change. As will be discussed in the next section on stress induced transitions, the essential condition for the occurrence of SME is that no plastic deformation should be involved in the transformation process[25].

2.4.3 Thermomechanical Behaviour

When a thermoelastic alloy is subjected to an external stress, the deformation modes largely depend on the test temperature. A typical single crystal tensile plot for a specimen tested above A_f is shown in Figure 2.3[13]. The initial linear section OA represents elastic deformation of the parent phase. At point A, stress induced martensite (SIM) begins to form under an applied stress $\sigma_{p \to m}$ and complete transformation is achieved at B. Although there are 24 possible martensitic variants, only the one whose shape strain provides maximum extension in the direction of the tensile axis is favoured by the applied stress[27,28]. Further stressing causes elastic deformation of the SIM along BC followed by plastic yielding until fracture occurs. C is the yield point of the material. However, if the stress is released before reaching C (say at point B'), there is first an elastic unloading of the martensite (B'D), followed by a reversion of the SIM to the parent matrix phase (DE) and finally

elastic recovery of the matrix phase (EF). Thus, the material essentially regains its original shape. This behaviour is termed pseudoelasticity. If the specimen is loaded beyond C, irreversible plastic deformation (slip yielding) of the martensite will prevent complete shape recovery[25].

The stress required to induce martensite, $\sigma_{p \rightarrow m}$ increases with temperature (Figure 2.4)[27] because of the increasing stability of the parent phase as the temperature is raised above M_s. The highest temperature above which martensite cannot be formed by stress is defined as M_d. It is the temperature at which $\sigma_{p \rightarrow m}$ is equal to the yield strength of the material. At higher temperatures, plastic deformation of the parent matrix occurs before $\sigma_{p \rightarrow m}$ is reached. An approximate relationship between $\sigma_{p \rightarrow m}$ and temperature can be expressed by a modified form of the Clausius-Clapeyron formula applicable to stress induced martensite[13,29].

$$\frac{d\sigma_{p \rightarrow m}}{dT} = \frac{\rho \Delta H}{\varepsilon_t T_o} \qquad 2.5$$

where:

$\frac{d\sigma_{p \rightarrow m}}{dT}$ - the temperature coefficient of the critical stress for the transformation and can be obtained from the slope of curve AB in Figure 2.4;

ΔH - the heat of transformation;

ε_t - the total macroscopic strain due to transformation;

ρ - the density of the material.

This equation is based on a balance between the mechanical work involved in the process and the volume free energy of transformation. It neglects any hysteresis in the stress-strain curve and assumes that both the matrix and martensite phases are always in equilibrium. Takei et al[30] have used this equation to determine ΔH for Ti-Ni alloys. Their results are found to be close to those obtained by specific heat measurements.

When a thermoelastic specimen is cooled to a temperature between M_s and M_f, the structure will consist of thermal martensite and a parent phase which can be transformed by applying external stress. Upon unloading, the SIM produced will remain stable because the initial residual matrix phase is in a metastable state. The typical single crystal tensile curve for an alloy deformed at temperature between M_s and M_f is shown in Figure 2.5. Section OABC results from[27,31]:

(i) the growth of the most favourably oriented existing thermal martensite variant at the expense of other variants and retained parent phase;

(ii) re-orientation of the existing martensite; and

(iii) movement of internal twin boundaries or stacking fault partial dislocations.

On release of the stress, some elastic recovery takes place (CD). If the sample is heated between A_s and A_f, complete recovery of the remaining strain (DO) occurs by reverse transformation and re-orientation to the original grain structure. This is the shape memory effect (SME).

The SME can also be observed by loading the specimen at a temperature below M_f, the temperature at which martensitic transformation ends on cooling. In this case, the deformation modes are similar to those of specimen stressed at a temperature between M_s and M_f, except that the original structure is essentially thermal martensite[27]. As with the pseudoelasticity, a material which has been stressed into the plastic region will not completely recover the total strain. For example, Baker[32] has studied the influence of the initial deformation strain on the extent of shape recovery in titanium - 35% niobium alloy. His results show that the amount of recovery, on heating, decreases from 100 to 70 per cent by increasing the strain from 3.25 to 5 per cent. There is thus, a critical strain limit which if exceeded can lead to imperfect strain recovery. In the next and final section of this chapter the prerequisites for the shape recovery and some factors influencing the amount of recoverable strain will be considered.

2.4.4 Conditions for the Reversal of Shape Change

Although the precise mechanism for the shape memory phenomenon remains a controversial subject, the two conditions which must be satisfied if the total strain is to be recovered, on heating, are well established[9,22].

(i) Crystallographic reversibility must exist between the parent and the martensite phases, i.e. the reversion process restores the original orientation of the parent phase.

(ii) All the strain must be produced by deformation mechanisms which are reversible, i.e. no (slip) plastic deformation involved. This implies that the growth or re-orientation of martensite plates during cooling or application of external stress must cease before the elastic limit of the material is reached.

The crystallographic reversibility in thermoelastic alloys has been associated with the ordered structure of the materials. It is considered that ordering can limit the direction of atomic displacement during the reverse transformation so as to maintain the order configurations. For instance, Dunne and Wayman[14] have reported that atomic ordering changes the martensitic reaction in Fe-Pt alloys from the burst type to a slow growth thermoelastic form. It has also been suggested that ordering enhances thermoelastic behaviour by raising the elastic limit beyond which the material

deforms in an irreversible fashion[14,34]. Strengthening of shape memory alloys (e.g. TiNi) by prestraining in order to suppress the onset of plastic flow has also been found to be an effective method of improving the shape recovery[33].

It must be emphasised, however, that not all strengthening techniques are capable of enhancing the thermoelastic behaviour. For example, it has been found from a number of studies (e.g. Refs. 10,16,33) that a single crystal specimen has a higher recoverable strain limit compared with a polycrystalline material of the same alloy. This has been attributed to the predominance of irreversible plastic yield at grain boundaries which limits the recoverable strain during subsequent heating through the reverse transition range.

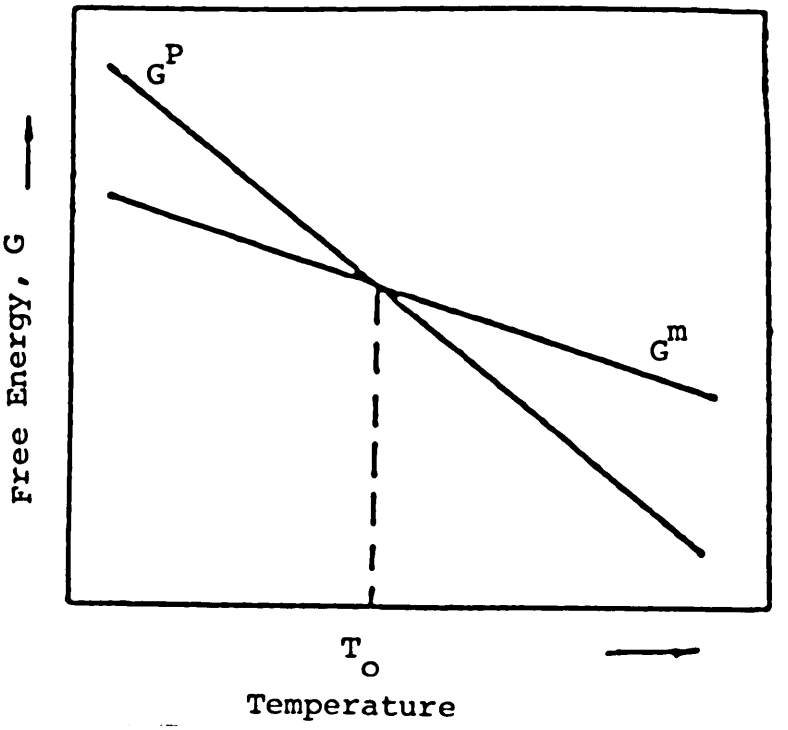

Figure 2.1 Temperature dependence of the free energies of the parent (p) and martensitic (m) phases[13].

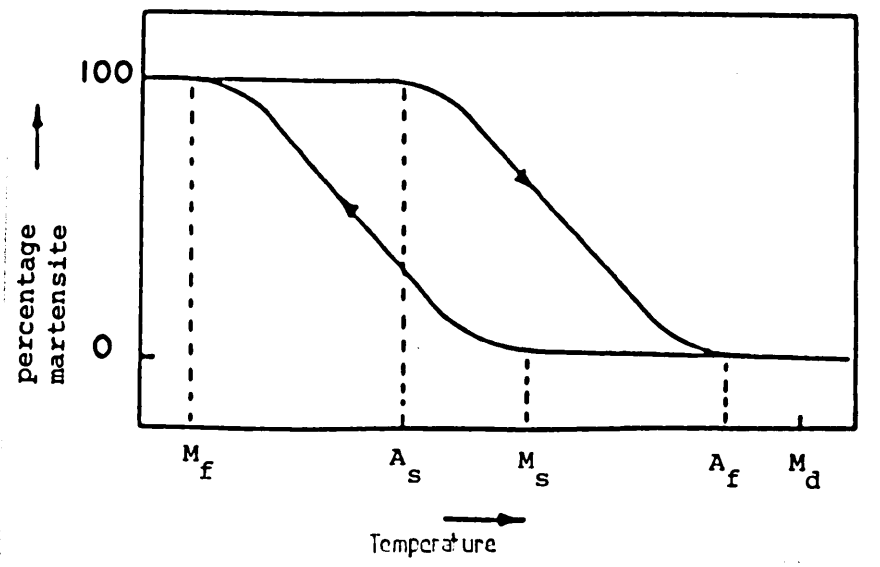

Figure 2.2 Schematic representation of the volume percentage of martensite as a function of temperature, showing transformation hysteresis loop[16].

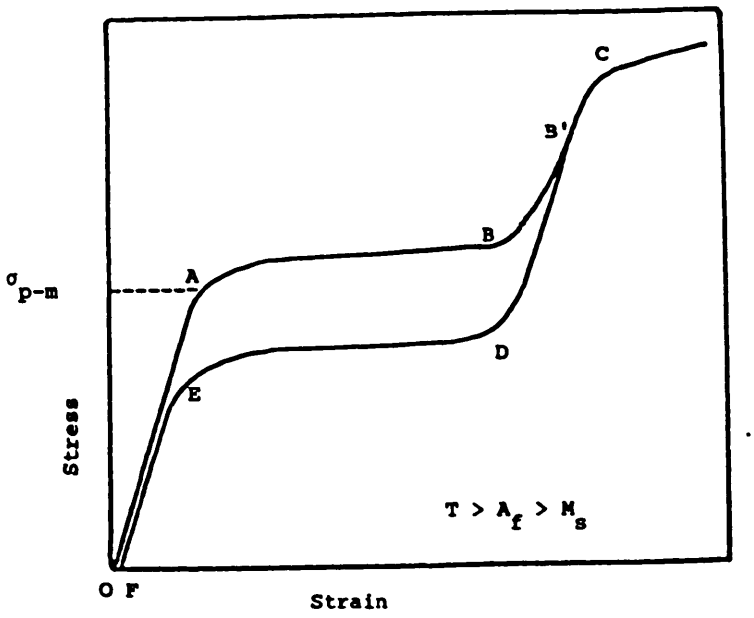

Figure 2.3 Typical stress-strain curve for alloy deformed at a temperature above A_f, showing pseudoelastic behaviour[13].

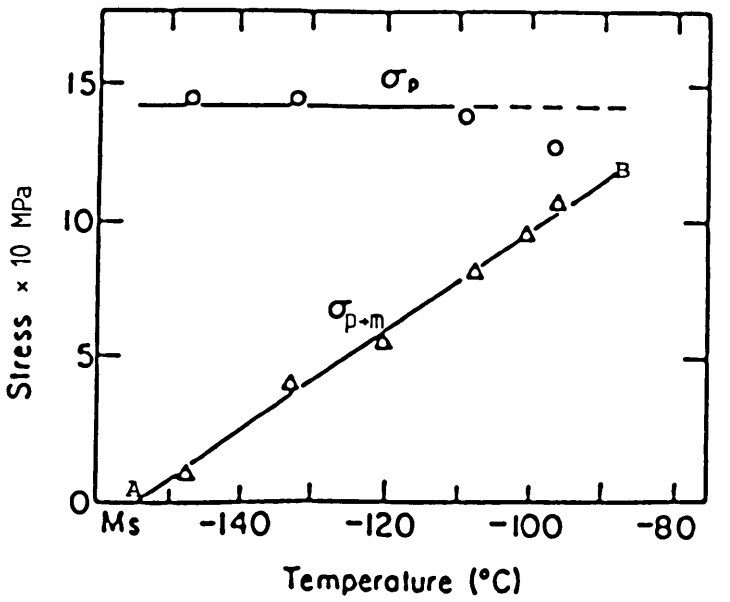

Figure 2.4 Variation of stress necessary to form martensite ($\sigma_{p\to m}$) and stress for plastic deformation of the matrix phase (σ_p) with temperature in CuZn single crystals[27].

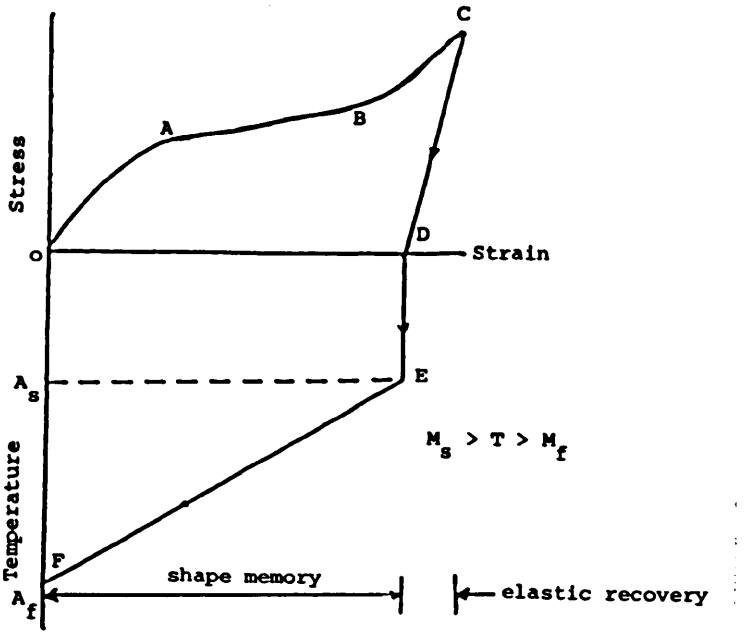

Figure 2.5 Schematic stress-strain curve for a shape memory specimen deformed at a temperature below M_s.

CHAPTER 3

TiNi SHAPE MEMORY ALLOYS

3.1 Introduction

The titanium-nickel compound of approximately equiatomic concentration, TiNi, is one of the most attractive shape memory alloys from the point of view of industrial application, but it is relatively expensive to process by conventional methods. One of the earliest uses of TiNi was for aircraft hydraulic tube couplings manufactured by Raychem Corporation of the United States[11]. The hydraulic fitting in the form of sleeve is machined to have an inner bore of about 4% less than the outer diameter of the tubes to be joined. The coupling is expanded in the martensitic state at liquid nitrogen temperature to a diameter greater than that of the tubes and then placed over the ends of the tubes. On allowing the assembly to heat to room temperature (i.e. above the transformation temperature of the particular alloy), the coupling contracts producing a tight seal joint. By using this technique, metallurgical problems associated with welding and brazing are avoided. Such TiNi couplings have been extensively used by the aircraft industry and similar fittings are also widely employed by the US and the British navies[11].

In addition to the shape memory behaviour, TiNi possesses a unique combination of physical and mechanical properties. These were first observed by Buehler and co-workers[35,36]. Unlike many other

intermetallics which are brittle at room temperature they found TiNi to be ductile (up to 16% elongation). It also displays good corrosion properties in a testing environment of impinging sea water at velocities ranging from 5 to 8 ms^{-1} over 60 days. It was also found to have a fatigue life greater than 10^7 cycles at a stress level of 480 MPa. It sustains a high temperature hardness of about 250 HV at 400°C[35]. TiNi alloys can also be quench-hardened to achieve a hardness value up to 700 HV[35,36].

The alloy has been extensively studied since the first report by Buehler et al[1] concerning its shape memory performance, although most reported investigations have been confined to developing an understanding of the underlying structural transformation involved. The high temperature phase has an ordered bcc caesium chloride structure which on cooling undergoes a thermoelastic martensitic transition. The information available regarding the crystal structure of the martensite, and the Ti-Ni phase diagram remains controversial. In the following sections, a review of the main experimental results on these aspects is presented.

3.2 The Phase Diagram

Despite the considerable number of investigations on the titanium-nickel binary phase diagram, the exact nature of the equiatomic region has not been established. Four proposed versions of the phase diagram are shown in Figure 3.1. According to Duwez and Taylor[37], on cooling, the high temperature TiNi compound decomposes

above 800°C into a mixture of Ti_2Ni and $TiNi_3$ (Figure 3.1a). This view was confirmed by Poole and Hume-Rothery[38], whereas, Margolin et al[39] could not obtain any evidence of such decomposition. Instead, they proposed a diagram with the compound TiNi existing over a composition range from 49 to 54 at -% Ni at temperatures below 1000°C (Figure 3.1b). Purdy and Parr[40] suggested that a restricted homogeneity range of TiNi exists at low temperatures (Figure 3.1c). This proposition was supported by Wasilewski et al[41] who in addition reported that a new phase related to $TiNi_3$ but of the approximate composition Ti_2Ni_3 forms peritectoidally at about 625°C (Figure 3.1d). There is also a marked difference between the liquidus temperature of 1310°C at the equiatomic composition proposed by Duwez and Taylor, and Poole and Hume-Rothery (adopted by Wasilewski et al) and the one (1240°C) proposed by Margolin et al and chosen by Purdy and Parr.

The reason for the disagreement between these results may be attributed to factors such as;

(i) experimental error resulting from the methods employed by different workers,

(ii) impurity content of the alloy.

In the Margolin (Figure 3.1b) experiment, the melting point of the alloy was taken to be the temperature at which the specimen assumed the shape of the containing graphite crucible. Since this could well happen while some solid phase is still present, such a

method of determining melting temperature is likely to be less accurate than the thermal analysis technique used by Poole and Hume-Rothery. This accounts for the lower liquidus temperature reported by Margolin. The melting point of TiNi can also be affected by the impurity content. Wasilewski et al[41] have provided experiment evidence which shows that a small rise in the level of oxygen contamination can cause a decrease in the melting temperature of TiNi alloy. However, since Margolin et al used materials of high purity, the effect of interstitial content on their results may not be significant.

In the present investigation, microhardness measurements were made on sintered compacts with varying composition from 49 to 56 at -% Ni which were either water quenched or furnace cooled from 1000°C. The hardness of the equiatomic composition was found to be unaffected by cooling rate, whereas quenched samples containing 52 at -% Ni and over showed considerably higher values than those cooled in the furnace. In addition, furnace cooled specimens with 52% Ni and above had second phase nickel-rich precipitates in their structure while the equiatomic composition was a single phase. From these observations, it can be argued that the homogeneity range of TiNi at room temperature is narrower than that proposed by Margolin et al (49 to 54 at -% Ni). The phase diagram due to Wasilewski et al is thus, found to be more consistent with the present results.

3.3 Phase transition, Crystal Structures and Transformation Phenomena

Although different results have been reported concerning the titanium-nickel equilibrium diagram, it is generally agreed that the high temperature phase of the equiatomic compound can undergo a martensitic transformation near room temperature. The existence of such a diffusionless transition in this alloy was first reported by Purdy and Parr[40] in 1961, and the powder pattern of the transformation product was indexed as hexagonal. Since then, the crystal structures of both the matrix and martensite phases have been investigated by many researchers (e.g. Refs. 42-45). The structure of the parent phase has been established to be the ordered bcc caesium chloride (B2) type with a unit cell of a = 3.015 Å[42], but in spite of numerous studies, controversy remains regarding the structure of the martensite. Dautovich and Purdy[43] in 1965, studied the martensitic phase. On analysing the electron diffraction patterns and X-ray powder photographs they proposed that TiNi also experienced a separate premartensitic transition. The crystal structure of the intermediate phase was reported to be rhombohedral with a = 6.02 Å and α = 90.7° while that of the martensite was triclinic with lattice parameters a = 4.60 Å, b = 2.86 Å, c = 4.11 Å, α = 90.1°, β = 90.9° and γ = 96.7°.

A similar study was undertaken by Marcinkowski et al[44] three years later and from the results of electron diffraction, they reported the co-existence of two types of monoclinic structures which

were designated M and M'. In 1971, Hehemann and Sandrock[45] and Otsuka et al[42] obtained essentially the same lattice parameters by X-ray and electron diffraction techniques and reported the structure to be a monoclinic distortion of the B19 type. This view has been supported by most recent workers (e.g. Refs. 46, 47) using various techniques (electron, X-ray and powder neutron diffraction). A summary of the proposed structures and their lattice parameters is given in Table 3.1.

A detailed study of the transition from B2 to the martensitic phase was undertaken in 1980 by Ling and Kaplow[48] using electrical resistance measurement and X-ray diffraction. They came to the conclusion that the onset of the martensitic reaction is not necessarily preceeded by the rhombohedral transformation (R phase) and that the latter proceeds continuously below a critical temperature, T_R and persists during the whole range of the martensitic transformation. They then proposed three possible phase transitions in TiNi alloy:

$$B2 \rightleftharpoons M, \quad R \rightleftharpoons M \quad \text{and} \quad B2 \rightleftharpoons R.$$

According to Ling and Kaplow, the intermediate transition can be pre-empted by the martensitic reaction if M_s is significantly higher than T_R. They suggested that factors, such as thermal cycling of the specimen through the transformation range or variation of alloy composition, which decrease M_s relative to T_R might be required to see both transitions.

In the present study, the M_s of equiatomic TiNi alloy was found to be depressed by rapid solidification (RS) processing and the differential scanning calorimetry cooling curves showed two-step transformation peaks. By comparison with the RS material, samples prepared by a powder metallurgy technique had a relatively higher M_s with only one transformation peak, which is in agreement with the proposition by Ling and Kaplow. Full discussion of these results will be given in chapter 9. However, it seems that the closeness and overlap of the intermediate and martensitic reactions, and the role of processing conditions on the transformation behaviour of TiNi alloy have been the source of difficulty in determining the structure of the martensite.

TiNi displays a number of anomalous effects such as;

(i) the appearance of extra diffraction spots at one-third positions of the B2 reciprocal lattice, the intensities of which increase with a fall in temperature[49];

(ii) splitting in the {110} and {211} X-ray reflections[50,51];

(iii) a two-step exothermic peak in differential thermal analysis plots during cooling[52-54];

(iv) the rapid increase in electrical resistivity on cooling from the high temperature B2 phase[55,56].

Table 3.1 Comparisons of crystallographic data for TiNi martensite

	DP[43]	MSK[44]		HS[45]	OSS[42]	MS[46]
Structures	triclinic	monoclinic		monoclinic	monoclinic	monoclinic
		M	M'			
a (Å)	4.60	5.19	5.19	2.883	2.889	2.885
b (Å)	2.86	4.96	5.52	4.117	4.120	4.120
c (Å)	4.11	4.25	4.25	4.623	4.622	4.622
α (°)	90.1					
β (°)	90.9	99	116	96.8	96.8	96.8
γ (°)	96.7					

DP[43], Dautovich and Purdy (1965)

MSK[44], Marcinkowski et al (1968)

HS[45], Hehemann and Sandrock (1971)

OSS[42], Otsuka et al (1971)

MS[46], Michal and Sinclair (1981)

These effects have become known as premartensitic phenomena. They were previously thought to be precursory effects associated with the martensitic reaction until Dautovich and Purdy[43] reported the existence of the intermediate reaction. Chandra and Purdy[49] in 1968 considered the extra reflections as being streaks originating from instabilities in the crystal due to the presence of an intermediate phase. They re-indexed the powder pattern obtained by Dautovich and Purdy in terms of rhombohedral cell with a = 9.03 Å and α = 89.3.

The peak splittings have also been interpreted in terms of a rhombohedral distortion of the B2 unit cell[50,51] and the two-step exothermic peaks have similarly been explained on the basis of a two-step transition sequence[52-54]. The electrical resistivity phenomenon has been under discussion. Wang and co-workers[55] and Sandrock et al[56] attributed it to incomplete thermal cycling effects (i.e. cooling the specimen to form martensite and heating until a proportion of the martensite transforms to the high temperature phase). It has now been shown that electrical resistivity peak also results from complete cycling[57]. This involves cooling to transform the entire specimen to martensite and then heating until a complete reversion to the high temperature phase is achieved. However, by observing surface relief at various stages during heating and cooling, Sandrock et al[56] correlated the resistivity peak with the martensitic transformation temperature, M_s.

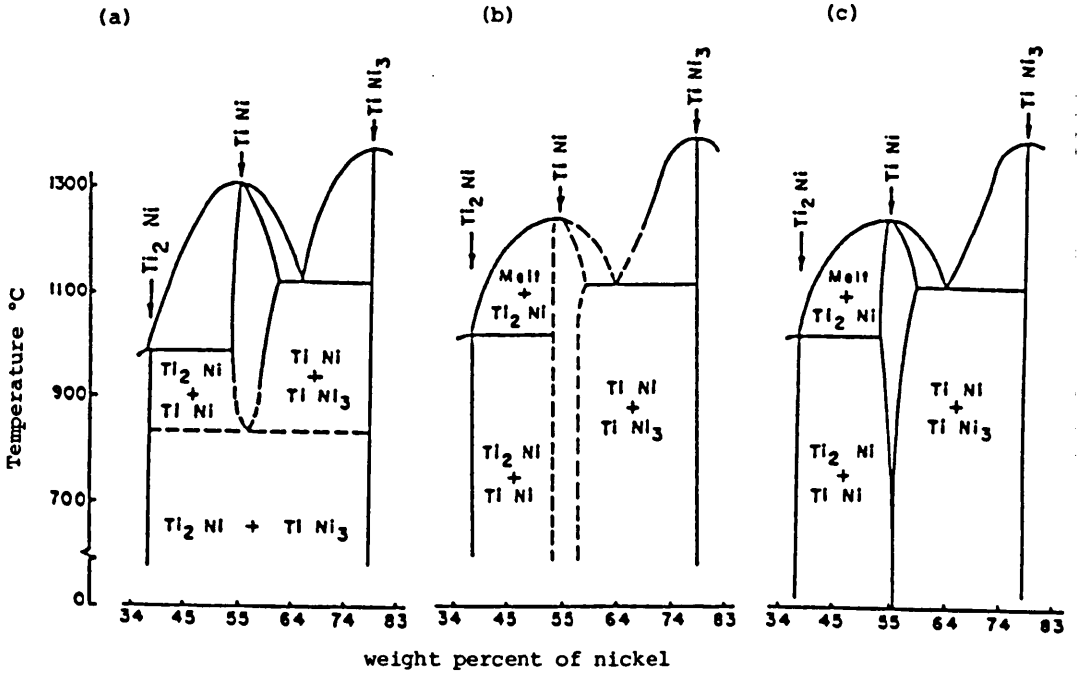

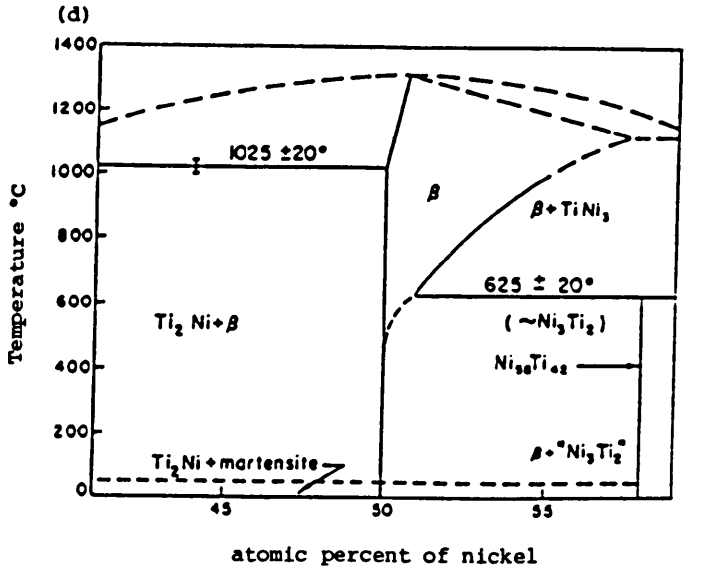

Figure 3.1 Equiatomic region of Ti-Ni equilibrium diagram

(a) Duwez and Taylor, 1950[37]

(b) Margolin et al, 1953[39]

(c) Purdy and Parr, 1961[40]

(d) Wasilewski et al, 1971[41]

CHAPTER 4

POWDER METALLURGY PROCESSING

4.1 Introduction

Powder metallurgy (P/M) is the technology of producing metal powders and utilising them to make serviceable objects[58]. The essential features of this process are the production of powder and its consolidation into a solid form.

The first instance recorded for P/M technology was in Egypt (around 3000 BC)[59,60]. Iron implements, for example, were prepared in this manner because it was not possible, with the primitive furnaces then available, to obtain temperatures high enough for fusion. As suitable furnaces were developed, the manufacture of articles from iron granules was superseded by ingot methods, except where the melting point of the material was too high (e.g. Platinum and Tungsten)[61,62].

However, the first significant use of P/M related to general manufacturing started in Germany in the 1920s with the production of tungsten carbide cutting-tool tips. A steady expansion period of the P/M industry developed through the 1930s until 1960, which led to the manufacture of a wide variety of P/M products including porous bronze bearings and many composites (e.g. a combination of high melting point inorganic non-metallic materials and metals)[59,60]. Since then the

growth of P/M has increased rapidly. There are now a number of consolidation techniques such as hot isostatic pressing and hot extrusion which allow the processing of full density products of comparable properties with those of wrought material. Thus, today, powder metallurgy has advanced from an art to a highly sophisticated technology and represents one of the three basic fabrication processes for the production of engineering components. A summary of the major historical developments in powder metallurgy is presented in Table 4.1[60]. Industrial applications of P/M include[63]:

(i) Processing of materials which cannot be or are not readily produced by conventional melting techniques such as refractory metals, porous products, cemented carbides, combination of metals which are insoluble in each other in the liquid state, and products in which the combined properties of metals and non-metals are desired.

(ii) Products which can be manufactured more economically by P/M than by ingot metallurgy methods, e.g. structural parts made to close dimensional tolerances, and components from high cost alloys which can be made to net or near-net shape.

Much has been written on the mechanisms involved in the science of powder metallurgy. In the following sections, a review of the scientific aspects of powder consolidation is presented. In many instances, powders are pressed to a green compact and sintered at a temperature where diffusion allows atomic bonding to occur between the

Table 4.1. Major historical developments in powder metallurgy

Date	Development	Origin
3000 B.C.	"Sponge iron" for making tools	Egypt, Africa, India
1200 A.D.	Cementing platinum grains	South America (Incas)
1781	Fusible platinum-arsenic alloy	France, Germany
1790	Production of platinum-arsenic chemical vessels commercially	France
1822	Platinum powder formed into solid ingot	France
1826	High-temperature sintering of platinum powder compacts on a commercial basis	Russia
1829	Wollaston method of producing compact platinum from platinum sponge (basis of modern P/M technique)	England
1830	Sintering compacts of various metals	Europe
1859	Platinum fusion process	
1870	Patent for bearing materials made from metal powders (forerunner of self-lubricating bearings)	United States
1878-1900	Incandescent lamp filaments	United States
1915-1930	Cemented carbides	Germany
Early 1900's	Composite metals	United States
	Porous metals and metallic filters	United States
1920's	Self-lubricating bearings (used commercially)	United States
1940's	Iron powder technology	Central Europe
1950's and 1960's	P/M wrought and dispersion-strengthened products, including P/M forgings	United States
1970's	Hot isostatic pressing, P/M tool steels, and superplastic superalloys	United States
1980's	Rapid solidification and injection moulding technology	United States

particles. There are a number of other processing methods (e.g. extrusion, hot isostatic pressing, rolling, etc.) but for the present investigation most attention will be paid to the press and sinter routes. Subsequently I will consider the specific case for components made from titanium powder.

4.2 Powder Pressing

Prior to the pressing operation, the desired particle size distribution of the different elemental powders (e.g. mostly between 40 and 150 μm for commercial titanium powder) are blended and mixed to produce a homogeneous mixture. Cold compaction is performed either in an enclosed die between opposing punches or in an isostatic press, Figure 4.1[64]. The pressures commonly employed range from 70 to 700MPa depending on the hardness of powder particles and the required density. In general, the density of the green (unsintered) compact increases with compaction pressure. A typical pressure/density curve is shown in Figure 4.2[61].

The theoretical analysis of the compaction process has been reported by many researchers[65-67]. Most of the investigations have been concerned with the effect of pressure on the compact density. One of the most quoted relationship between pressure and density is the proposal given by Shapiro and Kolthoff[65] and Heckel[66] using die pressing:

$$\ln (1/1-D) = KP + A \qquad 4.1$$

in which D - the relative density (i.e. the ratio of the actual density to the theoretical density of the solid metal)

P - applied pressure

K and A - constants

This equation gives a relationship with three characteristic regions, figure 4.3[70], which are widely held to correspond to compaction mechanisms. Investigations by Morgan and Sands[68] show that a similar relationship is applicable to cold isostatic pressing (CIP) except that the slope of line X - Y is steeper than that for die compaction. This indicates that a higher green density is achieved with CIP for a given compaction pressure.

Different interpretations of the three regions (Figure 4.3) have been reported. Marshall[69] attributed the first region to densification during filling of the die, the second to densification by particle movement and rearrangement at low pressures prior to interparticle bonding and the third to densification by particle deformation after interparticle bonding. Hewitt et al[70] proposed that plastic deformation occurs throughout the powder compaction operation and that the transition from first to second occurs when the applied pressure exceed the bulk yield strength of the material. However, it is generally agreed[69,70] that the mechanism for the development of green strength in pressed compacts is the result of particle rearrangement and deformation leading to mechanical interlocking and cold welding of particles.

Apart from compaction pressure the compact green density is to a considerable extent also dependent on the powder particle characteristics (e.g. particle size, shape, structure and surface area). For example, fine particles with larger surface area and consequently higher interparticle friction tend to achieve lower green densities than coarse particles. However, the high specific surface associated with fine particles is desirable for sintering since the driving force for particle bonding during the sintering process is the excess energy associated with the surface area[61], as will be discussed in the next section.

4.3 Sintering

It has not been possible to formulate a universally accepted definition which covers all the various phenomena that take place during sintering. The difficulty is attributable to the fact that there are many sintering processes (e.g. solid state sintering and liquid state sintering) operating by several mechanisms. For example, sintering has been defined[71] as "a process of reducing the interior and exterior surface of a body or of bodies of particles in contact by reinforcement of contact bridges and the reduction of the void volume. During this process at least one of the main components should be in the solid state". This definition is widely accepted, yet it clearly does not take into account the increase in pore volume observed during the sintering of some alloy systems such as Fe-Cu[72,73]. Thus, although the prime aim of sintering is the elimination of pores and strengthening of the green compact, sintering can also occur without densification.

Sintering, however, can be considered to occur in three stages which correspond to different geometrical morphologies of the pore-solid particle array[63,64,74]:

(i) The first stage is the growth of necks at points of contact between individual particles. This is associated with a decrease in the distance between particle centres and a reduction in pore volume[63]. The neck growth and shrinkage are such that the individual particles are still discernible (Figure 4.4a)[75].

(ii) In the intermediate stage, neck growth continues and the interconnected net-work of pores nip-off and close. Individual particles begin to loose their identity (Figure 4.4b) and densification proceeds. Most of the shrinkage is believed to occur at this stage[64]. Grain boundary migration across the original interparticle contact starts leading to grain growth[74].

(iii) The final stage is identified by isolation and spheroidization of pores (Figure 4.4c) and a further but slow shrinkage. The density of the compact starts to approach the theoretical value of the solid material[61,64].

In the following sub-sections, three sintering processes (single phase, multi-phase, and liquid-phase) are considered on the basis of these changes in particle shape.

4.3.1 Single Phase Sintering

The change of particle shape decreases the total surface area contained in the system and consequently its overall surface energy. The driving force for sintering in a single phase system is the reduction in surface free energy which is often called surface tension. Several mechanisms of atomic rearrangement by which a decrease in surface energy occurs have been proposed. These include viscous flow, evaporation-condensation, plastic flow, and diffusional flow.

The viscous flow mechanism was put forward by Frenkel[76] in 1945, as occuring in both amorphous and crystalline materials. In crystalline particles, he attributed this viscous flow to the diffusion of vacancies in the lattice. He then derived the following equation which relates the interparticle neck growth between two spheres (Figure 4.5) with time, t.

$$x^2 = \frac{3}{2}\frac{a\,\gamma t}{\eta} \qquad 4.2$$

in which x - interparticle radius

a - original radius of the sphere

γ - surface tension

η - viscosity coefficient

Nabarro[77] has shown that vacancies cannot give rise to a viscosity type of flow in a single crystal lattice. However, Kuczynski[78] has found it to be the mechanism of sintering glasses.

At the interface between two bodies in contact, the stress, σ generated by the surface tension forces is related to the two principal radii of curvature of the surface r_1 and r_2 and the surface tension, γ according to the Laplace's equation

$$\sigma = \gamma \left(\frac{1}{r_1} + \frac{1}{r_2}\right) \qquad 4.3$$

For a single phase system of two spheres or a sphere and a flat plate (Figure 4.6) in which the neck region is characterised by two radii of curvature ρ and α, Kuczynski[79] has considered the stresses in the neck area due to surface tension forces. He proposed that the stresses present cause a gradient in vapour pressure between the neck cavity (concave) and the neighbouring surface (convex) resulting in evaporation of material from the latter to the former. The rate of material transport, G is given by:

$$G = K (p_1 - p_2) \qquad 4.4$$

where p_1 and p_2 are the respective equilibrium pressures above the convex and concave surfaces, and constant K a function of temperature. This mechanism has been found to be significant only when sintering materials with high vapour pressure such as NaCl[80,81].

The principal mechanism in the sintering of metals is that of diffusional flow due to a concentration differential in lattice vacancies. The rate of material transfer by this process under a concentration gradient is usually expressed by Fick's first law:

$$J = -D \frac{dc}{dx} \qquad 4.5$$

where J - mass of substance flowing in unit time through unit area in the direction of the concentration gradient of - $\frac{dc}{dx}$ (the minus sign indicates that the concentration decreases along a distance, dx).

$\frac{dc}{dx}$ - concentration gradient

D - diffusion coefficient which is related to temperature by the Arrhenius type of equation:

$$D = D_o e^{-Q/RT} \qquad 4.6$$

Here D_o - frequency factor

Q - activation energy for the process

R - universal gas constant

T - absolute temperature.

According to Kuczynski, the stresses in the neck area result in vacancy concentrations which allow atomic movement from the convex surface to the concave neck. By considering one mechanism at a time as the only mode of material transfer by diffusion, under the influence of the gradient in vacancy concentration, he developed an equation for the rate of neck growth by volume self diffusion:

$$\frac{x^5}{a^2} = \frac{40\gamma\delta^3}{KT} D_v t \qquad 4.7$$

where x and a are the respective radii of the interface neck and the sphere

γ - surface tension

δ - interatomic distance

D_v - coefficient of volume self diffusion

t - time

K - Boltzmanns constant.

and for surface diffusion:

$$\frac{x^7}{a^3} = \frac{56\gamma\delta^4}{KT} D_s \, t \qquad 4.8$$

in which D_s is the coefficient of surface diffusion.

Kuczynski verified experimentally the rate of neck growth using 100 μm copper spheres and found it to be proportional to the fifth root of sintering time, which was in agreement with the value obtained for the case of volume diffusion. He then concluded that volume diffusion was the dominant mechanism during sintering. Kuczynski's work was the first important contribution to the historical development in the understanding of the fundamental sintering mechanisms. However, he did not consider the possible role of grain boundaries in atomic movement. The theory that grain boundaries can act as diffusion paths was developed by Herring[82] in 1950. He postulated that when polycrystalline material is subjected to an applied stress, vacancies move from grain boundaries under tension to those under compression (Figure 4.7) representing atomic flow in the reverse direction. Thus, in powder compacts, atoms are transported from the grain boundary formed at the interparticle

contact (compressive) to the neck surface (tensile). The first experimental observation of the significant role of grain boundaries in sintering was reported by Alexander and Balluffi in 1957[83]. They found that the pores in their copper powder compacts decreased in size only when they were intercepted by a grain boundary.

Hence, diffusional flow of atoms can occur by volume, surface and grain boundary diffusion. The actual contribution of each process in sintering depends on various factors such as the relative magnitudes of the individual diffusion coefficients, D_v (volume), D_s (surface) and D_{gb} (grain boundary), grain size, and sintering temperature. Ashby[84] has proposed the concept of sintering diagrams in which lines are drawn as a function of neck size, sintering time and temperature. Such a diagram for the sintering of two copper spheres is shown in Figure 4.8. The fully drawn boundaries correspond to the sintering conditions under which each of the two adjacent mechanisms shown contribute half of the total material transported to the neck region.

The final material transport mechanisms to be considered in this section is that of plastic flow. It is based on the hypothesis that plastic flow (i.e. dislocation motion) caused by capillary forces contributes to the shape change experienced by powder particles during sintering. The result of a model experiment[85] using single crystal copper spheres showed that the dislocation density in the neck region increased during sintering. In an investigation conducted to verify this material transfer mechanism, Brett and Siegle[86] sintered three

twisted nickel wires with fine alumina particles applied to serve as inert markers. They found that the material which filled the neck cavities was completely free of markers, and therefore concluded that plastic flow was not the dominant sintering mechanism. However, Hirth[87] has calculated the rate of dislocation generation at a free surface due to surface tension and found that only when the radii of curvature of the surfaces are small (e.g. 40 nm) that the stress is sufficient to create enough dislocations to cause plastic flow.

In summary, sintering which is defined by neck formation between neighbouring particles occurs by several material transfer mechanisms. These include viscous flow, evaporation-condensation, diffusional flow and plastic flow. In single phase metallic systems, the dominant process is self diffusion of atoms. However, it must be emphasised that the bulk of powder sintering mechanisms have been studied mainly on idealised model samples (e.g. two spheres). Sintering phenomena in real systems are more complex because of the various effects of several variables (e.g. particle size, purity, sintering atmosphere, rate of heating) associated with actual sintering. For example the presence of surface oxide film adversely affect the sintering of aluminium powder[88].

4.3.2 Sintering in Multi-phase Systems

In section 4.3.1, the various mechanisms for atomic transfer in single-phase sintering have been considered and it is demonstrated

that the dominant mechanism is that of self diffusion. In the case of two or more elemental powders, however, the process of sintering is not limited to self diffusion, heterogeneous diffusion can also occur. The main driving force for heterogeneous diffusion is the concentration gradient across the interface which results in material exchange between particles and may therefore cause bonding but not necessarily shrinkage. Compact growth may occur due to the formation of diffusional porosities as a result of the difference in the diffusivity of individual elements. This phenomenon was first reported by Smigelskas and Kirkendall[89] in 1947.

Thus, a compact prepared from more than one metal powder possesses not only the excess free energy due to the overall surface area, but also an excess energy leading to alloy formation. The dominant mechanism for such systems can be determined by comparing the magnitude of these two driving forces. By assuming a model compact consisting of spherical particles and considering the decrease in surface area of the particles due to the pressing operation to be negligible, Savitskii[90] derived the following equation for the evaluation of the surface energy, G_s, for a binary system:

$$G_s = 3 \left[\frac{M_a \gamma_a}{\rho_a r_a} = \frac{M_b \gamma_b}{\rho_b r_b} \right] \qquad 4.9$$

in which M_a and M_b - mass of the pure powders in moles

γ_a and γ_b - specific surface free energies

ρ_a and ρ_b - density of the pure metals

r_a and r_b - the particle radii

During alloy formation in a binary system, the free energy of mixing, G_{mix} can be calculated using the Gibb's free energy equation:

$$\Delta G_{mix} = \Delta H - T\Delta S \qquad 4.10$$

where ΔH and ΔS are the respective changes in enthalpy and entropy of the system due to mixing at temperature, T(°K).

Savitskii used these equations to determine the energies involved in the sintering of equiatomic TiAl and found the alloy formation energy (46.5 $kJmol^{-1}$) to be considerably larger than the overall surface energy (0.017 $kJmol^{-1}$) contained in the compact. The result suggests that the driving force for sintering elemental powders would be much higher than that for TiAl prealloyed powder. In the latter case, the individual powder particles have the same composition as that of the desired final product, hence the alloy formation energy is non-existent. Consequently the prealloyed powder would be expected to require a higher sintering temperature. This view was not verified experimentally by Savitskii, since he was only interested in the relative contribution of these two sintering processes to compact volume changes. However, in an investigation in to the sintering of Ti-6Al-4V, Abkowitz[91] found that whereas the compact made from elemental powders was satisfactorily sintered at 1230°C, a temperature well above 1260°C was required for prealloyed powder. Similar observations had been made in the present research (Chapter 9).

4.3.3 Liquid Phase Sintering

During the sintering of some multi-component systems, the temperature may be high enough for one or more of the materials to melt and liquid phase sintering (LPS) will result. In certain alloy systems (e.g. WC-Co) the liquid phase remains throughout the entire sintering process, whereas in others (e.g. Fe - Cu) it disappears by interdiffusion as sintering progresses. The latter is often called a transient liquid phase sintering. LPS has been used for many years in the fields of cemented carbide and heavy alloys (notably tungsten with up to 10% of nickel and copper) for producing high density material.

Analysis of the fundamental aspects of densification in liquid phase sintering is often divided into the three stages which were first proposed by Kingery in 1959[92]:

(i) First stage of particle rearrangement;
(ii) Intermediate stage of dissolution and reprecipitation;
(iii) Final stage of particle coalescence.

These will now be considered in turn.

First Stage - Particle Rearrangement

Particle rearrangement during liquid phase sintering is based on the concept that melt bridges exist between most of the adjacent solid phase in the compact. The collapse of these bridges under the action

of capillary forces leads to a co-operative movement of liquid and particles in such a way that overall densification occurs. According to Kingery, the capillary forces cause a negative pressure in the pores which is equivalent to subjecting the whole system to hydrostatic pressure. The pressure, P is given by[61]:

$$P = \frac{2\gamma_{LV}}{r} \qquad 4.11$$

where γ_{LV} - liquid-vapour surface energy

r - the pore radius.

The extent of densification by this process largely depends on factors such as (i) the degree of particle wetting by the molten phase (ii) particle geometry and (iii) the amount of liquid present. The liquid phase will wet and run over the surface of the dispersed particles if the surface energy of the solid/vapour (γ_{SV}) is greater than the sum of liquid/vapour (γ_{LV}) and the liquid/solid (γ_{LS}) interface surface energies[61,93] i.e.;

$$\gamma_{SV} > \gamma_{LS} + \gamma_{LV} \qquad 4.12$$

Under the conditions of complete wetting (i.e. when the solid particles are well isolated in the liquid), spherical particles, and the presence of sufficient molten phase ($\geq$ 35% volume fraction), full densification is possible[61]. Huppmann and Riegger[94] have studied the phenomenon of particle rearrangement using copper-coated tungsten. As tungsten is insoluble in liquid copper[95], other processes of

densification (e.g. dissolution and reprecipitation) were avoided. They found that the time of densification, following the formation of liquid phase is very short and takes only seconds.

Intermediate Stage - Dissolution and Reprecipitation

This involves the dissolution of solid particles into the liquid at solid/liquid interfaces of high chemical potential and reprecipitation on to areas of lower chemical potential. This process was first recognised by Price et al[96] in 1938, who attributed it to the higher solubility of small particles compared with larger particles. Kingery[92] has demonstrated that this view is inadequate on the ground that the difference in solubility of flat surfaces compared with that of a small particle is insufficient to account for the material transport observed. He then suggested that the stresses due to surface tension forces arising from the presence of pores in the compact area concentrated in the regions where the solid particles are separated by thin molten films. According to Kingery, this stress concentration causes a chemical potential gradient between highly stressed areas and the remainder of the particle surface, resulting in the dissolution of the solid phase at the region of stress concentration followed by reprecipitation in areas of lower stress. This transfer of material through the melt leads to further densification. The process can only occur if there is at least a limited solubility of the solid material in the molten phase.

Final Stage - Particle Coalescence

Under certain conditions in liquid phase sintering (for example, when the particles are not completely wetted by the liquid or when there is insufficient molten material), stable interparticle contacts may be formed. Coalescence of particles then occur by neck growth and migration of grain boundaries through interparticle necks leading to grain growth. The material transport modes in this case will be similar to those for solid state sintering. Experimental evidence confirming this process has been presented by Yoon and Huppman[97] in the tungsten-nickel system (Figure 4.9).

4.3.4 Summary

It was pointed out in section 4.3.1 that the most important material transfer mechanism during the sintering of a single phase powder compact is self diffusion. However, in the case of a compact prepared from a mixture of metal powders, both self diffusion and interdiffusion between different elements occur simultaneously. The driving force for interdiffusion is the chemical potential gradient caused by concentration differences. As a result of the unequal interdiffusion rates of different elements, excess vacancies accumulate and may result in an increase in the volume fraction of pores.

In some alloy systems, the sintering temperature may be sufficiently high for a liquid phase to form. Densification during

sintering in the presence of a liquid phase occurs by the mechanisms of particle rearrangement under the influence of capillary forces, dissolution of solid material in the molten phase and reprecipitation on other particles and particle coalescence. The extent of densification is dependent on factors such as particle geometry, volume fraction of liquid present, and the degree of solid particle wetting by the liquid phase. The conditions for full densification are those which allow maximum mobility of solid phase. In certain systems for example, tungsten-copper alloys where the liquid phase appears in a straight forward manner as the compact is heated to the melting point of copper, particle mobility is possible and full densification can be achieved, in the presence of a large volume of molten material. In other cases, however, for instance when there is insufficient liquid, the formation of stable interparticle contacts can prevent mobility and hence inhibits densification.

4.4 Powder Metallurgy of Titanium Alloys

The economic attractions of producing parts by powder metallurgy has long been appreciated in many component manufacturing industries. Early exploitation of titanium and titanium alloy powder metallurgy (P/M) has been hindered by the problem of interstitial pick-up encountered during the production of titanium powder. More recently, however, better powders have become available, which has led to an increasing interest in titanium alloy components produced by P/M[98,100]. Most of this work has concentrated on aerospace applications and very little has been reported concerning the P/M processing of titanium alloys for other requirements.

There are currently two developed routes for producing near-net shape of titanium alloy P/M parts:

(i) hot isostatic pressing (HIP) of prealloyed powders;

(ii) cold compaction and sintering of blended elemental powders, sometimes followed by HIPing.

Since most applications of titanium alloy components is still in aerospace industry, it is necessary that P/M parts are consolidated to 100% density. Much attention over the years has been focussed on the hot isostatic pressing of prealloyed powders. There are presently two methods for producing prealloyed powder commercially:

(i) processing from liquid metal and
(ii) comminution of solid stock material.

Powder may be produced from the melt either by local melting and powder formation or by atomisation of a large mass. Since molten titanium readily reacts with refractory linings, powder production from a large mass of liquid has not been possible. The usual technique of producing titanium alloy powder from the melt is, therefore, the local melting approach. The most common variant which has reached large scale production is the rotating electrode process (REP or PREP)[101]. In this process, a bar of the alloy to be produced in powder form is rotated at a high speed about its longitudinal axis (Figure 4.10). One end of the rod is heated by an

electric arc or plasma. When the centrifugal force due to bar rotation exceeds the liquid surface tension, molten material is thrown off as droplets. The operation is undertaken in an atmosphere of helium. A typical morphology of prealloyed powder particles is shown in Figure 4.11a. Prealloyed powder can also be produced by rapid solidification (RS) techniques, such as the chill block melt spinning method[102]. In this process, a molten jet of metal is ejected through an orifice onto a rotating wheel, producing rapidly solidified material in the form of ribbon which can be ground to powder. This method was employed in the present research. Full details will be presented in the next chapter. Other RS methods, such as the pendant drop melt extraction[102] can also be used but these will not be considered in the present work.

The final technique to be considered for producing commercial titanium alloy powder is the hydriding-dehydriding process[103]. It takes advantage of the affinity of titanium for compound forming elements (e.g. oxygen, hydrogen). This process uses feed stock titanium alloy in the form of chips or turnings. The starting material is reacted with high purity hydrogen at about 450°C according to:

$$Ti + 2H \rightleftharpoons TiH_2 \qquad 4.13$$

The resulting brittle hydride is comminuted in an attrition mill. The milled powder is then dehydrided at a temperature between 700 to 750°C in vacuum. The loosely sintered powder is again

attrited, followed by screening and magnetic separation. The whole operation is performed under an argon atmosphere to prevent contamination. The morphology of typical prealloyed powder particles produced by this method is shown in Figure 4.11b.

The consolidation of prealloyed powders is often performed using hot isostatic pressing (HIP). A technique developed for processing titanium alloy powders is the fluid die method[98] (Figure 4.12). In this process, a thick-walled container having an interior cavity with the enlarged configuration of the component to be pressed is machined or cast. The cavity is filled with the prealloyed powder. On pressing, the die becomes fluid under the influence of heat and pressure, thus consolidating the powder to full density. Mechanical properties of hot isostatically pressed materials are similar to those of wrought products[104]. However, the relative high cost of prealloyed powder has been a problem. Hence in the past few years increasing attention is being given to the development of the blended elemental technology which offers an inexpensive near-net shape process.

The elemental approach uses mixtures of titanium sponge fines and alloying element powders. The commercial production of titanium powder involves reacting titanium tetrachloride with magnesium according to the reaction[103,105]:

$$TiCl_{4(g)} + 2Mg_{(1)} = Ti_{(s)} + 2MgCl_{2(g)} \qquad 4.14$$

at a temperature betweeen 900 and 1050°C. The reaction product is then subjected to vacuum sublimation to obtain sponge. Cold compaction is undertaken using either an isostatic press or a die press. Since titanium powder is quite soft and ductile, green densities approaching 90% of theoretical value are readily achieved. Sintering is performed in a vacuum furnace. For certain applications, the densities (about 96%) and hence the mechanical properties of pressed and sintered materials are adequate, but for critical-components (e.g. rotating engine parts) the residual volume fraction of pores acts as stress concentrators resulting in poor dynamic properties. The effects of pores on the properties of Ti-6Al-4V, have been studied by Mahaja et al[106]. They found that while the pores may have a beneficial effect by controlling grain size, fatigue properties were degraded. The fatigue performance for prealloyed and elemental powder is compared to that of wrought material in Figure 4.13. Hot isostatic pressing has been successfully employed to raise the density and therefore, the mechanical properties of cold isostatically pressed and sintered Ti-6Al-4V[107]. The combined process is often referred to as CHIP. The mechanical properties achieved following the HIP operation are shown in Table 4.2 and compare favourably with samples processed by ingot metallurgy techniques.

Perhaps the most attractive feature of blended elemental powders is its relative cheapness. Cost savings of up to 70% have been reported[108,109]. This results from the use of relatively inexpensive titanium sponge, improved material yield, and the production of near-net shapes with reduced machining.

Table 4.2 Mechanical Properties of Pressed and Sintered, and Sintered Plus HIP TI-6Al-4V[107]

Treatment	% Theoretical Density	U T S MPa	Y S MPa	% El	% RA
Press and Sintered (P&S)	94	109.4	93	3	3
P&S + HIP	99+	127	117	9	17
Wrought	100	130	120	10	25

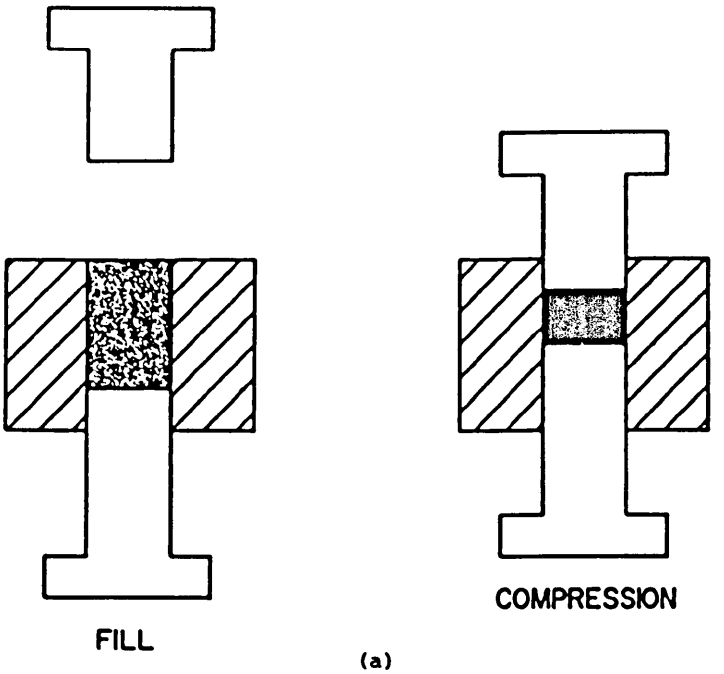

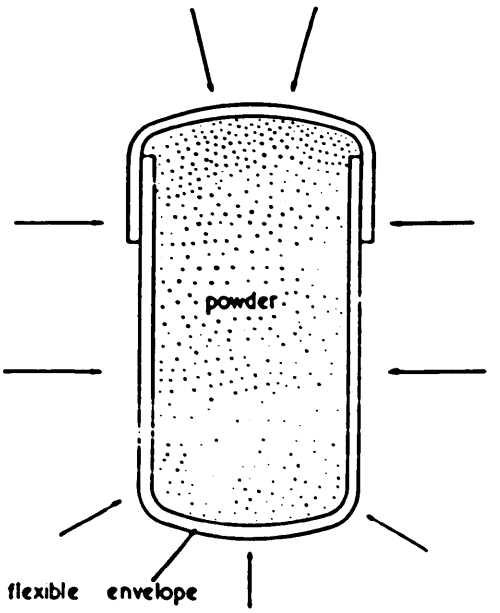

Figure 4.1 Schematic illustration of

(a) uniaxial die compaction

(b) cold isostatic compaction[64]

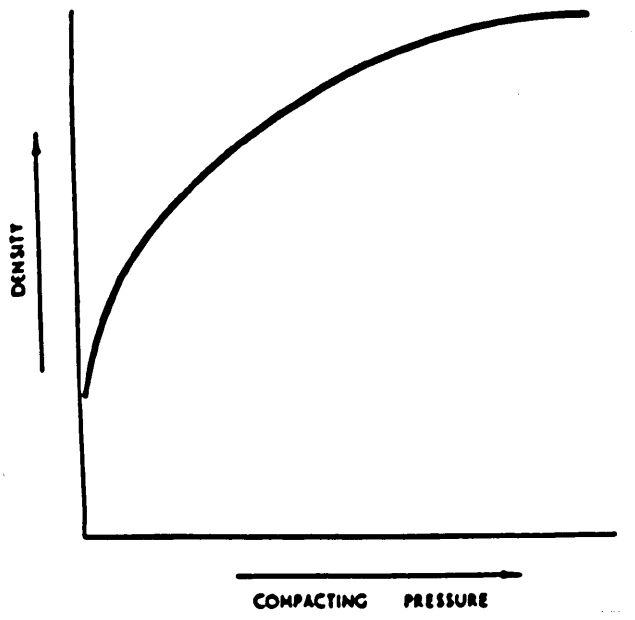

Figure 4.2 Typical pressure-density curve (uniaxial)[61].

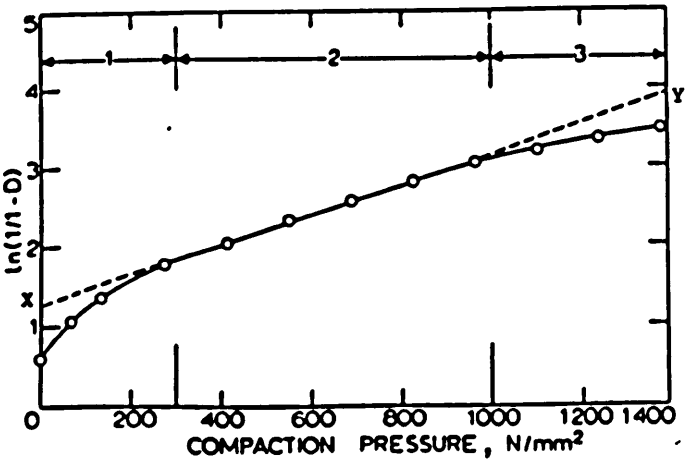

Figure 4.3 A plot of ln(1/1-D) against compaction pressure for Fe powder[70].

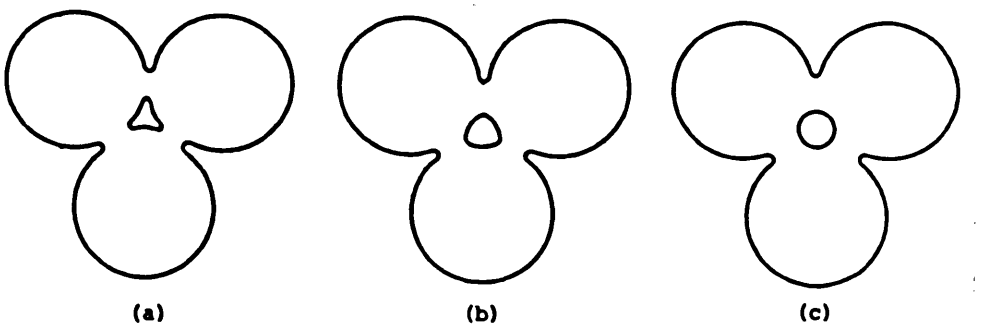

Figure 4.4 Schematic illustration of the three stages of sintering[75].

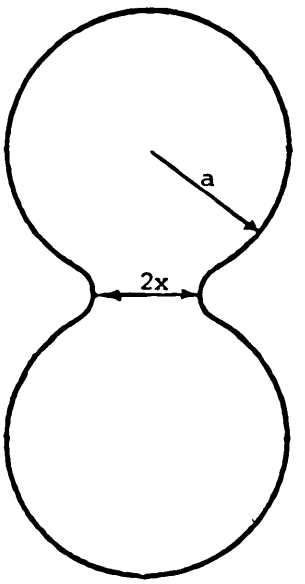

Figure 4.5 Schematic representation of two sintered spheres[76].

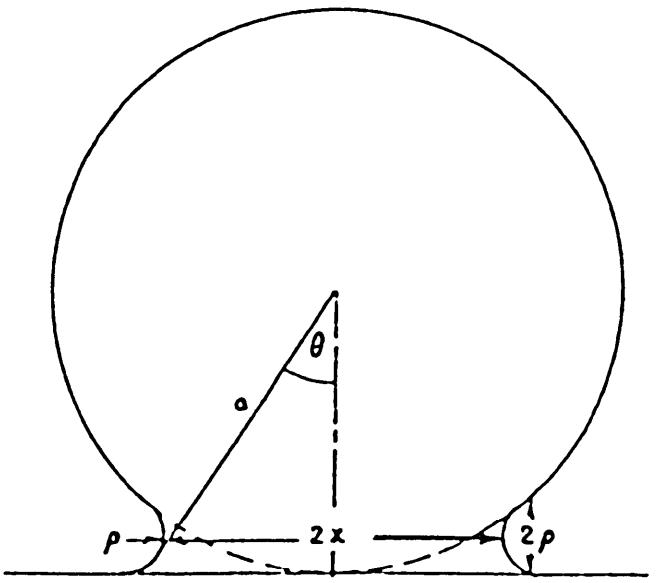

Figure 4.6 A schematic illustration of a spherical particle sintered to a flat metallic plate[79].

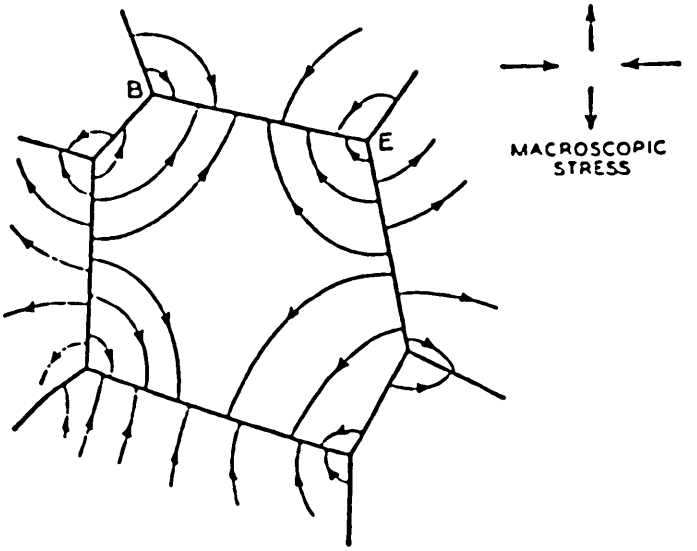

Figure 4.7 A diagrammatic representation of vacancies flow from grain boundaries under a tensile stress to grain boundaries under a compressive stress[82].

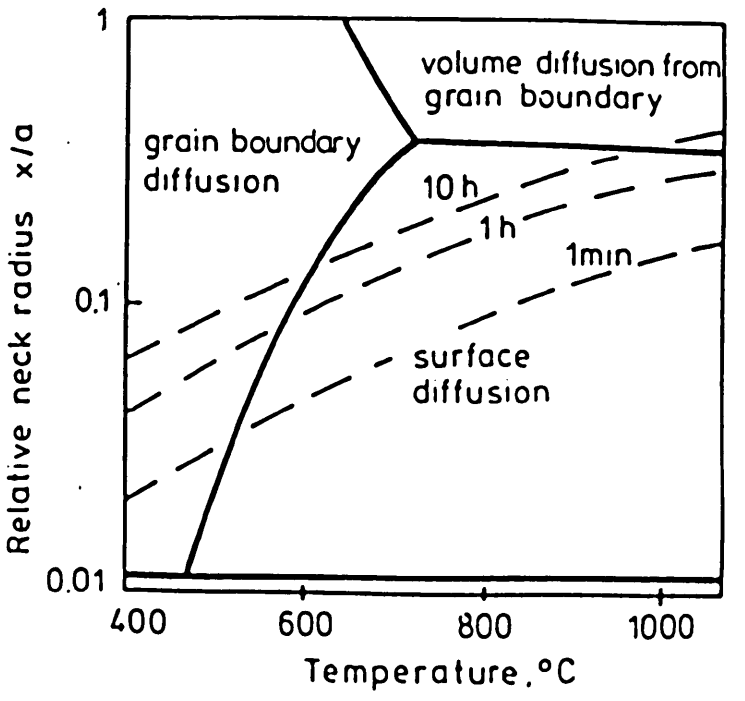

Figure 4.8 A proposed sintering diagram for two copper spheres(after Ashby)[84].

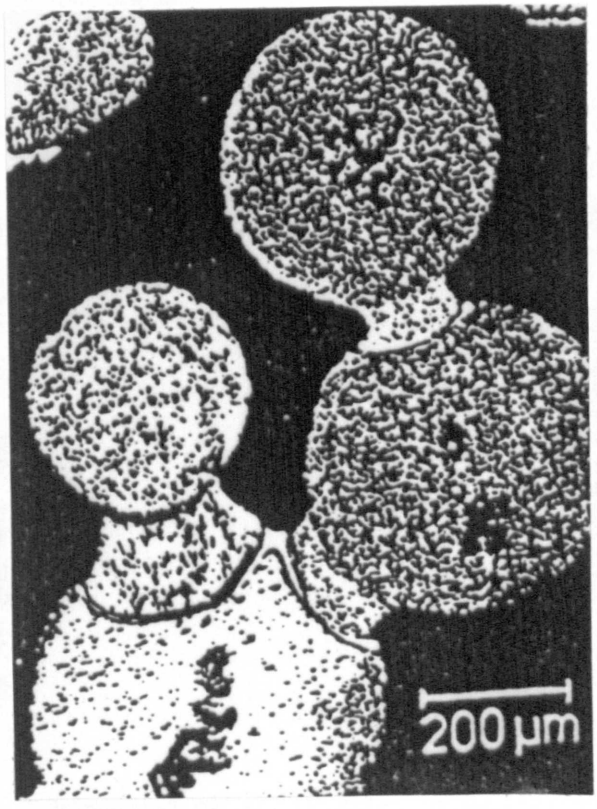

Figure 4.9 Microstructures of W-2%Ni sintered at 1640°C for 1 hr. (After Yoon and Huppmann)[97].

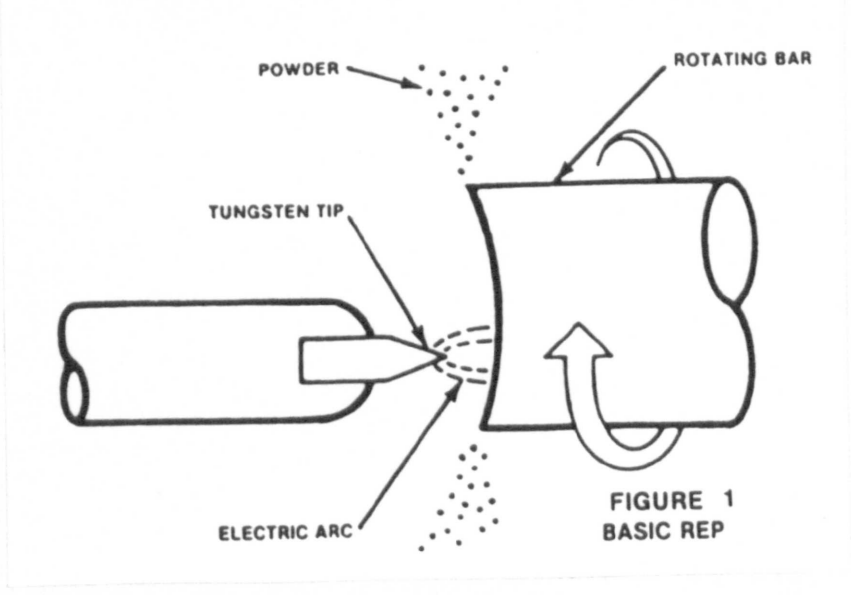

Figure 4.10 Schematic of rotating electrode process[101].

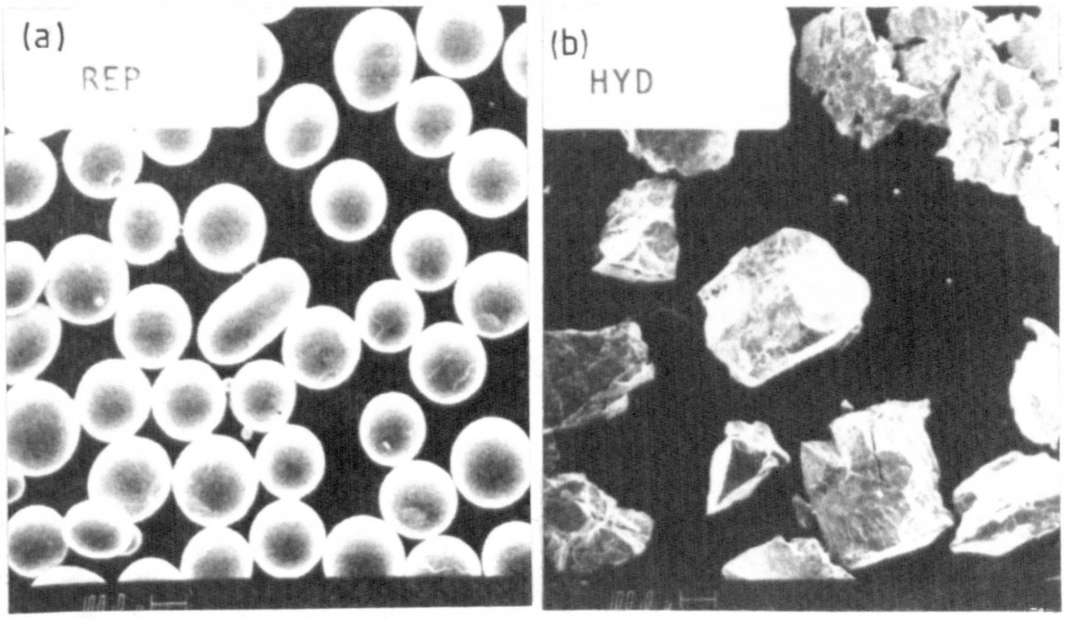

Figure 4.11 Morphology of pre-alloyed Ti-6Al-4V powder particles produced by

(a) Rotating electrode process (REP)

(b) Hydride-Dehydride process (HYD)[99].

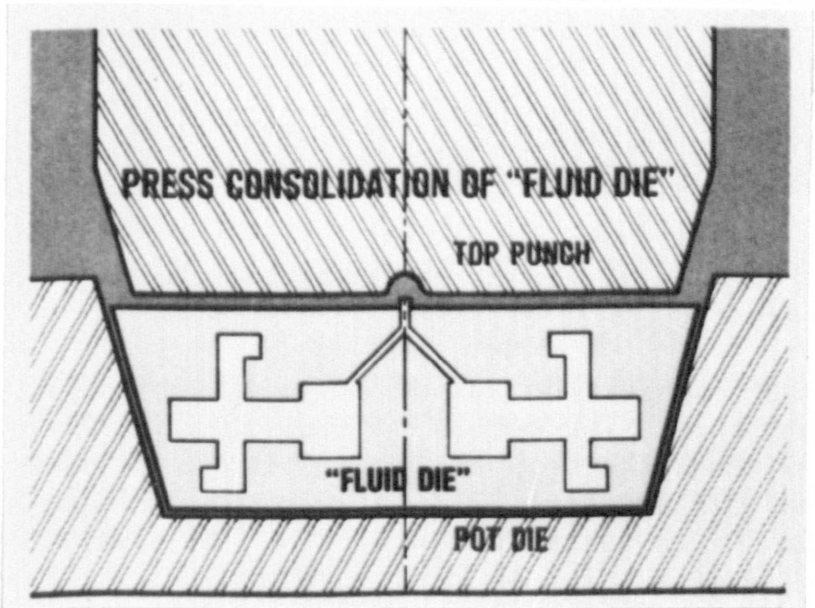

Figure 4.12 Schematic of the fluid die process[98].

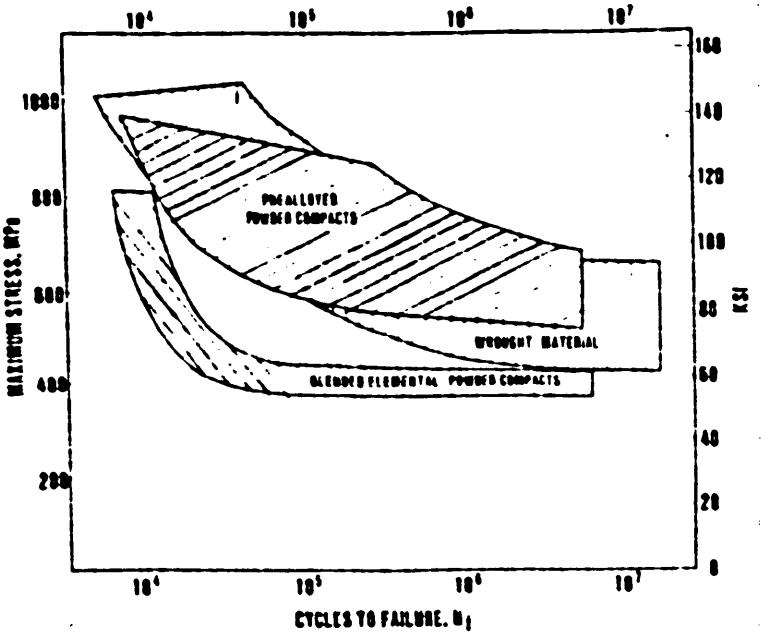

Figure 4.13 Comparison of the fatigue behaviour of Ti-6Al-4V P/M compacts with wrought material[104].

CHAPTER 5

RAPID SOLIDIFICATION PROCESSING

5.1 Introduction

The process of rapid solidification (RS) has been employed extensively for the production of alloys, ever since the pioneering work of Duwez et al[110] in 1960. The main reason for the surge of interest is the recognition that by subjecting a liquid metal to a high cooling rate of at least 10^3 Ks^{-1} during its transformation to solid, alloys which exhibit useful constitutional and microstructural modifications can be produced. It is now well established that the key factor which determines the microstructural development is the amount of liquid undercooling achieved during solidification[111,112]. There are many published reviews (e.g. Refs. 113, 114) of the work in this field and it is not the intention to present a comprehensive overview here. Instead a summary of the topics which are relevant to the present study on crystalline material will be given. This will be done under the three headings of Principles, Effects and Consolidation.

5.2 Principles of Rapid Solidification

Rapid solidification processing of crystalline alloys involves the fast removal of the latent heat of fusion from the liquid by an efficient heat sink to achieve high crystal growth velocities. There

are basically two types of heat sink - external and internal. Typical examples of externally provided heat sink include the conducting wheel in melt spinning and the convective gas used in many atomisation techniques. The effectiveness of these heat sinks is characterised by the heat transfer coefficient, h. Values of h for metal substrates vary from about 10^3 to 10^7 $Wm^{-2}K^{-1}$[115].

When a liquid metal alloy is undercooled below its liquidus temperature prior to the commencement of solidification the release of latent heat can be absorbed by the sample. This is known as an internal heat sink. During the heat absorption, the solidifying volume recalesces (reheats)[116], the temperature rising by an amount as high as c/L, where c is the heat capacity per unit volume of liquid and L the latent heat of solidification per unit volume. Recalescence stops when the temperature has risen to the equilibrium liquidus. However, if the initial undercooling, ΔT, is sufficiently high such that $\Delta T > c/L$, hypercooling occurs in which all the latent heat generated is absorbed without reheating to the liquidus temperature[117]. Consequently, there is no need for additional means of external heat extraction and the rate of crystal growth can be high. In nickel for example, the dendrite tip velocity approaches 40 ms^{-1} at 200 K undercooling (Figure 5.1)[116].

However, in conventional casting, the degree of undercooling attained is usually limited by the presence of heterogeneous nucleation catalysts. Successful development of high undercooling, therefore, relies on the suppression of crystal nucleation during cooling below the liquidus

temperature of the alloy. One of the possible means of achieving this is the subdivision of the liquid metal into small droplets (such as in atomization) to generate a large fraction of nucleant free droplets which exhibit extensive undercooling regardless of the imposed cooling rate[112].

In the case of molten layer configurations (as in melt spinning) where the geometrical shape may not have a direct effect on nucleant isolation by melt subdivision, rapid crystal growth is promoted by a combination of large undercoolings and high rate of external heat extraction[117]. In addition, there is ample evidence (e.g. Refs. 117, 118) that the undercooling increases with the cooling rate.

Hence, over the past few years, several techniques have been developed for subjecting a liquid metal to a high cooling rate during solidification. For the present study, only the chill block melt spinning technique will be considered. The principles underlying this process are shown schematically in Figure 5.2. In operation, the material to be processed is melted in the crucible and the liquid metal is ejected through a small orifice in the base by applying a top pressure of gas. The stream of molten metal then impinges on the circumferential surface of the fast rotating cold wheel. While in contact with the wheel substrate (chill block) the melt solidifies, producing a continuous ribbon which is then thrown off tangentially at a velocity of the order of 10 to 50 ms^{-1}. The quench rates achieved by this process have been shown to be between 10^3 and 10^7 Ks^{-1}[102] depending on a number of variables such as the wheel

speed and the heat transfer coefficient between the metal and the wheel material.

Most of the analyses of melt spinning have been devoted to the understanding of the effects of process variables on the dimension of the ribbon. All analyses consider a puddle of liquid metal at the foot of the stream of molten metal impinging on the rotating surface, which provides the transition from the liquid jet to the solidified ribbon. The basic relationship between the spinning variables and the ribbon dimensions is represented by the continuity equation for the volumetric flow rate of an incompressible fluid[119].

$$Q = A_r V_r = w \bar{t} V_r \qquad 5.1$$

and the Bernoulli's equation:

$$V_J^2 = \frac{2P}{\rho} \qquad 5.2$$

where Q - volumetric flow rate (given by $\frac{\pi d^2}{4} V_j$ in which d and V_j are the jet diameter and the velocity).

A_r - cross sectional area of ribbon

V_r - ribbon velocity

w - ribbon width

$\bar{t}$ - average thickness of ribbon

P - ejection pressure

ρ - density

The mean ribbon thickness, $\bar{t}$, is obtained from the expression $\bar{t} = m/(\ell w \rho)$ where ℓ and m are the ribbon length and mass respectively. The value of $\bar{t}$ so determined may differ significantly from that measured with a micrometer. This difference is related to the non-uniform spreading of the liquid stream on the wheel. The possible causes of dimensional variations in the spun ribbon have been discussed in some detail[120]. Identified causes include periodic vibrations of the melt puddle, and temporal changes in the heat transfer coefficient due to metal debris on the wheel surface and entrapped gas.

By combining equations 5.1 and 5.2, the following expression for the area of ribbon is obtained:

$$A_r = \frac{\pi d^2 P^{1/2}}{2^{3/2} V_s \rho^{1/2}} \qquad 5.3$$

where V_s is the wheel velocity. This equation predicts a linear relationship between A_r and $\frac{d^2 P^{1/2}}{V_s}$ which is consistent with the experimental results of Charter et al[119] on crystalline alloys (e.g. Al-2% Fe, Figure 5.3). Data from a number of chill block melt spinning experiments indicate that the average thickness of crystalline ribbon is given by[102,121]:

$$\bar{t} = \frac{K_1 d}{V_s} \qquad 5.4$$

where the proportionality factor, K_1 depends on the physical properties of the liquid and chill block, melt superheat, chill block

surface finish, and the angle between the normal to the chill block surface and the jet.

Liebermann[122] has obtained an empirical relationship between ribbon width, w and the volumetric flow rate, Q from a study of a variety of melt spun Fe-Ni based amorphous materials:

$$w = w_o + Q\, V_p \qquad 5.5$$

where w_o and V_p are constants. He interpreted V_p as the dynamic viscosity in the melt puddle and found the value to be relatively constant at 1.0 to 1.1 x 10^{-3} m^2 sec^{-1} for the range of alloys investigated. The experimentally determined width/flow rate data by Charter et al[119] for a number of crystalline alloys (e.g. Al-2% Mn) are also in reasonable agreement with equation 5.5. Thus, the fundamental parameters governing ribbon dimensions, which in turn control the cooling rate are liquid flow rate and wheel velocity.

Under the conditions of Newtonian cooling, the cooling rate, varies inversely with the ribbon thickness according to the following relationship[123]:

$$\dot{\varepsilon} = \frac{h_i\, K\, (T - T_s)}{k\, t} \qquad 5.6$$

where h_i - interfacial heat transfer coefficient

K - thermal diffusivity

T - instantaneous temperature of puddle

T_s - substrate temperature

k - thermal conductivity of puddle

t - puddle thickness.

Newtonian cooling conditions refer to the case in which the heat transfer coefficient has a low value (e.g. 10^4 Wm^{-2} K^{-1}) in contrast to ideal cooling conditions where h has a value approaching infinity[124,125]. In most rapid solidification techniques the values of h vary from about 10^3 to 10^7 $Wm^{-2}K^{-1}$[115], hence Newtonian cooling conditions are usually asssumed. However, a quantitative differentiation between the two cases is obtained by determining the dimensionless Nusselt number, Nu which is given by $Nu = h_i t/k$. Cooling is ideal when $Nu > 30$ and is Newtonian when $Nu < 0.015$[124]. Intermediate cooling conditions lie between these two values.

Techniques based on microstructural features, for determining cooling rates; and hence undercooling, have gained considerable attention in recent years (e.g. Ref. 123). The most employed features are secondary dendrite arm spacing and eutectic cell spacing. Results from a number of theoretical and experimental studies (e.g. Refs. 116,117,123,125) support the following relationships:

$$d_2 = B_1 \dot{\varepsilon}^{-n} = B_2 t_f \qquad 5.7$$

$$\dot{\varepsilon} = V_g G \qquad 5.8$$

$$\lambda = B_3 V_g^{-1/2} \qquad 5.9$$

$$\lambda = B_4/\Delta T \qquad 5.10$$

and $$V_g = B_5 \Delta T \qquad 5.11$$

where d_2 - secondary dendrite arm spacing

$\dot{\varepsilon}$ - average cooling rate during solidification

t_f - local solidification time

λ - eutectic cell spacing

ΔT - undercooling at the solidification front

V_g - growth velocity

G - temperature gradient at the liquid - solid interface

and n, B_1, B_2, B_3, B_4 and B_5 are constants.

The importance of the role of undercooling in controlling crystal growth velocity and consequently the microstructural features is apparent from the above relationships. For example, the dendritic growth velocity for Al-8 wt-% Fe alloy is related to undercooling by the following expression[117]:

$$V_g = 1.49 \times 10^{-4} \Delta T^{2.84} \qquad 5.12$$

Experimental data (validating Eq. 5.9) from a number of studies showing the dependence of eutectic spacing on growth velocity for Al-Al_2Cu are shown in Figure 5.4[116].

5.3 Effects of Rapid Solidification Processing

Solidification at increasingly high crystal growth velocities results in progressive departure from equilibrium microstructures. The effects of concern in the present research on crystalline TiNi shape memory alloys which undergo a martensitic phase transformation are:

(i) Refinement of grain size
(ii) Increase in point defect and dislocation concentration
(iii) Suppression or modification of the order - disorder reaction.

These will now be considered in turn.

5.3.1 Refinement or Grain Size

Rapidly solidified crystalline alloys typically show grain sizes between 0.1 to 10 μm depending on the technique and the degree of undercooling achieved during solidification. These are smaller than those that can be obtained by a grain refining operation in conventional casting. The microstructural refinement of RS material is related to the higher level of undercoolings attained prior to crystalline solidification. A substantial undercooling before solidification can significantly affect the grain size. For example, Walker[126] studied the influence of melt undercooling on the grain size of pure nickel by using a glass encasement to prevent the metal from being nucleated by crucible walls. He found that at undercoolings up to approximately 140 K the specimen contained only a

few grains, whereas at an undercooling of about 150 K there was a sharp decrease in grain size. A similar result (Figure 5.5) has also been reported for nickel-base alloys by Skolianos et al[127], who in addition observed that the dendrite arm spacing decreases with increasing undercooling.

The grain refinement caused by RS processing can have some effects on the transformation behaviour of martensitic alloys. It is well known that grain boundaries can act as effective obstacles to martensite formation as a result of the extra energy needed for complementary shear during transformation[21]. Thus, fine grained material with higher grain boundary area would be expected to give a lower transformation temperature, M_s than the corresponding coarse grained specimen. The results of Sastri and West[128] from a study into Fe - C - Ni - Cr - Mo alloys are shown in Figure 5.6 in which the M_s and the grain size simultaneously increase with austenitizing temperature. In another investigation on Fe - Ni - C alloys, Inokuti and Cantor[129] found the M_s temperature of fine-grained (0.5 - 1 μm) rapidly solidified samples to be considerably lower by as much as 200 K, when compared with those of coarse grained (40 - 60 μm) wrought specimens. A similar depression in M_s as a result of grain refinement has also been observed by Wood and Shingu[130] in Cu-base shape memory alloys (e.g. Cu-Ni-Al). There are other parameters which could influence the transition performance as a result of rapid solidification processing. These will be considered in the following sections.

Apart from its effect on M_s temperature, grain refinement decreases the amount of recoverable strain in shape memory alloys as pointed out in section 2.4.3. For example, Wayman[10] found the recoverable strain limit of single crystal Cu-39.8 wt-%Zn specimens to be considerably higher (about 11%) than that (around 3%) of polycrystalline samples with an average grain size of .25 mm.

5.3.2 Increase in Point Defect Concentration

The equilibrium concentration of vacancies, C_v in a solid at any temperature, T is given by:

$$C_v = \exp(\Delta S_v/k).\exp -(\Delta H_v/kT) \qquad 5.12$$

or $$C_v = \exp -(\Delta G_v/kT) \qquad 5.13$$

since $$G_v = \Delta H - T.\Delta S_v \qquad 5.14$$

where ΔS_v - entropy change on adding vacancies

ΔH - change in enthalpy per mole of vacancies increase

k - Boltzmann's constant

ΔG_v - thermal energy required to displace an atom from its lattice site.

Thus, the equilibrium concentration of vacancies increases exponentially with temperature and reaches a value of about 10^{-4} - 10^{-3} at the melting point of most solids. For example, C_v for

aluminium at the melting point is 9.4×10^{-4}[131]. When a metal is slowly cooled from a high temperature, the vacancies will migrate to a number of sinks (such as grain boundaries). However, when the material is rapidly quenched from a high temperature, there may be insufficient time for a new equilibrium concentration to be established, and consequently, a supersaturation of vacancies exists at the lower temperature. This quenched-in vacancy density would be expected to increase with quenching temperature for a given alloy and cooling conditions.

Experimental study by Rastogi and Mukherjee[132] on lead has shown that the degree of supersaturation of vacancies is even higher when the sample is rapidly cooled from the liquid state instead of the solid state at the melting temperature (Figure 5.7). A similar result has also been reported for aluminium by Thomas and Willens[133].

Some of these vacancies may be attracted together into vacancy clusters which can subsequently collapse and result in high dislocation densities. Dislocation loops characteristic of the break down of excess vacancies quenched-in from the melt have been observed by Wood and Honeycombe[134] in splat quenched Fe-25% Ni-20% Cr austenitic stainless steel. Further evidence has come from the work of Smallman[135] on quenched Al-6%Mg. The retention of this excess vacancy supersaturation depends on maintaining a high quench rate throughout the cooling process. It has been shown by a number of workers (e.g. Ref. 130, 136) that while the quench rate during rapid solidification process can be quite high (e.g. 10^5 Ks^{-1}), subsequent

cooling to ambient temperature can be relatively low. It is therefore likely that a proportion of the excess vacancies could anneal out to sinks.

In alloys that undergo the martensitic reaction, higher vacancy density may affect the transformation behaviour. Wood and Shingu[130] have studied the effect of vacancy concentration on the transformation behaviour of Cu-base shape memory alloys. Their results show that a large vacancy density serves to increase the characteristic transformation temperatures. In certain alloys such as nickel-base superalloys, it has been reported that a rise in vacancy concentration increases their tendency to decompose spinodally[136].

Another RS effect which could influence the transition response of martensitic alloys is the increase in dislocation density. It has been demonstrated[24] that the strain field associated with a dislocation can enhance martensite formation by providing a favourable interaction with the strain field of a martensite nucleus, thereby resulting in an increase in M_s. There is however, a possibility that nuclei growth is suppressed by dislocations[21]. It is not known which of these two effects dominates.

5.3.3 Suppression or Modification of the Order - Disorder Reaction

When an alloy which undergoes a solid state order - disorder reaction is quenched from a temperature above the ordering transition temperature range, there is a possibility of partially suppressing the

transformation since it is a diffusion controlled process. For instance, Tadaki and Shimizu[137] have studied the Fe_3Pt alloy and found some weak and blurred superlattice spots (such as 010) in the electron diffraction pattern of samples quenched from 1000°C. On reheating the specimen at 650°C for 30 min. after being quenched from 1000°C, the sharpness and intensity of the superlattice increases indicating the development of ordering. Suppression of the ordering reaction as a result of rapid solidification has also been reported by Perkins[138] in CuZnAl shape memory alloys. In addition, Perkins studied the effect of ordering on the transformation response of the alloys and found that the M_s temperature rises with increasing degree of ordering.

5.4 Consolidation of Rapidly Solidified Materials

Since the conditions that give rise to the high cooling rates for large undercooling are mainly met in materials of thin section, rapidly solidified products are usually in the form of powder, ribbon or fibre. Although there may be some applications in which such material of small cross-section can be employed directly in the "as solidified" state, powder metallurgy techniques have been commonly used to consolidate them into bulk engineering components. Several consolidation methods in commercial production (e.g. pressing and sintering, hot isostatic pressing, hot extrusion, and hot forging) and more novel techniques (for example, explosive compaction) which are in laboratory scale development, have been employed.

There is now overwhelming evidence that such subsequent processing does not necessarily impair the fine grain structure achieved by rapid solidification. Indeed, it has been convincingly demonstrated by a number of workers that rapidly solidified products can be more resistant to grain coarsening than those processed by conventional methods. For example, Suga et al[139] have studied the grain coarsening resistance of a series of rapidly solidified, and conventionally produced austenitic steels (e.g. Fe-9Ni-4Co). Their results show that while the conventionally prepared specimens coarsen to a grain size of several hundred microns, the rapidly solidified sample maintains a grain size of about 20 μm after the 1200°C heat treatment. Slaughter and Das[140] have also reported that fine grained (1 - 2 μm) Fe-Al-Ti-B alloys containing a large density (2×10^{14} particles/cm^3) of uniformly dispersed TiB_2 fine particles (about 600 Å mean diameter) can be obtained by hot isostatic pressing and thermomechanical processing of rapidly solidified materials. A similar observation has been reported by Gagg, Bee and Wood[141] in their investigation into the compaction and sintering behaviour of a number of RS Fe-Ni-V and Fe-Mn-V steels produced by the melt extraction technique. The bulk of the experimental evidence suggests that the resistance to grain growth of RS specimens is due to particle-pinning of grain boundaries. The particles result from the decomposition of the metastable phases, produced by rapid solidification during subsequent heat treatment.

The mechanical properties (yield strength and ultimate tensile strength) data from the work of Ray and Clemm[142] on hot

consolidation of rapidly solidified Ti-6Al-4V-1B alloy are presented in Figure 5.8. It is evident that substantial improvements in mechanical properties can be achieved by choosing the RS route instead of conventional methods. Thus, the combination of rapid solidification with the concomitant structural refinement, and powder metallurgical processing with the associated ease of producing near-net shapes offers a great potential for making components with improved properties.

5.5 Summary

Rapid solidification of crystalline alloys involves the rapid removal of the latent heat of fusion from a molten metal by an effective heat sink to achieve high crystal growth rates. If substantial undercooling can be established prior to solidification, all the latent heat generated can be absorbed by the solidifying sample without the need for additional means of external heat extraction. In practice, however, the degree of undercooling is usually limited by the presence of heterogeneous nucleation catalysts in the liquid metal. High crystal growth rate can be promoted by a combination of large undercoolings and high rate of external heat removal. In substrate quenching such as melt spinning, the rate of heat extraction is determined by the heat transfer coefficient between the substrate and the molten alloy, and the ribbon thickness. The latter is dependent on a number of process variables such as the wheel speed and the liquid flow rate.

Solidification with increasingly higher interface velocities results in progressive departure from equilibrium microstructures. Among the possible effects of rapid solidification processing are grain refinement, increase in point defects concentrations and suppression of the order - disorder reaction. In alloys that subsequently undergo a martensitic transformation, grain refinement and suppression of the order - disorder transition can lead to a decrease in M_s temperature, whereas an increase in vacancy density would have the opposite effect. The M_s of a rapidly solidified material would depend on the relative contribution of these parameters.

Rapidly solidified product can be consolidated by powder metallurgy methods without necessarily destroying the fine grain structure of the starting material.

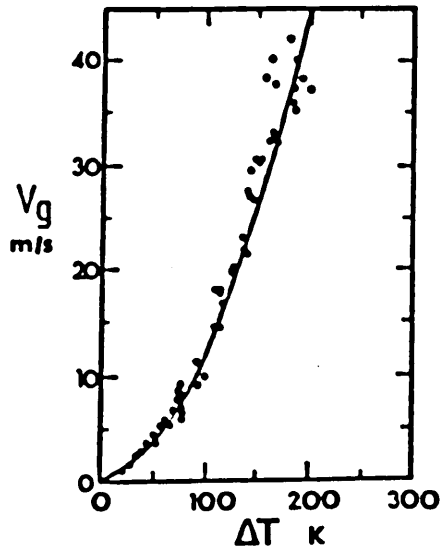

Figure 5.1 Dependence of dendrite tip velocity on undercooling in nickel melts[116]

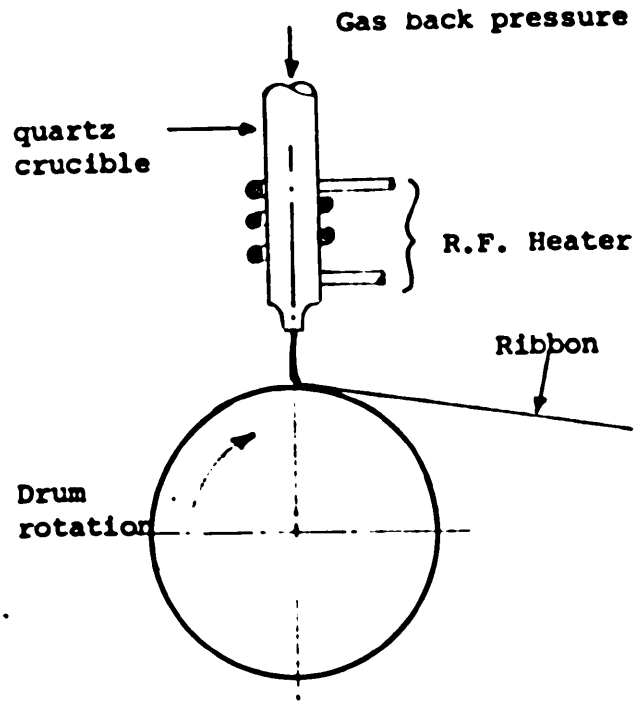

Figure 5.2 Chill block melt spinning.

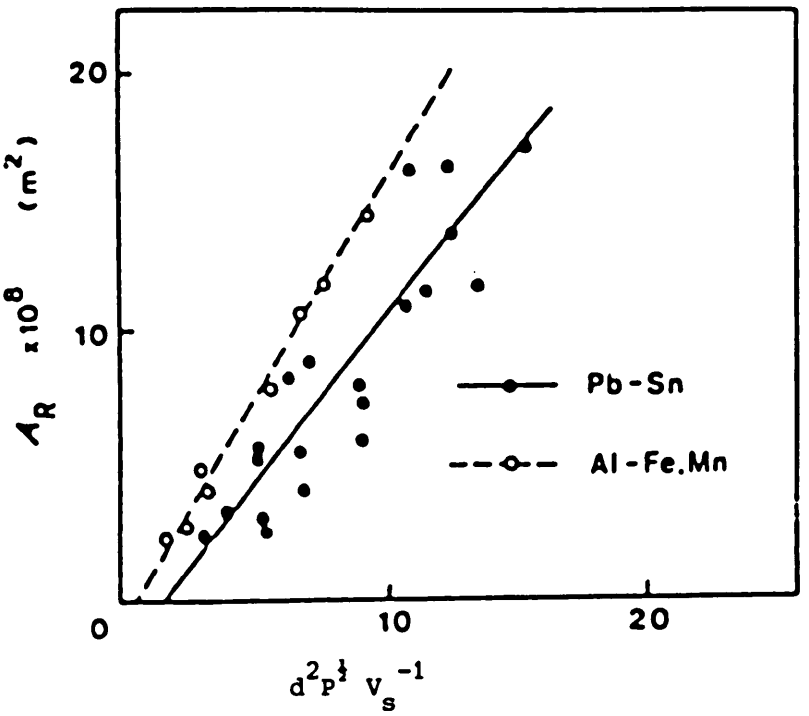

Figure 5.3 Ribbon cross-sectional area A_r as a function of $d^2P^{1/2}V_s^{-1}$ for melt spun crystalline Sn-Pb and Al-(Fe, Mn)[119].

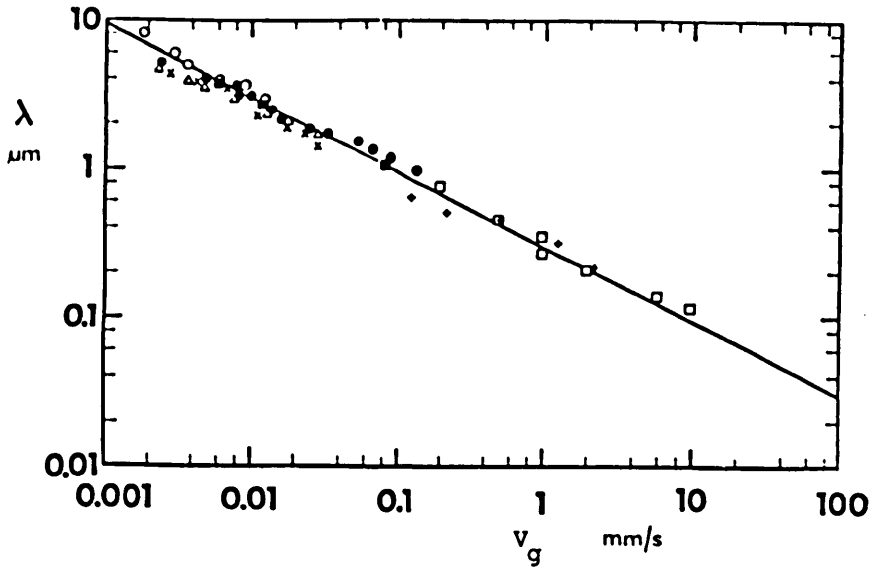

Figure 5.4 The dependence of eutectic cell spacing λ on growth velocity V_g for Al-Al_2Cu[116].

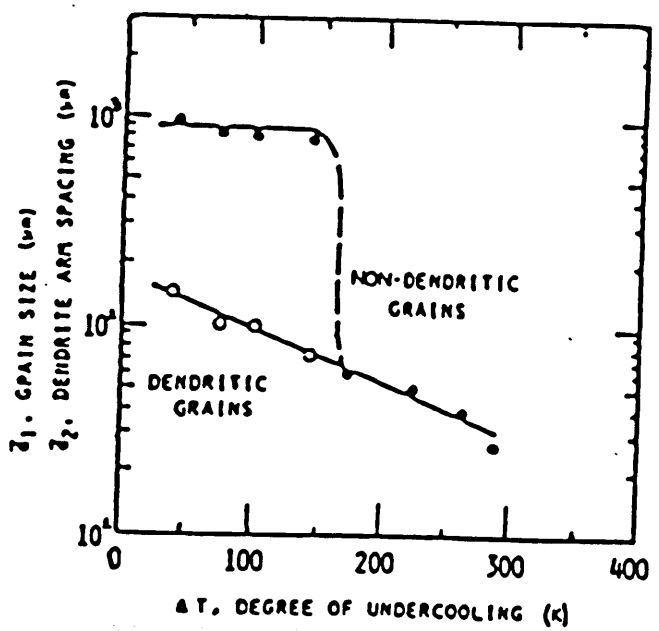

Figure 5.5 Dendrite arm spacing (o) for dendritic specimens and grain size (•) for both dendritic and non-dendritic specimens vs. degree of undercooling for Ni-25 wt % Cu-0.2 wt % Ni-25 wt % Cu-0.2 wt % alloy[127].

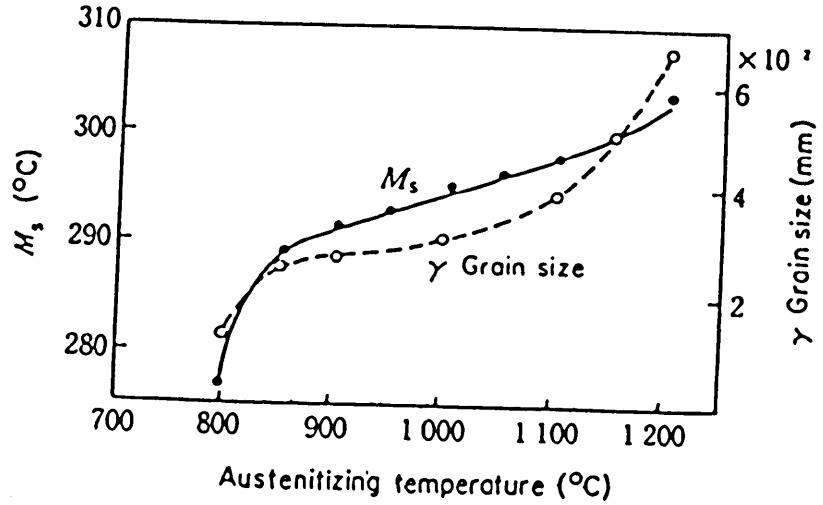

Figure 5.6 Variation of M_s temperature and austenite grain size with austenitizing temperature for Fe-0.33% C-3.26%Ni-0.85%Cr-0.09%Mo alloy[128].

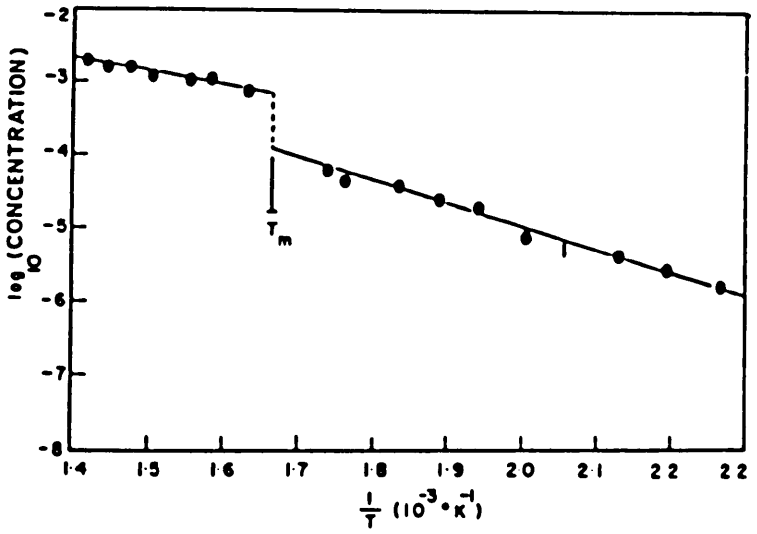

Figure 5.7 Quenched-in vacancy concentration as a function of inverse quenching temperature T for lead.

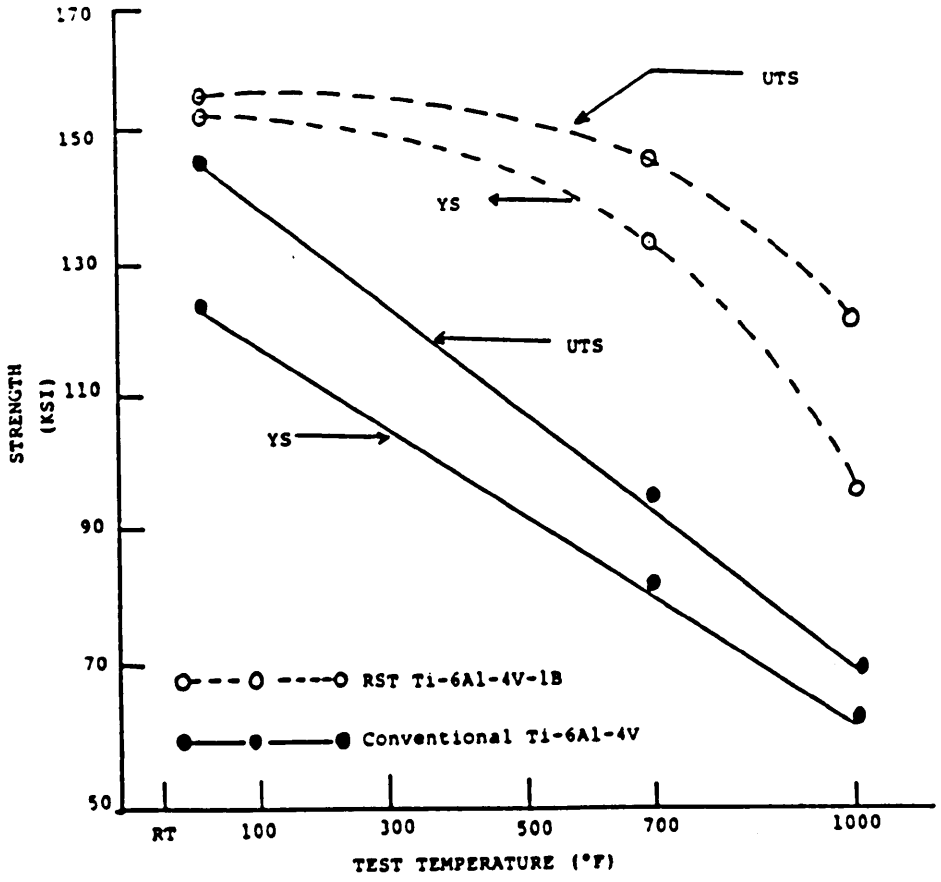

Figure 5.8 Yield and ultimate tensile strength of consolidated RS Ti-6Al-4V-1B and conventional Ti-6Al-4V as a function temperature.

CHAPTER 6

EXPERIMENTAL DETAILS

6.1 Introduction

The aim of the present research was to investigate the properties of Ti-Ni shape memory alloys produced by both powder metallurgy and rapid solidification techniques. The work was performed in four different stages:

(i) Investigation of the effects of compaction pressure, sintering temperature, and powder particle size on density and dimensional change of elemental powder compacts. Effect of hot isostatic pressing on the density of sintered compacts was also examined.

(ii) Determination of the properties of pressed and sintered specimens. The properties investigated are hardness, transformation behaviour and tensile strength.

(iii) A study of the effect of rapid solidification process on the properties of TiNi alloy. The properties looked at included grain size, transformation behaviour and hardness. The influence of heat treatment on these properties was also examined.

(iv) An investigation into the consolidation of rapidly solidified material. The results obtained were compared with those of elemental powders.

In the following sections, a detailed account of the starting materials, specimen preparation, rapid solidification processing and the techniques used to characterise the samples is presented.

6.2 Materials and Preparation

The base powders employed throughout the present work were titanium sponge fines (-150 μm with irregular shape) obtained from Deeside Titanium and Inco 123 carbonyl nickel powder (3-7 μm, fine spiky particles) supplied by Inco International. Typical characteristics of the nickel powder are shown in Table 6.1. The titanium powder size distribution was obtained using a standard set of 200 mm BS sieves.

Powders were blended for the equiatomic composition (Ti-50 at -% Ni) by tumbling in a cylindrical plastic jar for one hour using a laboratory mixer. The effect of titanium particle size was studied by sieving some powder into seven size fractions (i.e. 137.5, 115.5, 98, 82.5, 69, 50.5 and 27.5 μm) before mixing.

Table 6.1 Characteristics of Inco 123 Nickel Powder

Particle size (Fisher), μm	3-7
Apparent density, Mgm^{-3}	1.6-2.6
Specific surface area, m^2g^{-1}	0.3

6.3 Powder Pressing

Powders were cold compacted to cylindrical shape specimens using either a floating die assembly on a hydraulic press (uniaxial) or cold isostatic pressing. Since the usual metallic stearate lubricants used in conventional powder metallurgy have the effect of contaminating titanium powder, all pressing was performed without lubricant. Compaction pressures ranged from 155 to 929 MPa for uniaxial die pressing and 171 to 503 MPa for isostatic compaction. Each die pressed sample weighed 4 grams with a diameter of 12.7 mm and the height varied from 5.8 to 8.4 mm depending on the compaction pressure applied. The weight of each isostatically pressed specimen was 6 grams. Since these compacts were not of uniform cylindrical shape, they were subsequently machined into discs before making dimensional measurements. Densities of "green" (unsintered) compacts were determined from weight and dimensional measurements which were accurate to within ± 0.001 g and ± 0.001 mm respectively. Tensile test specimens of the the 'dog-bone' geometry shown in Figure 6.1 were made using a floating die pressing.

6.4 Sintering and Heat Treatment

All sintering experiments were undertaken in a horizontal tube furnace under a vacuum of 10^{-3} Pa for a standard time of 5 hours unless otherwise stated. The furnace consists of a resistance wire wound onto a refractory tube, a oil-diffusion pump backed by a rotary

pump, a specimen thermocouple and a temperature control equipment which measures and regulates the temperature of the tube. The furnace could be used at temperatures up to 1200°C. In the present study, the temperature in the hot zone of the furnace was monitored by means of a platinum/platinum-rhodium thermocouple placed inside the furnace tube just above the compacts. Temperature was maintained to within ± 2°C.

To sinter a batch of compacts, the samples were placed in the central hot zone of the tube at room temperature. The tube end cap was replaced and the furnace evacuated to a vacuum of 10^{-3} Pa before switching on the power. The heating rate was about 10°C min^{-1}. First trial samples suffered from low temperature melting due to the evolution of heat during the formation of Ti-Ni intermetallics. This problem was overcome by raising the desired temperature in steps of 50°c at temperatures above 800°C, where the specimens were susceptible to premature melting. The aim of this was to decrease the heating rate during heating above 800°C. The sintering temperature ranged from 600°C to 1150°C. After sintering for the desired period, the power was turned off and the compacts allowed to cool to room temperature in the furnace before turning off the vacuum pumps. The changes in the radial and axial dimensions of the cylindrical compacts, due to sintering, were determined by subtracting the values observed before sintering from the corresponding values obtained after sintering and the results were expressed as percentages of the former.

All further heat treatments of sintered samples were performed in sealed quartz capsules which had previously been evacuated to

10^{-3} Pa. Some sintered specimens were sent to HIP (Powder Metals) Ltd., for hot isostatic pressing. They were encapsulated in mild steel tubing and HIPped for 3 hours at 950°C using a pressure of 15000 psi (103 MPa). Decanning was achieved by machining.

6.5 Production of Rapidly Solidified Materials and Prealloyed Powder

Rapidly solidified material was produced by the chill block melt spinning technique described in Section 5.2 (Chapter 5). In the present investigation about 10 grams of equiatomic titanium-nickel compacts which had previously been prepared by compaction and sintering of elemental powders were used as the feed stock material for each run. The apparatus was enclosed in a chamber which was first evacuated to 10^{-2} Pa and double flushed with argon. The chamber was then back filled to a pressure of 65 kPa with argon prior to melt spinning. The quartz tube crucibles had an orifice diameter of 0.8 mm. A radio frequency induction coil was used to generate the heat for melting. A pressure of 100 kPa was employed to eject the liquid alloy on to a 230 mm diameter water cooled 70:30 brass wheel. A peripheral wheel speed of 27 ms^{-1} was maintained for all experiments. The spun ribbons were about 3 mm wide and up to 50 μm in thickness.

Some ribbons were subsequently chopped to between 1 and 4 mm long followed by grinding for 5 hours in a vibratory mill. In view of the ductile nature of the ribbons, only a fraction of the charge could be converted into powder. The yield can be much enhanced by a hydriding-dehydriding processing described in Section 4.4 (Chapter 4).

For the purpose of the present research, however, the prealloyed powder produced by direct ball milling of the solidified ribbon was sufficient. The powder was screened through a 150μm sieve. The apparent density, tap density and sieve analysis for the prealloyed powder were determined.

6.6 Determination of Tensile Strength and Hardness

Tensile tests were performed on 'dog-bone' shaped (Figure 6.1) sintered samples using an Instron machine equipped with a chamber for testing at temperatures below and above room temperature. Test temperatures were varied from - 60 to 140°C. Specimens were pulled to fracture at a cross-head speed of 1.0 mm min^{-1}. The ultimate tensile strength for each sample was determined by dividing the maximum load sustained before fracture by the original area within a specimen gauge length of 25.4 mm.

Vickers hardness and microhardness tests were conducted on polished specimens using 10 kg and 100 g loads respectively.

6.7 Transformation Characteristics

The transformation temperatures on heating and cooling of melt spun and sintered materials were determined on a DuPont 1090 differential scanning calorimeter (DSC). In the DSC, a sample to be analysed and an inert reference are heated at a constant rate over a

range of temperatures. When a heat-related change (e.g. melting, or transition from one crystalline form to another) occurs in the specimen, heat is either liberated or absorbed. A signal proportional to the heat flow required to maintain the specimen and the inert reference at the same temperature is fed into a recorder producing a plot of heat flow against temperature. Thus allowing the determination of transition temperatures and enthalpy of reaction.

In the present study, an aluminium pan was used as the inert reference. The specimens were cycled between -100 and 200°C at a programmed heating and cooling rate of 20°C min^{-1} under a constant argon flow of 0.3 ℓ min^{-1}. A standard sample size of 20 mg was employed throughout. The cooling runs were performed by placing a metal can containing liquid nitrogen onto the cell block and allowing the DSC to supply the necessary amount of heat to maintain the pre-programmed cooling rate. Typical DSC plots are shown schematically in Figure 6.2 where the characteristic temperatures M_s, M_f, P_s and P_f have been defined as corresponding to the temperatures at which the curve departs from the base line.

6.8 Structural Analysis

Metallographic examination was performed on polished and etched surfaces using a Philips 501 B scanning electron microscope (SEM). Green and sintered cylindrical compacts were sectioned along a diameter and mounted. Considerable care was required to avoid smearing during polishing, especially for green compacts and samples

sintered at low temperatures. Etching was undertaken in a mixture of 5% HF, 5% HNO_3 and water. SEM fractographs of tensile test pieces were also obtained.

Discs specimens of 3 mm diameter for transmission electron microscopy were cut from melt spun ribbons and polished in a Struers Tenupol jet apparatus. Polishing was performed at - 50 to -60°C under an applied potential of 20 volts and a current of 20 mA using 7:2:1 methanol: glycerol: perchloric acid electrolyte. Discs made from sintered samples could not be successfully thinned because of porosity. Structural observation of thinned foils of spun ribbon was conducted in a Philips 301 transmission electron microscope, operated at 100 KV.

X-ray diffraction analysis was undertaken using a Debye-Scherrer powder camera. The thin strip samples were mounted by adhesive paste and exposed for 8 hours. Cu Kα radiation was employed with a Ni filter. The diffraction lines were measured by a vernier instrument to within ± 0.05 mm.

6.9 Diffusion Couple

From the analysis of the microstructural results of sintered elemental blend compacts, it was thought necessary to conduct a diffusion couple experiment in order to obtain a better understanding of the interdiffusion characteristics of titanium and nickel powders. The usual method for making a diffusion couple is to first heat treat

the starting materials for several days at a temperature high enough to cause considerable grain growth sufficient to render grain boundary diffusion negligible. In the present instance, however, the diffusion couple was prepared using two discs 10 mm diameter and 5 mm thick, machined from pressed and sintered pure titanium and nickel compacts. These starting materials with a fine grain structure were used in order to simulate actual behaviour in the sintered elemental blend compacts. The discs were polished and rinsed in acetone before clamping between steel plates. In order to prevent the couple and the steel plates from welding together during the diffusion treatment, a few drops of alcohol containing alumina particles were applied to the outside surfaces. The couple was diffusion-bonded at 800°C in a vacuum furnace for 2 hours and then cooled to room temperature. The steel plates were removed and the sample was diffusion-annealed at 900°C for 72 hours in a vacuum furnace.

Finally, the specimen was sectioned and prepared for microstructural investigation. The variation of composition across the diffusion zone was monitored by energy dispersive x-ray analysis.

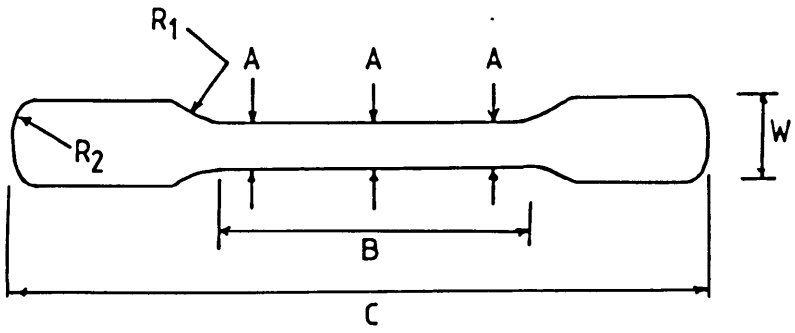

Figure 6.1 Geometry of tensile test piece

$A = 3.44 \pm 0.02$, $B = 20 \pm 0.5$, $C = 54 \pm 0.5$, $W = 5.2 \pm 0.5$,

$R_1 = 15$, $R_2 = 2.6$ (all dimensions in mm), (area = $235.65 mm^2$).

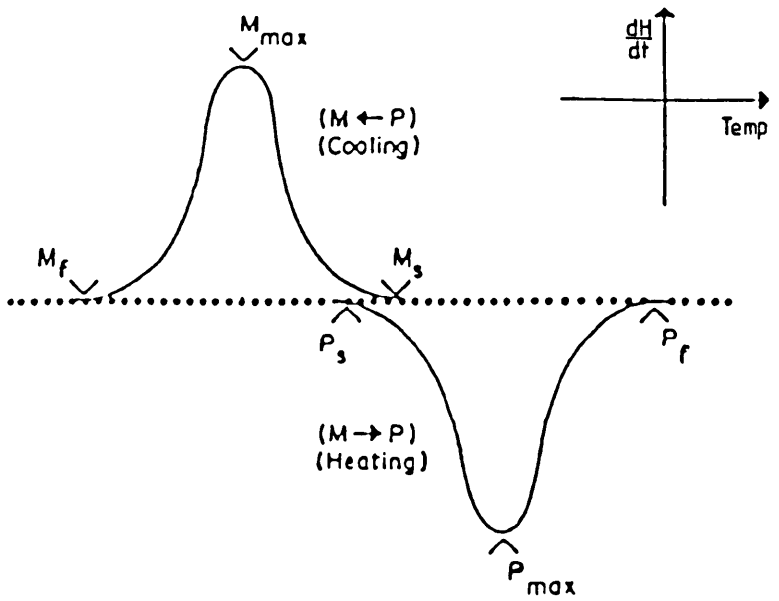

Figure 6.2 Schematic differential scanning calorimeter curves illustrating the characteristic transformation temperatures.

CHAPTER 7

COMPACTION AND SINTERING OF TITANIUM-NICKEL ELEMENTAL POWDERS

7.1 Introduction

One of the main distinguishing features of pressed and sintered materials is their porosity which often has a dominating influence on mechanical properties. An increase in density (i.e. a decrease in the level of porosity) generally leads to a rise in tensile strength, fracture toughness and resistance to fatigue crack growth[143].

In the present chapter, the results of an investigation into the effect of powder characteristics, compaction pressure and sintering temperature on density of sintered Ti-Ni compacts of equiatomic composition are presented. In addition, the study was set out to determine the influence of these experimental variables on the dimensional change of sintered compacts. It is generally observed that soft pure metal powder compacts shrink during sintering (e.g. Refs. 144,145). However, in the case of a mixture of two or more distinct elemental powders in which alloying and sintering proceed simultaneously, compact growth can occur. An outstanding example from industrial powder metallurgical practice, is a blend of iron and copper in which the mechanisms for compact growth are well established[146,147]. For titanium-nickel powder mixture, however, the results of previous studies on dimensional change are inconclusive. Majima and Sohama[148], for instance have investigated

the sintering of uniaxially pressed equiatomic Ti-Ni compacts and observed anisotropy of dimensional change with expansion in the radial dimension and contraction in the axial direction of a cylindrical compact. They attributed the contracting phenomenon to the appearance of thick layers of intermetallic compound in the press direction and the expanding effect to the reaction between the eutectic liquid present and the intermetallic compounds. Aksenov et al[149] on the other hand, observed a decrease in density of compacts during both solid and liquid phase sintering, suggesting that the appearance of a eutectic liquid during sintering is not the only cause of compact growth as proposed by Majima and Sohama. As the manufacture of components to close tolerances is one of the main objectives of the P/M technique, it is essential that the factors influencing the dimensional changes and the mechanisms involved are established. It is necessary to understand this in order to predict the magnitude of growth or shrinkage at every processing stage (e.g. during the design of a pressing die).

In this chapter, the results of a more detailed study of the effect of critical experimental variables on this phenomenon are reported. On the basis of the results, a mechanism has been proposed to account for the dimensional changes observed. The mean values of density and dimensional change reported here for each test condition were obtained from three independent specimens. Scatter between the values obtained for individual specimens was minimal.

7.2 Results

7.2.1 Powder Characteristics

The discrete nature of the titanium and nickel powder particles is revealed by the scanning electron micrographs shown in Figure 7.1. The fine nickel powder (Figure 7.1a) exhibits a fairly uniform size (3-7 μm) and shape with rough surface projections. The titanium powder particles are of irregular shape with a wide variation in size (Figure 7.1b). A typical sieve analysis for a 100 grams sample of the titanium powder is given in Table 7.1. It contains a relatively large proportion of coarse particles with 70.7% of the mass greater than 63 microns in diameter

Table 7.1. Particle size distribution of titanium powder.

Particle size, μm	% retained
150	0
125	1.8
106	11.6
90	17.9
75	17.5
63	21.9
38	16.1
less than 38	13.2

7.2.2 Densification

The effect of compaction pressure on green density for both uniaxial and cold isostatic compaction is shown in Figure 7.2. The salient features are:

(i) The green density increases with compaction pressure, and in the case of die pressing the rate of change becomes less with increasing pressure.

(ii) Over a comparable range of pressure, higher green densities are achieved by isostatic pressing compared with uniaxial die compaction.

Figure 7.3 shows a plot of $\ln(1/1-D)$ versus compaction pressure for uniaxial die compaction and cold isostatic pressing. A linear relationship between $\ln(1/1-D)$ and pressure exists for compacts made by isostatic pressing in accordance with equation 4.1 (Chapter 4). The data for die pressed samples indicate a similar trend except that the slope of the line (0.0014) is not as steep as for cold isostatic compaction (0.0017). Also, at high pressures above 630 MPa, a deviation from a straight line is observed for die compaction.

The green density curves are replotted in Figure 7.4 for comparison with sintered densities of compacts after sintering for 5 hours at 1000°C. It is apparent that the sintered densities are in most cases lower than the green densities, the only exception being

the die compacted samples at low pressures (e.g. the density of compact pressed at 155 MPa increases from 58 to 62% of theoretical density).

The effect of sintering temperature on the density of uniaxially pressed specimens at a pressure of 774.4 MPa (81% of theoretical density) and isostatically pressed compacts at 503 MPa (82% of theoretical value) is presented in Figure 7.5. In both cases there is a gradual fall in density with increasing temperature up to 900°C and this becomes dramatic as the temperature is raised to 1000°C. For example, the density of uniaxially compacted specimen decreases from 79% of theoretical value at 900°C to 68% at 1000°C.

In addition to compaction pressure and sintering temperature, there are several other parameters (e.g. sintering time) which can affect the sintered density of a compact, but in the present study, only the influence of powder particle size was examined. Other variables were kept constant. Mixtures were prepared from titanium powder of various particle sizes and a nickel powder of a mean particle diameter of about 5 μm. Compacts were uniaxially pressed at 744.4 MPa and sintered at 1000°C for 5 hours. The results are plotted in Figure 7.6. It can be seen that the density increased from 61 to 80% of theoretical value by reducing the average particle size of titanium from 137.5 to 27 μm.

7.2.3 Dimensional Changes in Sintered Compacts

Dimensional changes were determined on cylindrical compacts as the difference in height (axial) and diameter (radial) between the green and sintered samples. The values were expressed as percentages of the green compact dimensions. The results are plotted in Figure 7.7, 7.8 and 7.9 illustrating the variations of dimensional change with compaction pressure, sintering temperature and titanium particle size respectively. Growth of compacts is indicated by a plus sign (+) while shrinkage is shown by a minus sign (-). The following observations can be made from these figures;

(i) At all compaction pressures, the radial dimension of uniaxially pressed specimens grows while the axial dimension shrinks. The magnitude of radial growth increases with compaction pressures whereas the amount of shrinkage becomes less with increasing pressure (Figure 7.7a).

(ii) Cold isostatically pressed compacts expand in both radial and axial dimensions during sintering at 1000°C and the amount of expansion, which rises with compaction pressure is slightly higher in the radial than the axial direction (Figure 7.7b).

(iii) The radial swelling of uniaxially die pressed specimens rises progressively with temperature up to 900°C but increases sharply when the sintering temperature is raised to 1000°C. The

contraction in the axial dimension follows a similar pattern up to 900°C but its magnitude decreases from 5% at 900°C to 0.8% at 1000°C (Figure 7.8).

(iv) The dimensional change behaviour of isostatically compacted specimens indicates the same trend as die compacted samples pressed to the same density (81% of theoretical value). However, the amount of growth and shrinkage are significantly smaller (Figure 7.8). When the sintering temperature is raised to 1000°C, isostatic compacted specimens expand in both the radial and axial dimensions.

(v) The radial growth of uniaxially pressed compacts decreases while the axial shrinkage increases with reducing particle size. The radial swelling changes at a greater rate than the axial shrinkage (Figure 7.9). Compacts containing titanium powder with particle sizes larger than 100 μm expand in both the radial and axial dimensions.

7.2.4 Microstructures

Scanning electron micrographs representative of the green compacts of similar density (≈ 81%) produced by the two compaction techniques are shown in Figure 7.10. The cylindrical shape samples were sectioned along a diameter and prepared for metallographic examination as described in Section 6.8 (Chapter 6). Observations were made in the direction A-A as indicated in Figure 7.10c. The

microstructures (Figure 7.10) show quite clearly the large discrepancy in particle sizes between the nickel (white) and titanium (dark) powders. The structures are interesting for the form of powder particle distribution within the two compacts. In the uniaxially pressed sample (Figure 7.10a) considerable segregation of the distinct powder particles has taken place in the axial direction, whereas in the isostatically compacted specimens (Figure 7.10b) the titanium and nickel particles are more evenly distributed.

Figure 7.11 is a sequence of micrographs showing the effect of sintering temperature on uniaxially compacted samples at 774.4 MPa (81-82% of theoretical density). After sintering at 600°C for 5 hours there is minimal alloying and most of the interparticle boundaries are still discernible (Figure 7.11 a). As the temperature is increased, interparticle intermetallic phases are formed (Figure 7.11 b-e). The amount of porosity also increases with rising temperature. Another important feature is the difference in the distribution and morphology of pores in samples sintered at temperatures up to 900°C (Figure 7.11 a-d) compared with that sintered at 1000°C (Figure 7.11e). Up to 900°C, the structure is characterised by pores in the form of a network, the distribution of which follows the initial sites of nickel particles in the compact. By contrast, the structure of sample sintered at 1000°C is marked by relatively large pores which appear to be more isolated from each other, and their position cannot be correlated with the initial distribution of nickel particles.

The micrographs of samples prepared from Ti-50 at-% Ni powder

mixtures, containing various titanium particle sizes and sintered at 1000°C, illustrate that the porosity is related to the size of titanium particles (Figure 7.12). A plot of pore size versus titanium particle size displays a linear relationship (Figure 7.13).

7.2.5 Diffusion Couple

The increase in the degree of alloying and the associated rise in the amount of pores as the sintering temperature is raised from 600 to 900°C are indicative of heterogeneous diffusion in the solid state. In effect, the compact can be considered as a collection of several small diffusion couples where the difference in interdiffusion rates results in the creation of diffusional porosities in the region of the faster diffusing element. The microstructural evidence (Figure 7.11b-d) appears to suggest that nickel diffuses more rapidly than titanium in this system. To verify this view, a diffusion couple experiment was undertaken as previously described in Chapter 6.9. The results of this investigation are given in Figure 7.14. The scanning electron micrograph of the diffusion couple (Figure 7.14a) demonstrates the presence of porosity in the nickel-rich region of the diffusion zone. This result is consistent with that of sintered compacts (Figure 7.11a-d) in which the distribution of pores follows the initial sites of nickel particles in the green compact. The creation of these diffusional porosities indicates that nickel atoms diffuse faster than titanium. The concentration profile determined by energy dispersive X-ray quantitative analysis along the micromarker lines on the micrograph in Figure 7.14a is given in Figure 7.14b. The

intermetallic phases identified are in accordance with the titanium-nickel equilibrium diagram (Figure 3.1), although only a minute trace of Ti_2Ni is present.

7.2.6 Hot Isostatic Pressing (HIP) of Sintered Compacts

In most cases, sintering of compacts made from elemental titanium-nickel mixtures resulted in a decrease in density. It was therefore decided to study the effect of further HIP processing on the density of sintered specimen. Some sintered compacts were HIPed for 3 hours at 950°C using a pressure of 103 MPa. This raises their densities to near full density (99% +) regardless of the initial sintered density. Hot isostatic pressing results in a substantial decrease in the level of porosity (Figure 7.15). The structure of the HIPed sample contains a significant volume fraction of oxides. This is attributable to oxygen pick-up during the HIPing process

7.3 Discussion of Results

7.3.1 Powder Compaction

The compaction behaviour of metal powders has been well documented (e.g. Refs. 69,70, Chapter 4) and can be divided into three overlapping stages:

(i) Particle movement and rearrangement at low pressures. The degree to which this occurs would largely depend on several

factors such as particle size distribution and particle shape. For instance, fine powder particles with poor flow properties are likely to form bridges.

(ii) Plastic deformation of particles. The extent of plastic deformation which occurs would depend on the properties of the metal powder. Deformation would be more extensive during the compaction of soft ductile powder than in the case of hard brittle particles.

(iii) Mechanical interlocking and cold welding.

In uniaxial die pressing, the pressure is applied to the powder in the vertical direction between two opposing punches as shown in Figure 4.1 (Chapter 4). Frictional forces between the powder particles and the die wall inhibit the transmission of uniform pressure throughout the compact. Consequently, a variation in density occurs within the compact[150]. Also, as punch load increases, further densification is increasingly hindered by work hardening of particles and by friction. In isostatic pressing, the absence of die wall friction and the uniform application of pressure in all directions results in a more even density profile in the specimen[151]. In addition, the enhanced particle movement and rearrangement results in superior compressibility. This difference is confirmed in the present study (Figure 7.2). A further result of these differences in stage (i) compaction between the two techniques leads to a significantly greater degree of segregation of titanium and nickel particles in the die pressed compacts as can be seen in Figure 7.10.

It is also found that the large size variation and differences in mechanical properties between nickel and titanium powders do not result in any deviation from conventional compaction behaviour. A plot of ℓn(1/1-D) versus compaction pressure yields a straight line, with that of isostatic compaction producing a higher gradient (Figure 7.3). In the case of a uniaxial pressing a deviation from a linear relationship occurs at higher pressures (> 630 MPa) probably due to work hardening and friction effects as mentioned above. These results are in agreement with the work of Hewitt et al[70] and Morgan and Sands[68] (Chapter 4).

7.3.2 Sintering

During the sintering of compacts made from different elemental powders, both self- and heterogeneous diffusion will take place, assuming that alloy formation can occur. Diffusion between nickel and titanium powder will initially result in compositional variations in the compact. Eventually, a homogeneous structure is found with a density significantly less than that predicted by theory. The theoretical density of the final compact (100% dense) for Ti-50 at-% Ni is 6.44 Mg m^{-3}. The presence of diffusional (Kirkendall) porosities in nickel particle regions within the sintered compacts (Figure 7.11) and on the nickel side of the diffusion couple (Figure 7.14) show that nickel diffuses faster than titanium in the present case.

It is interesting to note the difference in distribution and morphology of pores in the compacts sintered at temperatures up to

900°C (Figure 7.11 a-d) compared with those sintered at 1000°C (Figure 7.11e). At low temperatures ($\leq$ 900°C) pores in the compact are in the form of network and are concentrated in the prior nickel particle regions which is consistent with the solid state diffusion mechanism. However, at 1000°C the pore size increases significantly and the pores appear to be more isolated from each other. The later structure is accompanied by a drop in density (Figure 7.5). According to the Ti-Ni phase diagram there is the possibility of a transient liquid phase formation of a eutectic composition 24.5 at -% Ni at 955°C. The reason for the change in pore morphology can be attributed to the presence of this liquid phase.

7.3.3 Dimensional Changes

The anisotropy of dimensional change observed in this study is in agreement with the report by Majima and Sohama[148]. In their case, Ti-Ni powders were uniaxially pressed and sintered above the eutectic temperature only. They ascribed the axial contraction to the formation of thick plates of intermetallics during sintering and the radial expansion to a reaction between the transient liquid phase and these intermetallic plates. The work here (Figure 7.8) demonstrates that this difference in radial and axial behaviour is present for all sintering temperature and therefore a mechanism based on the presence of liquid phase alone is not correct. In this chapter, I suggest a different mechanism to account for the dimensional behaviour during solid and liquid phase sintering. Majima and Sohama used similar powders to those in the present research and I believe that the

reasons for the radial/axial dimensional changes are connected with the large discrepancies in powder diameters which result in significant powder segregation during uniaxial pressing (Figure 7.10). A model is proposed that accounts for the observed phenomenon for temperatures both below and above the eutectic temperature. I will now consider each case in turn.

7.3.3.1 Dimensional Change During Sintering Below the Eutectic Temperature

A schematic diagram of the model is shown in Figure 7.16 starting with a representation of the segregated powder structure (Figure 7.16a). When sintering is performed below the eutectic temperature, non-uniform diffusion will take place. In the radial direction interdiffusion between titanium and nickel will predominantly occur (Figure 7.16b), whereas in the axial direction diffusion will be principally between particles of the same powder type (i.e. Ni-Ni and Ti-Ti). Since nickel diffuses faster than titanium, the small nickel particles experience a net loss of atoms and diffusional porosities are created at the prior nickel sites, resulting in the formation of a skeleton pore network in the sintered structure (Figure 7.16c). It is necessary to compare this model with that in Figure 7.11a-d. The overall positive flux of atoms into the titanium particles will result in uniform expansion in all directions (Figure 7.16b). Concurrently, there will be Ti-Ti self diffusion between touching Ti particles in the axial direction which will cause neck growth and subsequent densification. This will in turn lead to

contraction in the axial direction (Figure 7.16c). The latter of these two mechanisms must predominate in this case since the actual observations show contraction. The former mechanism clearly accounts for the reported expansion in the radial direction (Figure 7.8).

Further evidence in support of the segregation effect on dimensional behaviour is also provided by the fact that isostatically pressed compacts show only slight growth and shrinkage in the radial and axial dimensions respectively when sintered in the solid state (Figure 7.8). For example, at 900°C the respective radial and axial dimensional changes for isostatically pressed specimens are +0.63% and -0.39%, while the corresponding values for uniaxial compaction are +3.23% and -5.0%. The minimal particle segregation in isostatic compaction is attributable to powder handling during the packing process (filling and tapping the PVC mould while in vertical position to ensure a compact of fairly uniform section). It is therefore postulated that the dimensional behaviour observed in this work during sintering below the eutectic temperature is a combination of interdiffusion effects and segregation of powder particles.

7.3.3.2 Dimensional Change During Sintering Above the Eutectic Temperature

As discussed in Chapter 4.4.3, the dominant mechanism for densification in liquid phase sintering is particle rearrangement. This mechanism implies particle mobility during densification. We would therefore expect that any factors which inhibit particle

mobility will hinder any beneficial effect of liquid phase sintering. Unlike the well investigated simple systems such as the tungsten-copper alloys[94] where the liquid phase is formed at the melting point of Cu, followed by possible particle rearrangement, the liquid phase in Ti-Ni systems which forms at 955°C is of the eutectic composition (Ti-24.5 at -% Ni). Thus solid state diffusion is a prerequisite to the formation of the transient liquid phase. Under this condition, therefore, we should anticipate that the dimensional behaviour resulting from interdiffusion and particle segregation effects, as discussed for solid state sintering below the eutectic temperature, would precede the formation of liquid. As solid state diffusion continues, the transient liquid phase, which would eventually appear on the titanium side of the initial titanium-nickel interparticle contact could penetrate along capillaries including those formed during the preceding solid state diffusion stage. This would cause expansion of the compact, leaving pores behind in the prior titanium particle region, which would account for the final structure seen in Figure 7.11e. A schematic diagram illustrating this process is shown in Figure 7.17.

The overall dimensional change is therefore related to two phenomena:

(i) Initial solid state diffusion (interdiffusion and particle segregation effects).

(ii) The expansion effect resulting from the penetration of liquid into capillaries.

The expansion as a result of (ii) will be superimposed on the radial expansion connected with (i) whereas in the axial direction it will counteract the contraction due to (i). This accounts for the sharp increase in radial growth and a rapid decrease in axial shrinkage as the sintering temperature is raised above the eutectic value (Figure 7.8). This can also explain the reason for the change from pores in the form of a network to large and more isolated pores when the compact is sintered below and above the eutectic temperature (Figure 7.11a-e) and the associated drop in density (Figure 7.5).

The pore size of compacts sintered above the eutectic is related to the particle size of titanium (see Figures 7.12, 7.13) since titanium contributes 75.5 at -% of the liquid phase. Fine powder particles are generally characterised by high shrinkages during sintering, but the fact that the radial growth decreases at a higher rate than the rate of increase in axial shrinkage with reducing titanium particle size (Figure 7.9) provides further evidence in support of the suggested correlation between particle segregation and dimensional change. We would expect that, as the difference between the two particle sizes decreases, the tendency to segregate would become less and therefore the anisotropy of the dimensional change would become smaller.

From the analysis of the results presented in this chapter it is proposed that the dimensional behaviour observed above the eutectic temperature is a combination of three effects:

(i) Kirkendal diffusion effects

(ii) Particle segregation

(iii) Expansion resulting from the penetration of molten liquid into capillaries.

Although the above model has been greatly simplified by assuming that the powder particles are of spherical shape, it clearly illustrates the significant effect of particle sizes and powder segregation on the dimensional changes of compacts during sintering.

The phenomenon of powder particle segregation is well known in powder metallurgy processing of ferrous materials (e.g. Refs. 152-154). For instance in Fe-Cu alloys, one grave problem associated with copper additions is the pronounced growth of compacts during sintering. Thus, any variations in copper distribution results in dimensional instability. It has been found that by using a partially prealloyed iron copper powder instead of an elemental mixture, a significant improvement in dimensional tolerances of sintered compacts can be obtained[153]. This effect has been explained in terms of the reduced segregation of copper. Partially prealloyed iron powders consist of iron particles onto which finer particles of the metallic alloying elements are diffusion-bonded.

The growth of Fe-Cu compacts has often been attributed to the diffusion of copper into iron particles, leaving initial copper particle sites as large stable isolated pores[155]. However, it has recently been demonstrated that the penetration of the molten copper

into the iron interparticle spaces and some of the grain boundaries in the particles make a significant contribution to the swelling observed in the Fe-Cu system[146,156]. The results of a model experiment[64] on Fe-10Cu has shown that 65% of the 6% volume increase arises from the penetration of copper into the interstices in the compact and into the grain boundaries while 35% is due to diffusion of copper into iron particles. In the present study (Figure 7.5) a 2% decrease in density is observed during solid state sintering at 900°C whereas at 1000°C in the presence of liquid phase the corresponding value is 13%. Thus, the model proposed here (Figure 7.16 and 7.17) would also suggest that the penetration of liquid metal into capillaries is the dominant mechanism for compact growth in Ti-Ni system.

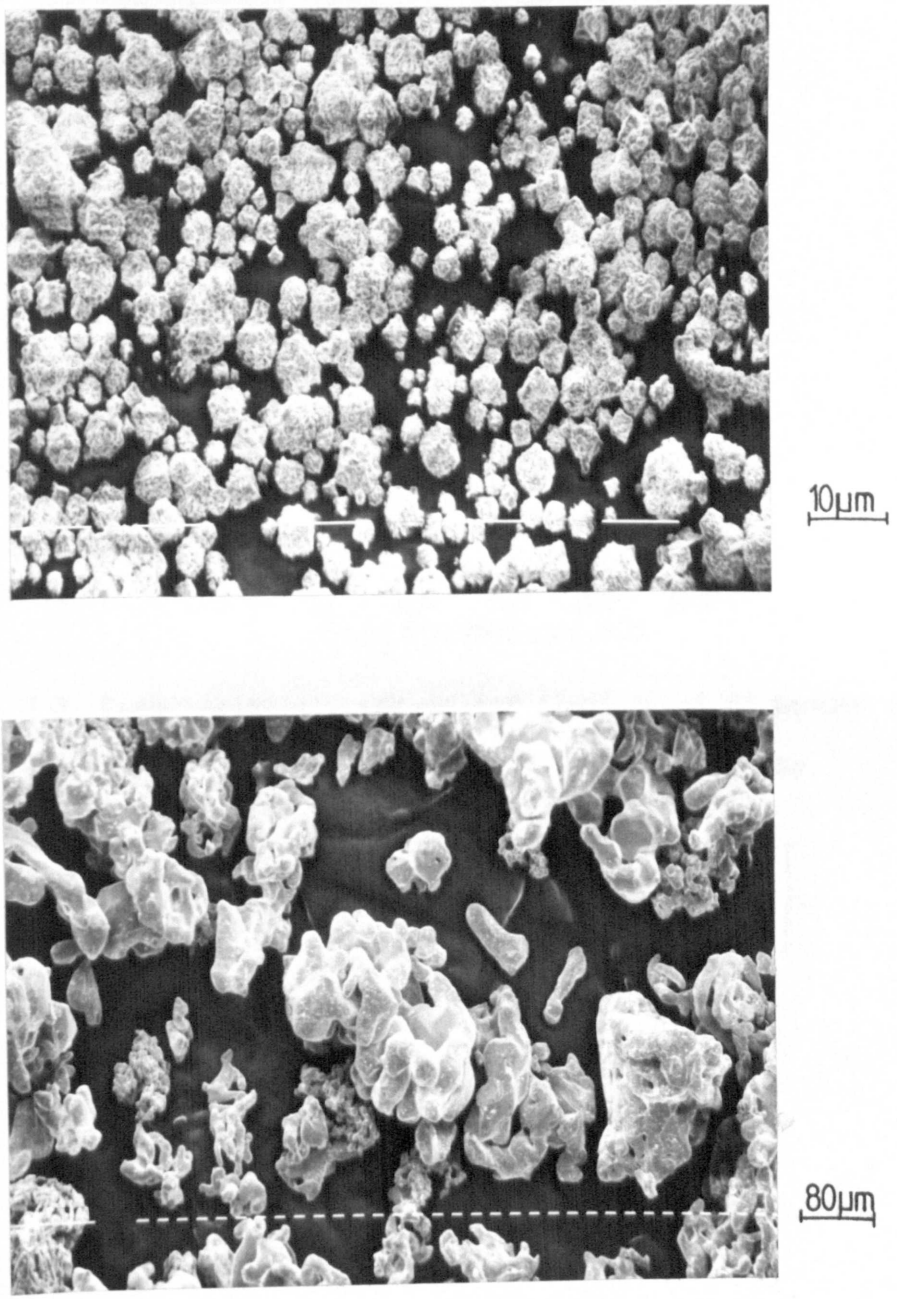

Figure 7.1 Scanning electron micrographs of (a) nickel and (b) titanium powders.

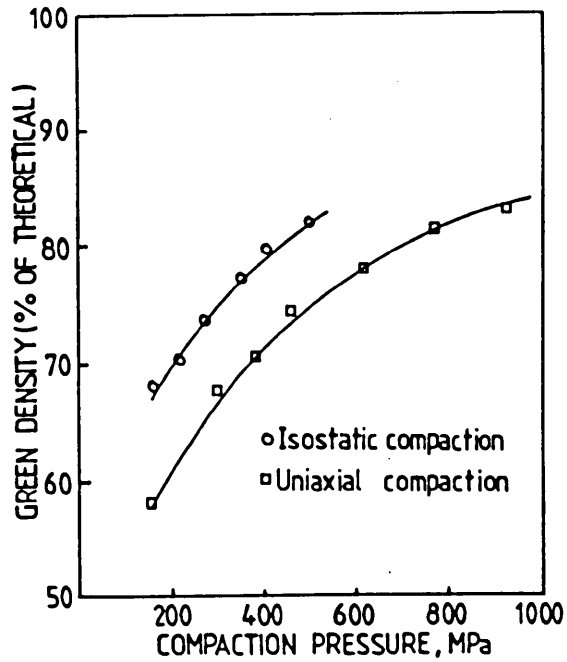

Figure 7.2 Compressibility curves for Ti-50 at -% Ni powder mixture processed by uniaxial and isostatic pressing.

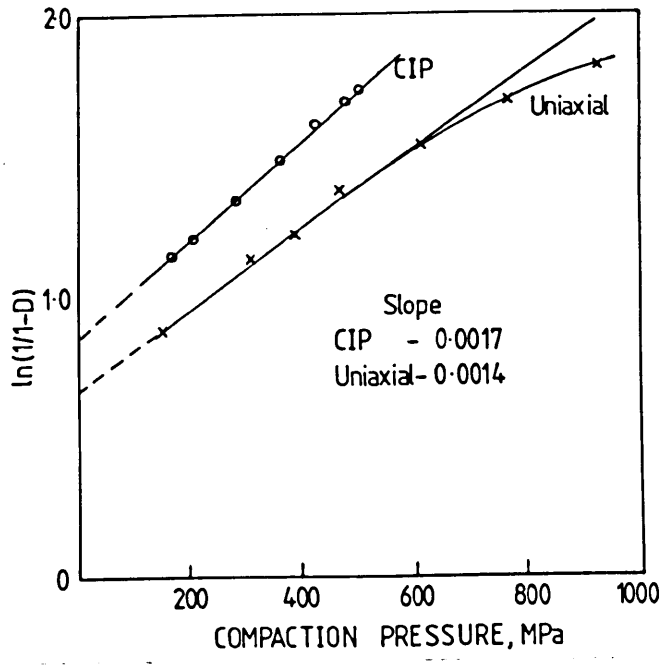

Figure 7.3 Plots of Ln(1/1-D) vs compaction pressure for uniaxial die compaction and cold isostatic pressing.

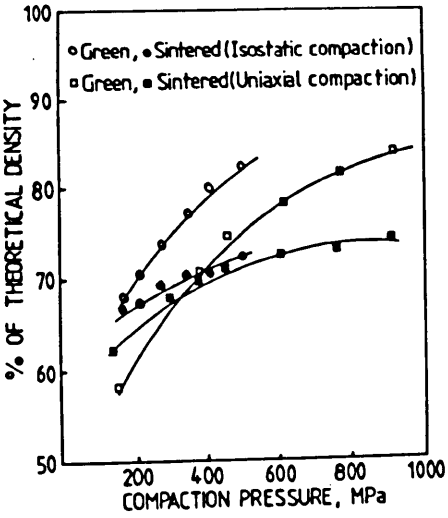

Figure 7.4 Comparison of green and sintered density curves (specimens sintered for 5 hrs at 1000°C).

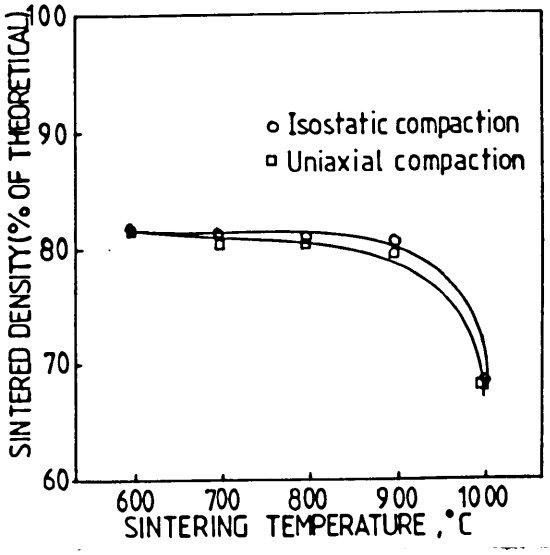

Figure 7.5 Influence of sintering temperature on density of compacts pressed at 503 MPa (isostatic) and 774.4 MPa(uniaxial die) and sintered for 5 hours.

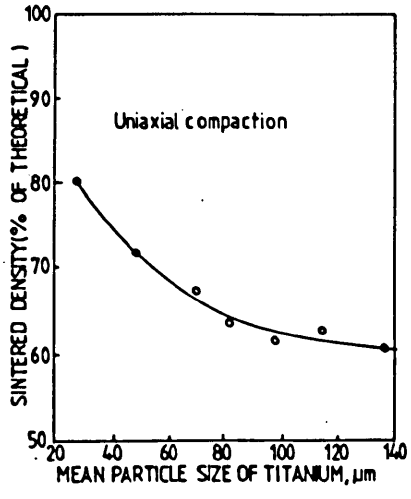

Figure 7.6 Effect of titanium particle size on sintered density of compacts pressed at 774.4 MPa and sintered at 1000°C for 5 hours.

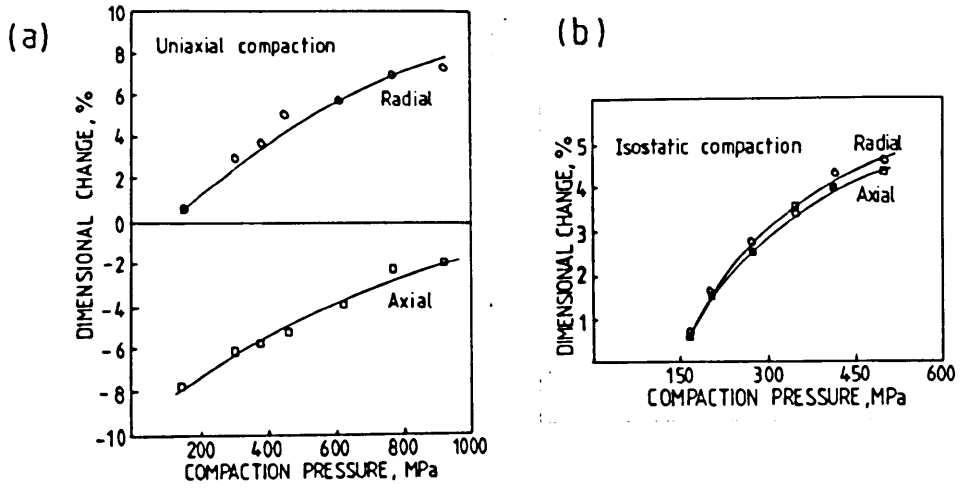

Figure 7.7 Variation of dimensional change with compaction pressure (a) uniaxial compaction (b) isostatic compaction.

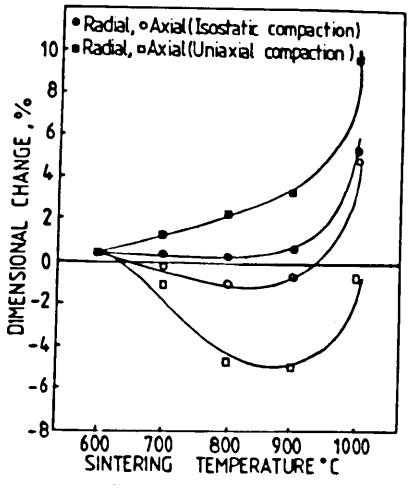

Figure 7.8 Effect of sintering temperature on dimensional change for uniaxially pressed specimens (774.4 MPa) and isostatically compacted samples (503 MPa) sintered for 5 hours.

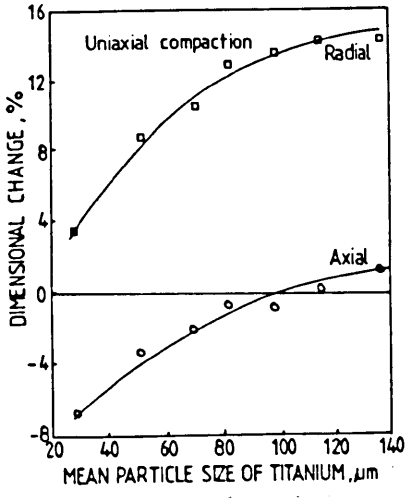

Figure 7.9 Variation of dimensional change with titanium particle size for uniaxially processed compacts (774.4 MPa) and sintered at 1000°C for 5 hours.

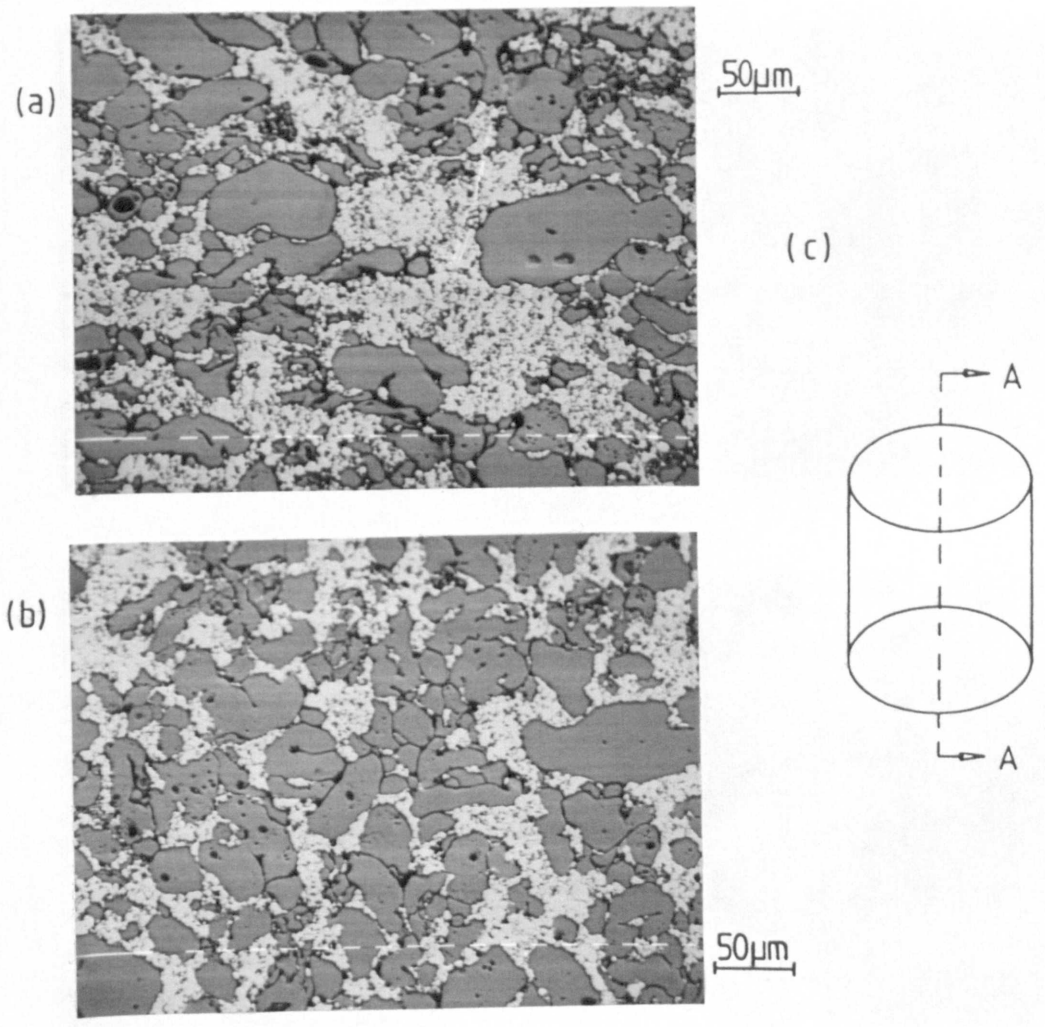

Figure 7.10 Microstructures of (a) uniaxially pressed green compact showing extensive segregation of powder particles and (b) isostatically compacted specimen showing almost uniform distribution of powder particles. (c) Cross-section of metallographic observations.

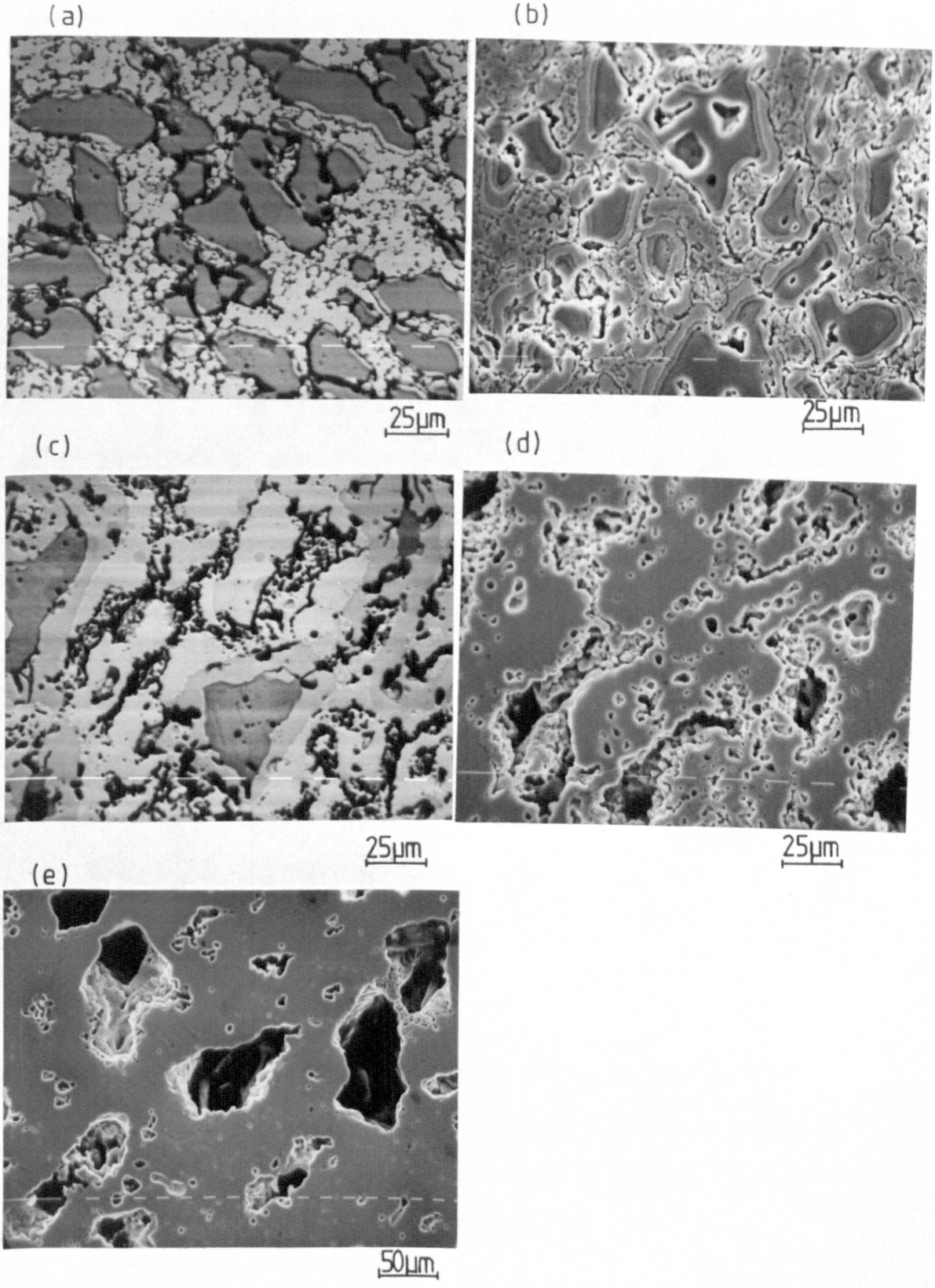

Figure 7.11 Scanning electron micrographs of compacts sintered for 5 hours at (a) 600°C, (b) 700°C, (c) 800°C, (d) 900°C, and (e) 1000°C, illustrating the effect of sintering below ($\leq$ 900°C) and above (1000°C) the eutectic temperature on the morphology and distribution of pores.

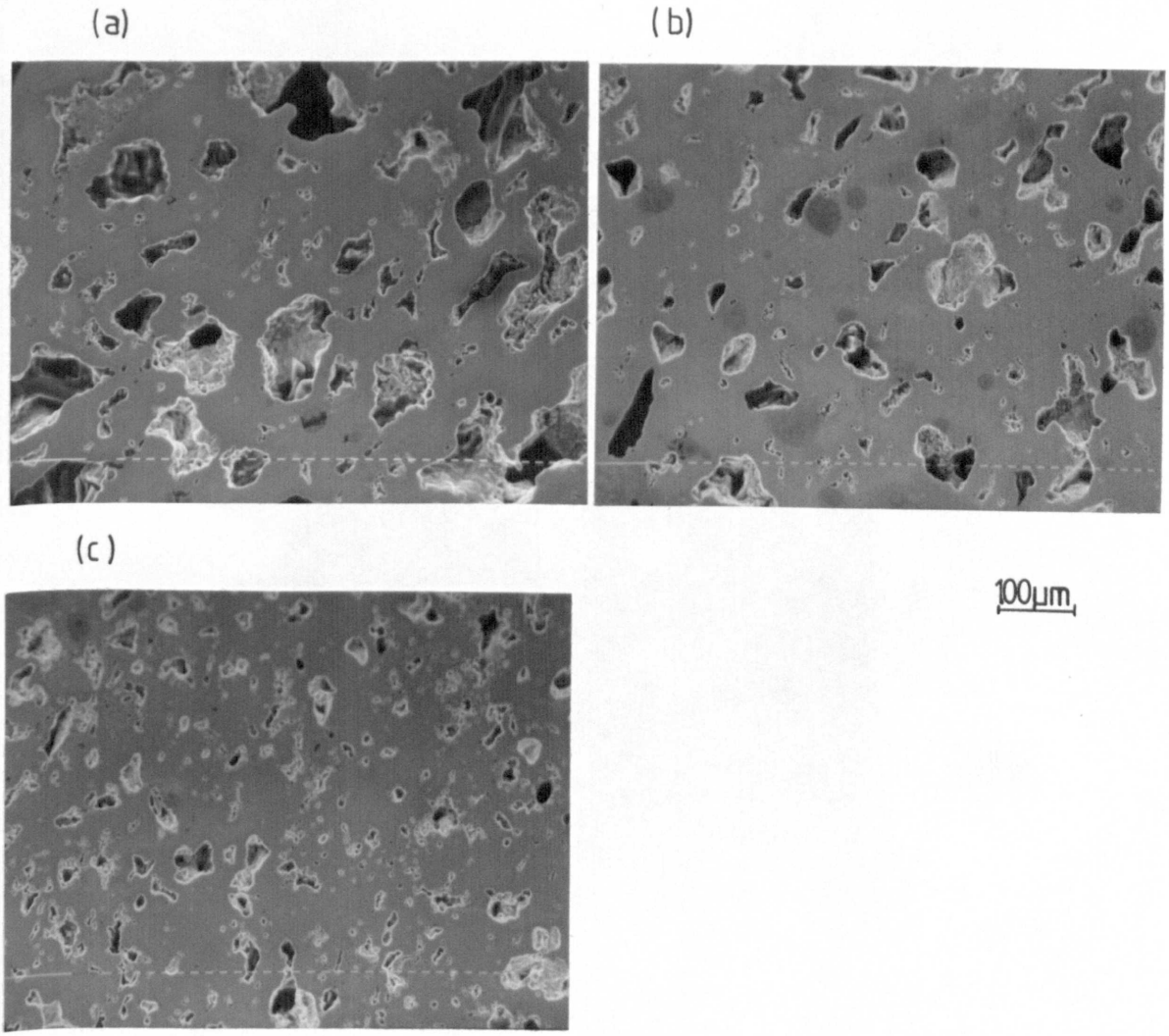

Figure 7.12 Scanning electron micrographs of samples pressed at 774.4 MPa and sintered for 5 hours at 1000°C, showing the effect of titanium particle size on porosity. Mean particle size include (a) 82.5 µm, (b) 50 µm, and (c) 27.5 µm.

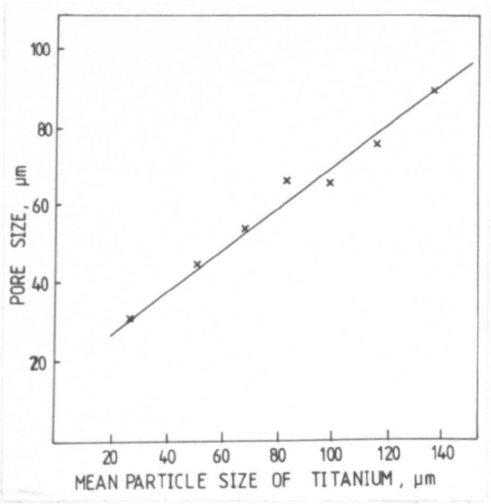

Figure 7.13 Variation of pore size with titanium particle size in compacts pressed at 774.4 MPa and sintered at 1000°C for 5 hours.

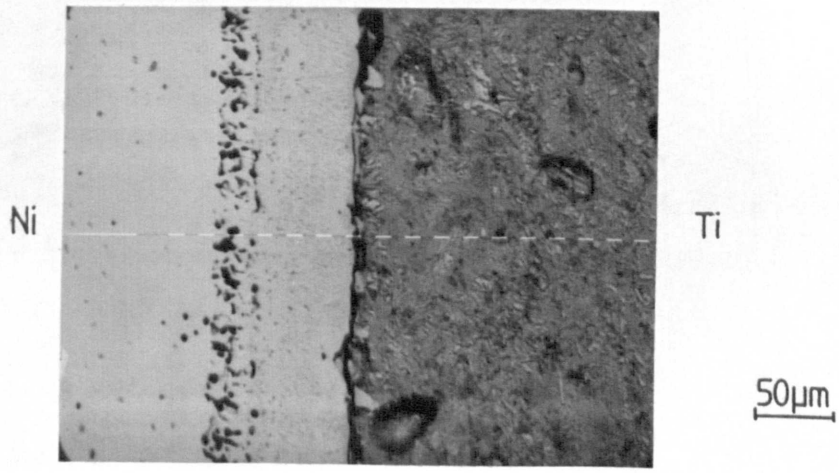

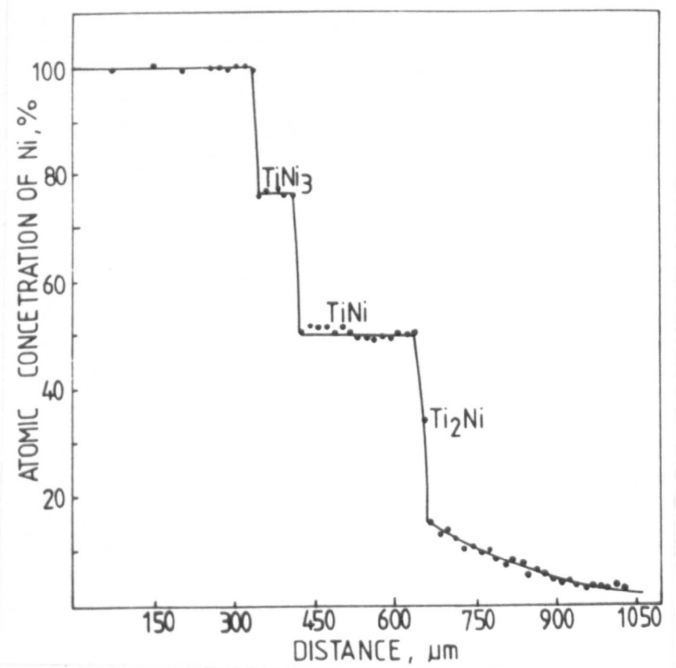

Figure 7.14 (a) Microstructure of Ti-Ni diffusion couple, annealed at 900°C for 72 hours, illustrating the presence of diffusional porosities in nickel rich region of the diffusion zone;

(b) Concentration profile for Ni across the diffusion zone.

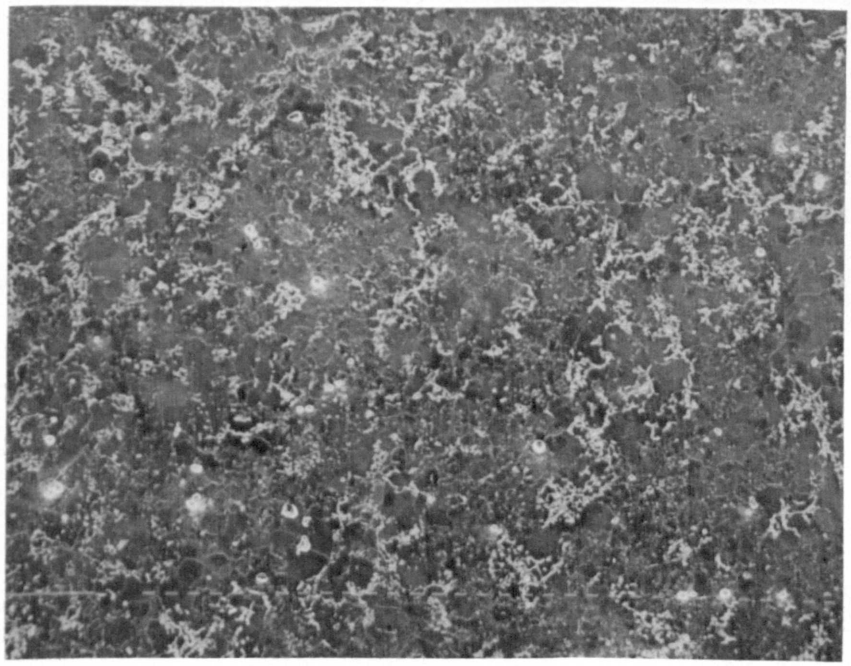

Figure 7.15 Scanning electron micrograph of HIPed compact.

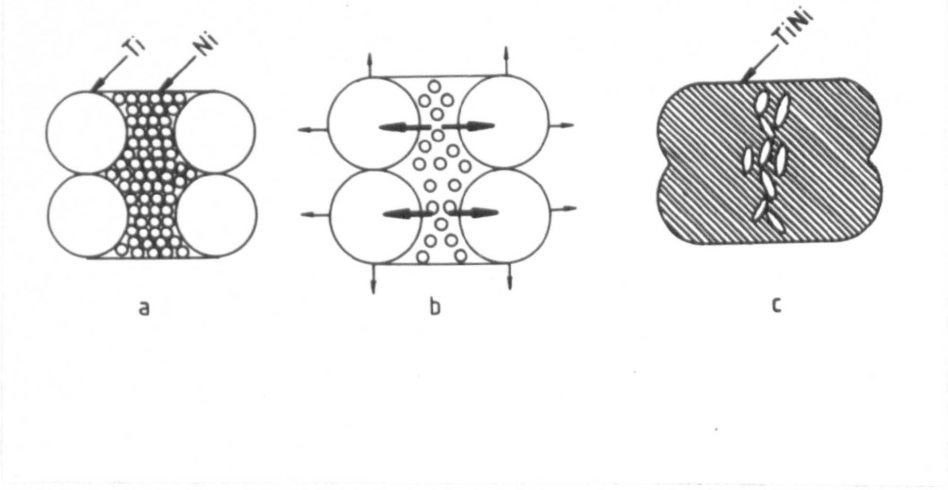

Figure 7.16 A proposed model for describing the mechanism of dimensional changes during sintering below eutectic temperature.

(a) Schematic representation of segregated powder particles in uniaxially pressed compact;

(b) Expansion of compact due to diffusion of nickel atoms into titanium particles, and creation of diffusional porosities in prior nickel region (large arrows indicate direction of net flux of atoms and small arrows for expansion);

(c) Final structure illustrating the presence of skeleton pore network at prior nickel sites giving rise to radial expansion and densification in axial direction as a result of growth of necks between touching titanium particles

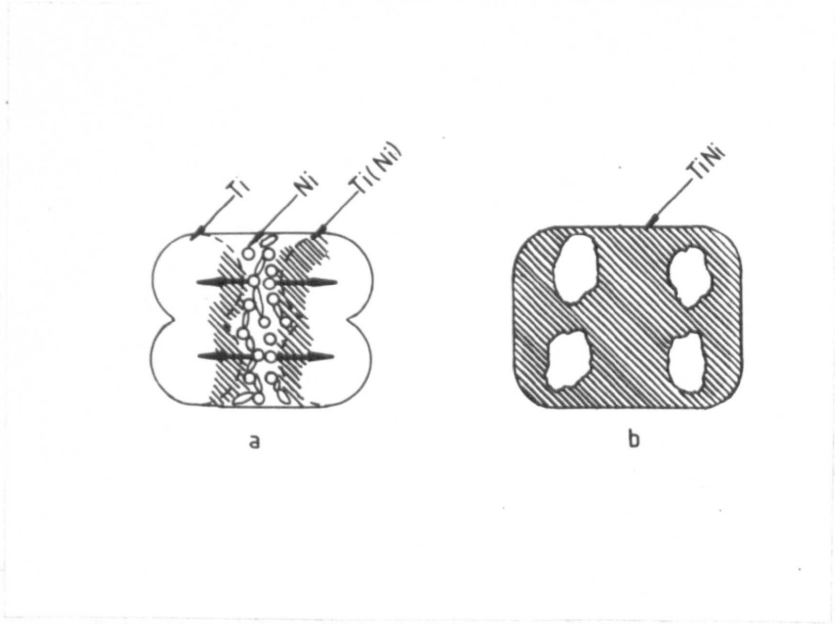

Figure 7.17 Schematic diagram of the sintering mechanism above the eutectic temperature

(a) Net nickel diffusion into titanium particles as in Figure 7.16 leaving diffusional porosity.

(b) After the formation of a transient liquid phase, penetration of liquid into capillaries occurs, causing overall expansion of compact, leaving pores behind on prior sites of titanium particles.

CHAPTER 8

PROPERTIES OF SINTERED TiNi COMPACTS

8.1 Introduction

In Chapter 7, the results of an investigation involving the compaction and sintering of Ti-Ni elemental powders was reported. In that instance the densities of compacts decreased during sintering. This phenomenon has been related to the difference in interdiffusion rates of titanium and nickel and the occurrence of a transient liquid phase at temperatures above the eutectic temperature. In this chapter the results of a study into the properties of sintered compacts are presented. The properties investigated are hardness, martensitic transformation characteristics and the shape memory behaviour. Unless otherwise stated, the alloy studied was the equiatomic concentration.

8.2 Hardness Determination

Vickers hardness (macro) values were obtained from sectioned and polished samples using a 10 kg load. The average of 10 readings was recorded for each specimen and every mean value given here was obtained from three specimens. The actual value of individual measurements varied within ± 5 HV of the mean.

The hardness results on isostatically pressed compacts at a pressure of 503 MPa (82% of theoretical density) and uniaxially compacted samples at 774.4 MPa (81% of theoretical density) sintered at different temperatures are plotted in Figure 8.1. It is apparent that there is no simple correlation between hardness and sintering temperature. For instance, the hardness of an isostatically pressed sample increases from 80 HV at 600°C to 130 HV at 800°C and then decreases to 83 HV at 1000°C. The hardness curve for uniaxially processed samples shows the same trend.

The dependence of hardness on titanium particle size (at constant nickel particle diameter) for uniaxially pressed specimens at a pressure of 774.4 MPa and sintered at 1000°C for 5 hours is reported in Figure 8.2. It indicates that the smaller the particle size the higher the hardness value. As the titanium particle size is reduced from 137.5 μm to 27.5 μm, the hardness increases from 60 to 128 HV.

8.3 Effect of Composition and Heat Treatment on the Hardness of Ti-Ni Alloys

Margolin et al[39] (Chapter 3.2) have proposed a phase diagram (Figure 3.1b) showing the TiNi phase region extending from 49 to 54 at -% Ni at temperatures below 1000°C. However, in an investigation into the properties of various Ti-Ni alloys with compositions close to equiatomic, Buehler and Wang[36] found that the alloys containing 52 to 57 at -% Ni can be hardened by quenching from around 950°C, while the hardness of an equiatomic specimen is relatively unaffected by

cooling rate. This observation suggests a constitutional difference between the equiatomic TiNi compound and those of nickel-rich composition (e.g. Ti - 52 at -% Ni) which is in contrast to the data of Margolin et al. It was therefore decided to investigate in more detail the response of a number of TiNi alloys, around the equiatomic concentration, to heat treatment.

Titanium-nickel powder mixtures containing varying amount of nickel from 49 to 55 atomic per cent were prepared by mixing elemental powders. Cylindrical samples were pressed in a cold isostatic press using a pressure of 503 MPa. Sintering was performed in vacuum furnace at 1000°C for 5 hours. Samples were then encapsulated under a vacuum pressure of 10^{-3} MPa and either furnace cooled or water quenched after a 1/2 hour treatment at 1000°C. Microhardness measurements were performed with a load of 100 g. Metallographic observations were conducted on the same samples which were used for microhardness determination.

The results obtained are shown in Figure 8.3. It is apparent from Figure 8.3 that samples containing less than 51 at -% Ni do not display any quench hardening effect. By comparison with this observation, specimens with higher nickel content show a considerable increase in hardness when tested in the quenched condition. The maximum hardness value of 690 HV occurs at about 54 at -% Ni. These results are in agreement with those of Buehler and Wang which show that hardening effect begins at 51 at -% Ni and an enlarged hardness peak occurs over a composition range from 53 and 57 at -% Ni.

The microstructures of some of the samples investigated are presented in Figure 8.4. The Ti-50 at -% Ni is virtually a single phase in both the as-quenched and furnace cooled condition (Figure 8.4a and b). In the case of nickel-rich alloys (e.g. Ti-54 at -% Ni), however, a single phase only is observed in the as-quenched condition (Figure 8.4d). When the sample is allowed to cool slowly in the furnace, a second phase precipitates along the grain boundaries and within the grains, producing a Widmanstatten type of structure (Figure 8.4c). The results of X-ray image analysis (Figure 8.5) show that the second phase precipitates are nickel-rich. By means of a quantitative energy dispersive X-ray analysis, the second phase was found to be $TiNi_3$. A further difference between the furnace cooled and the water quenched Ni-rich specimens is that there are no martensite plates in the structure of the quenched samples (Figure 8.6b). This indicates that the transformation temperature, is below room temperature. This observation is consistent with the differential scanning calorimetry result to be presented in the next section.

8.4 Transformation Characteristics

The shape memory effect has been associated with a thermoelastic martensitic transformation (Chapter 2.4.2). This type of reaction is highly sensitive to a number of processing variables such as heat treatment conditions and thermal cycling. In the present investigation, the effects of composition, heat treatment and complete thermal cycling on the transformation behaviour of Ti-Ni alloys were

examined. Complete thermal cycling involves cooling to transform the entire sample to martensite and then heating until a complete reversion to the high temperature parent phase is obtained. In this instance, the specimen was cycled between -100°c and +200°C. All transformation temperatures were monitored by a differential scanning calorimeter (DSC) as previously described in Chapter 6. Typical DSC heating and cooling curves for pressed and sintered Ti-50 at -% Ni specimen are given in Figure 8.7. Both the exothermic and endothermic peaks relating to the martensitic transformation on cooling and the reverse transition on heating are clearly defined. The characteristics temperature (M_s, M_f, A_s, and A_f) points on the curves are also shown.

The effect of composition on the transformation temperature, M_s of samples cooled in the furnace after heat treating at 1000°C for 1/2 hour is presented in Figure 8.8. The M_s decreases considerably from 79.2 to 33°C by raising the nickel content in the TiNi alloys from 50 to 52 at -%. Further rise in nickel concentration lowers the reaction temperature slightly. The M_s of water quenched Ti-49 at -% Ni and Ti-50 at -% Ni specimens are also shown in Figure 8.8. It can be seen that the M_s temperatures of these two alloys are not significantly affected by the rate of cooling. For the case of nickel-rich alloys, however, the water quenched samples did not transform even when cooled to -100°C. This means that the M_s of nickel-rich alloy is considerably suppressed by quenching.

The influence of thermal cycling on the transformation

temperatures, M_s and A_s of Ti-50 at -% Ni alloy is shown in Figure 8.9. M_s decreases from 79.2 to 70°C after 14 cycles and then remains relatively stable with further cycling. The A_s shows similar behaviour except that the point of stability is reached after about 20 cycles. As a result of the relative changes in the M_s and A_s, the transformation hysteresis also decreases slightly from 5.6 to 3.8°C after 20 cycles. A full summary of the characteristics transformation temperatures (M_s, M_f, M_{max}, A_s, A_f and A_{max}) is presented in Tables 8.1 and 8.2. M_{max} and A_{max} are the temperatures at the point of maximum heat flow on the DSC plot during the forward and the reverse transformation respectively. All the temperatures decrease as the number of cycles rises. The enthalpies of transformation are also shown in the tables. For the case of the martensitic reaction the enthalpy decreases from 3.61 to 3.23 kJ $mole^{-1}$ as a result of thirty cycles. A similar depression from 3.59 to 3.26 kJ $mole^{-1}$ is also observed for the reverse transformation.

8.5 Shape Memory Effect in Sintered Ti-Ni Compacts

It has been pointed out in Section 7.1 that the porosity in sintered compacts often influences their properties. An experimental study was therefore undertaken to ascertain whether the shape memory effect would display itself in a porous TiNi compact. The results in Chapter 7 indicate that the occurrence of a transient liquid phase is one of the main contributing factors to the decrease in density experienced by Ti-Ni powder compacts during sintering. In the present investigation, compacts were uniaxially pressed from a powder mixture

Table 8.1. DSC data for sintered Ti-50 at -% Ni cycled between -100 and +200°C (Cooling)

No. of cycles	M_s (°C)	M_f (°C)	M_{max} (°C)	Heat of transformation (kJ mol^{-1})	M_s-M_f
1	79.2	31.2	60.7	3.61	48.0
5	74.6	23.7	57.9	3.39	50.9
10	71.0	17.7	54.7	3.16	52.3
15	70.1	16.7	53.6	3.36	53.4
20	69.0	14.7	52.0	3.30	54.3
25	69.1	12.8	51.9	3.32	56.3
30	68.9	12.0	51.8	3.23	56.9

Table 8.2. DSC data for sintered Ti-50 at -% Ni cycled between -100 and +200°C (Heating)

No. of cycles	A_s (°C)	A_f (°C)	A_{max} (°C)	Heat of transformation ($KJ\ mol^{-1}$)	A_s-M_s (ΔT)
1	73.5	122.0	104.1	3.59	5.7
5	70.8	117.0	101.3	3.48	3.8
10	68.6	115.0	99.0	3.36	2.4
15	66.6	113.5	96.5	3.26	3.5
20	65.2	112.5	94.7	3.21	3.8
25	64.5	112.0	94.3	3.28	4.6
30	64.0	112.0	94.0	3.26	4.9

of Ti-50 at -% Ni at various pressures ranges from 155 to 929 MPa. The samples were held in the vacuum furnace at 900°c for 3 hours to allow significant solid state diffusion to occur before raising the temperature to 1000°C for 5 hours. This sequence of sintering was employed in order to reduce the amount of liquid phase occurring at 1000°C. The resulting sintered density ranged from 72.2 to 79.5% of theoretical value which is a considerable improvement when compared with the values (62 to 73%) obtained without the additional lower temperature sintering.

To investigate the manifestation of the shape memory effect, the cylindrical compacts of heights h_1 were compressed on an Instron machine at a cross head speed of 1 mm min^{-1} under an applied pressure of 300 MPa to a height, h_2. The degree of initial deformation, ε_d was determined from:

$$\varepsilon_d = \frac{h_1 - h_2}{h_1} \cdot 100\% \qquad 8.1$$

The deformed specimens were heated to 300°C (i.e. above the reversible transformation temperature range). This raised the sample height to h_3, and the amount of strain recovered, ε_r i.e. the shape memory effect, was obtained from:

$$\varepsilon_r = \frac{h_3 - h_2}{h_1} \cdot 100\% \qquad 8.2$$

The extent of recovery of the initial strain Δ_r was determined by:

$$\Delta_r = \frac{h_3 - h_2}{h_1 - h_2} \cdot 100\% \qquad 8.3$$

The results obtained are plotted in Figure 8.10. As would be expected the amount of initial deformation at a constant applied pressure decreases as the compact density rises. The level of shape recovery remains relatively constant at about 3% irrespective of the specimen density. The percentage of shape recovery of the initial strains, however, increases from 64 to 83 as the density is raised from 72.2 to 79.5% of theoretical value.

In Chapter 2.4.2 it was pointed out that the degree of shape recovery can also be influenced by prestraining. In the present study the effect of prestraining on the shape recovery of sintered equiatomic TiNi compacts was examined. Sintered samples (≅ 77% of theoretical density) were compressed at two different pressures (200 and 300 MPa). The extent of initial deformation was determined. The specimens were then heated to 300°C. The amount of shape recovery and its percentage of the initial strain were recorded. The samples were then compressed at a pressure of 200 MPa followed by a reversion treatment (i.e. heating to 300°C through the reversible transition temperature range). The results obtained are given in Table 8.3. It can be seen that the percentage shape recovery of the initial strains increases from 83 to 88 by prestraining to a stress level of 300 MPa.

Table 8.3 Strain recovery in sintered equiatomic TiNi compacts, after prestraining at 200 and 300 MPa, and heating to 300°C followed by a further compression loading at 200 MPa and a reversion heating to 300°C (sintered density ≅ 77% of theoretical value).

Prestrain pressure, MPa	0	200	300
% Initial deformation	0	3.23	3.92
% Recovery	0	2.65	3.07
% Shape recovery of initial deformation	0	82.0	78.3
After heating at 300°C and recompressed at 200 MPa			
% Initial deformation	3.26	2.98	2.75
% Recovery	2.71	2.53	2.42
% Shape recovery of initial deformation	83.0	85	88

8.6 Temperature Dependence of Tensile Strength

The tensile strength of TiNi samples pressed at 774.4 MPa and sintered for 5 hours at 1000°C are given in Figure 8.11 as a function of test temperature. There is considerable scatter in the data, but when average values are plotted (Figure 8.12), it is found that the curve has a minimum value at about 60°C. At higher temperatures a linear relationship between stress and temperature occurs, thus satisfying the Clausius-Clapeyron relation (Equation 2.5). The slope of the line, $d\sigma/dT$, is found to be 1.050 MPa/°C. By substituting the appropriate values from Tables 8.1 and 8.2 in Equation 2.5 (Chapter 2), the transformation strain, ε_t is determined to be 4.6% (see Appendix 8.1). This is in reasonable agreement with the 5.15% obtained by Melton and Mercier[157] for wrought specimens, considering the large scatter in the data for the sintered samples. However, both values are less than the 7.2% found in TiNi single crystals[30].

Scanning electron microscope examination of tensile specimens shows a ductile fracture with considerable dimpling (Figure 8.13). The fracture surface also shows relatively large voids, a reflection of the low density (≅ 77% dense) of the samples.

8.7 Discussion of Results

8.7.1 Hardness

Hardness measurement is widely performed in general metallurgy both for production control and in users' specifications. For wrought

products, reliable conversion factors are available which allow a reasonable estimation of other mechanical properties (e.g. Hv = 2.9 σ_y where σ_y is the yield strength of the material[158]). In the case of sintered porous specimens, the correlation of apparent hardness values with other mechanical properties such as UTS requires some caution. The macro hardness values obtained are a function of the plastic deformation of the metal matrix and of the pores. The latter may be regarded as a phase having zero hardness. Hence the hardness of samples identical in chemical composition and prepared under similar conditions will differ according to the amount of porosity. The greater the porosity the lower will be the apparent hardness[159]. Indeed, hardness determination is particularly valuable for detecting density variations in different areas of a green compact[150]. By comparison with hardness measurements, the value of tensile strength, for example, depends upon the total amount as well as the characteristics of porosity (e.g. for a given level of porosity a specimen with interconnected pores of irregular shape would be expected to give lower strength than a sample of the same composition but containing round isolated pores. The pores in the former being more effective as stress raisers[159]).

In the present study, the rise in hardness value to a maximum followed by a decrease as the sintering temperature is raised (Figure 8.1) can be ascribed to the combined effects of diffusional homogenization (see Figure 7.11, Chapter 7.2.4) and an increase in porosity with increasing temperature. The dependence of hardness on titanium particle size (Figure 8.2) is directly attributable to the change in porosity (see Figure 7.12, Chapter 7).

8.7.2 Hardening Effect in Ti-Ni Alloys

The results obtained from this investigation have demonstrated that Ti-Ni alloys with compositions ranging from 52 to 55 at -% Ni are capable of being quench-hardened. The composition at which the maximum hardness value is obtained is about 54 at -% Ni which corresponds to the composition of the phase boundary between TiNi and TiNi + $TiNi_3$ at 1000°C according to the phase diagram proposed by Duwez and Taylor[37] (Figure 3.1a, Chapter 3.2). This observation suggests a link between the hardening effect in Ni-rich alloys and the solubility of Ni in TiNi compound.

It is well known that intermetallic compounds which have a range of homogeneity contain structural defects at non-stoichiometric concentrations to achieve the required ordered structure[160]. It has been demonstrated that the concentration of the defects require is 1×10^{-2} for substitutional atoms and 2×10^{-2} for vacancies at the composition of 1 atomic percent off the stoichiometric composition. In TiNi, the excess nickel is present as substitutional atoms[41,43]. It is considered that the greater part of these defects are retained by quenching. In compounds such as NiAl which have the same CsCl (body centred cubic, B2) structure as TiNi and a wide homogeneity range, a considerable rise in hardness has been observed with increasing amount of defects. The mechanism of hardening by structural defects which are induced by deviation from the stoichiometric composition at the quenching temperature is only effective when the homogeneity range becomes narrower with decreasing temperature[161].

In the present study, the samples containing excess nickel ($\geq$ 52 at -% Ni) shows second phase ($TiNi_3$) precipitates when furnace cooled from 1000°C, whereas water quenched specimens are found to be single phase. In contrast, alloy of equiatomic concentration displays a single phase in both the as quenched and furnace cooled conditions. There is, thus, a decrease in solubility limit of Ni in TiNi compound as the temperature is lowered. By water quenching, the precipitation of the excess nickel is suppressed. It is probable that the quench hardening capability of Ni-rich alloys is a result of the supersaturated structure produced by quenching.

These results also indicate that the homogeneity range of TiNi compound is narrower than 54 at -% Ni suggested by Margolin et al[39] (Chapter 3.2, Figure 3.1b). Also, since the sample of equiatomic composition is a single phase both in the as quenched and furnace cooled conditions, the decomposition of TiNi compound into a mixture of Ti_2Ni and $TiNi_3$ above 800°C, proposed by Duwez and Taylor[37] (Figure 3.1a, Chapter 3.2) is not confirmed by the present study.

8.7.3 Transformation Temperature

The differential scanning calorimetry (DSC) results show that the transformation temperatures of alloys containing 49 and 50 at -% Ni are insensitive to heat treatment. Raising the nickel content significantly decreases the transformation temperature. Alloys of nickel-rich compositions show a marked variation in transformation

behaviour with the prior heat treatment. In the furnace cooled condition the transformation temperature of a nickel-rich sample is slightly above room temperature whereas in the water quenched state the sample does not transform even when cooled to -100°C in the DSC.

Slow cooling in the furnace allows the precipitation of excess nickel from the high temperature TiNi compound. The precipitation process usually begins with the atomic rearrangement of fine particles which are coherent with the matrix. Such precipitates are known to obstruct the shape change for martensitic reaction[21]. The martensite formation is thus more difficult and consequently the M_s temperature decreases. As the precipitated particles become larger, coherency is lost, resulting in an increase in M_s. Thus a furnace cooled nickel-rich sample with relatively large $TiNi_3$ particles would be expected to give a higher M_s temperature than water quenched specimen with incomplete precipitation (Figure 8.4c, d).

8.7.4 Thermal Cycling

When a TiNi specimen prepared by conventional methods is subjected to thermal cycling a decrease in temperature hysteresis and transformation temperature is observed (e.g. Ref. 25). After a certain number of cycles (Perkins[162] reported about 12) saturation of this effect is reached and the transition parameters remain nearly constant with further cycling. Similar behaviour is demonstrated in the sintered specimens studied in the present work (Figure 8.9). This observation indicates that the parent phase is able to exist over a

wider range of temperature. It may therefore be said that thermal cycling has a stabilizing effect on the parent phase relative to the martensite.

The ability of cycling to lower the transformation temperature has been attributed to a stabilization effect associated with dislocation debris generated by the formation and reversal of the martensite phase. Microstructural evidence of the generation of substructural dislocations due to thermal cycling has been reported by several workers (e.g. Refs. 16, 33, 162) in many alloy systems (e.g. TiNi, Cu-Zn-Al). It is suspected that the dislocation debris is the accumulation of sessile dislocations formed either by dissociation of interfacial dislocations or the interaction of these dislocations with annealed-in dislocations during the forward or reverse motion of the martensite/parent phase interface.

One of the characteristics of thermoelastic transformation considered in Chapter 2.4.4 is that the growth of martensite plates must cease before the elastic limit of the material is reached. That is, no plastic deformation is involved, since this constitutes an irreversible process. Clearly the build-up of dislocations during cycling until the saturation point is reached where no further dislocations are generated, suggests that a "truly" thermoelasic behaviour is attained after some number of thermal cycles. The saturation of this irreversible behaviour can be envisaged as the attainment of microstructural stabilization in the form of transformation strain hardening to a point where further deformation

is able to be resisted without exceeding the elastic limit of the material.

It has been pointed out in Chapter 5.3.2 that the strain field associated with a dislocation can enhance the formation of martensite by providing a favourable interaction with the strain field of a martensite nucleus, thereby resulting in an increase in M_s. It is also mentioned that the dislocations can suppress the growth of nuclei. An increase in dislocation density due to thermal cycling and the associated decrease in M_s would suggest that the latter of the two opposing effects of dislocations on the martensitic reaction dominates.

8.7.5 Shape Memory Effect in Sintered TiNi Compacts

The porosity in sintered specimens gives rise to a reduction in the load bearing section of the material. Consequently, for a given compressive load the initial deformation strain becomes higher as the sample density decreases. As the initial strain is raised the proportion recovered on heating also becomes smaller.

The importance of the amount of initial deformation on the degree of shape recovery has been considered in Chapter 2.4.3. It is pointed out that if a shape memory material is stressed such that irreversible plastic deformation occurs, complete reversion to its initial shape will be hindered. It is likely that the reduction in the amount of shape recovery with density (Figure 8.10) is a result of a localized plastic deformation caused by porosity. Further evidence

in support of this view is obtained from the UTS data reported in Section 8.6. In that instance, the mean UTS of the porous specimens (≅ 77% dense) tested at room temperature (Figure 8.12) is found to be 290 MPa (which is slightly lower than the 300 MPa employed to compress the samples of the present study). Examination of those tensile test pieces shows a ductile fracture. By prestraining, the proportion of the initial strain recovered during heating (as in chapter 2.4.4) can be enhanced (Table 8.3).

The total recoverable strain during the reverse transformation of sintered specimens is found not to be significantly different from those of conventionally processed non-porous specimen. The value obtained is however, lower than that found in single crystal specimens. This can be attributed to the effects of grain boundaries in limiting the recoverable strain (Chapter 2.4.4).

8.8 Summary

The data reported in this chapter have shown that no simple relationship exists between the apparent hardness of TiNi compacts and sintering temperature. The apparent hardness of a specimen is related to the combined effects of diffusional honogenization and a rise in the amount of porosity with temperature.

TiNi compound has a wide homogeneity range (49 to 54 at -% Ni) at high temperature (e.g. 1000°C). As the temperature is lowered the solubility of Ni in TiNi decreases. Fast cooling of samples

containing nickel in excess of 51% from about 1000°C produces a supersaturated structure with a considerable increase in micro-hardness.

The transformation temperature of a specimen of equiatomic concentration is insensitive to heat-treatment. Raising the nickel content significantly lowers the transition temperature and renders it susceptible to cooling rate. This phenomenon has been explained in terms of the precipitates formed in the nickel-rich alloys. However, the transformation temperatures of samples of equiatomic composition are lowered by thermal cycling. This is associated with the build-up of dislocation density during cycling.

Although the total recoverable strain observed in sintered samples is not significantly different from those found in wrought specimens, the pores in the former can promote plastic deformation resulting in a reduction in the degree of strain recovered during heating. The extent of strain recovery can be enhanced by prestraining.

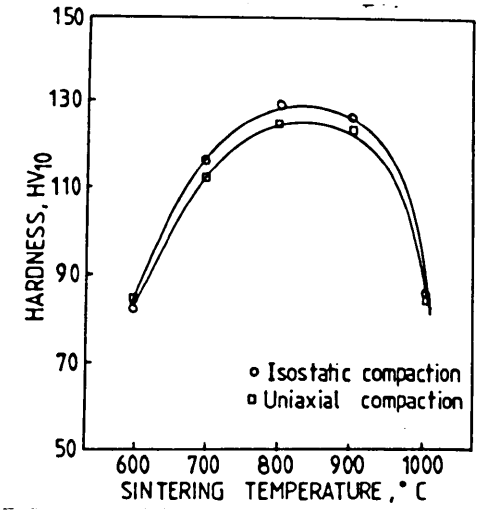

Figure 8.1 Variation of macrohardness with sintering temperature of compacts pressed at 503 MPa (isostatic) and 774.4 MPa (uniaxial) and sintered for 5 hours.

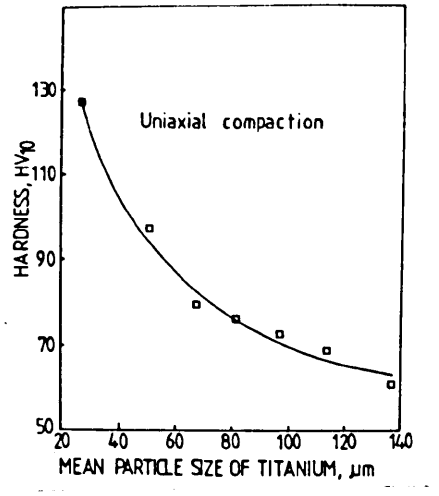

Figure 8.2 Dependence of hardness on titanium particle size for compacts pressed at 774.4 MPa and sintered for 5 hours at 1000°C.

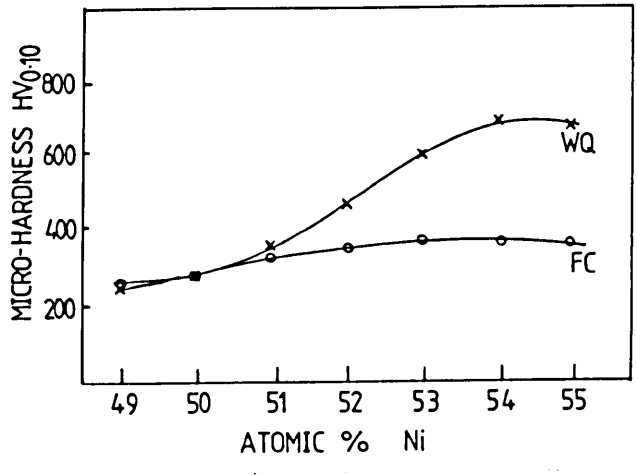

Figure 8.3 Variation of microhardness with composition of water quenched (WQ) and furnace cooled (FC) Ti-Ni specimens.

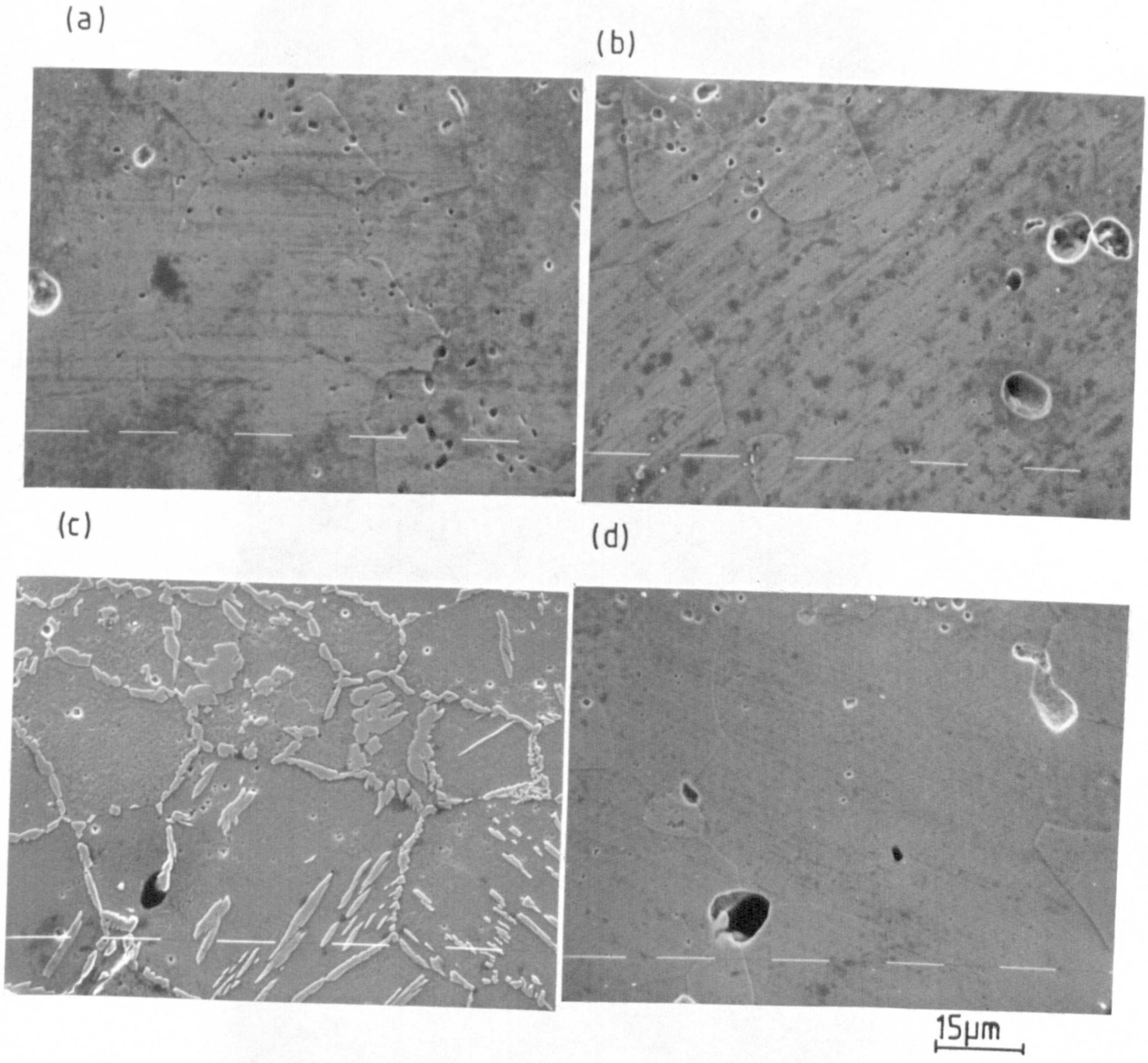

Figure 8.4 Scanning electron micrographs of

(a) equiatomic TiNi specimen furnace cooled from 1000°C

(b) equiatomic TiNi specimen water-quenched from 1000°C

(c) Ti-54 at -%Ni sample furnace cooled from 1000°C

(d) Ti-54 at -%Ni sample water-quenched from 1000°C.

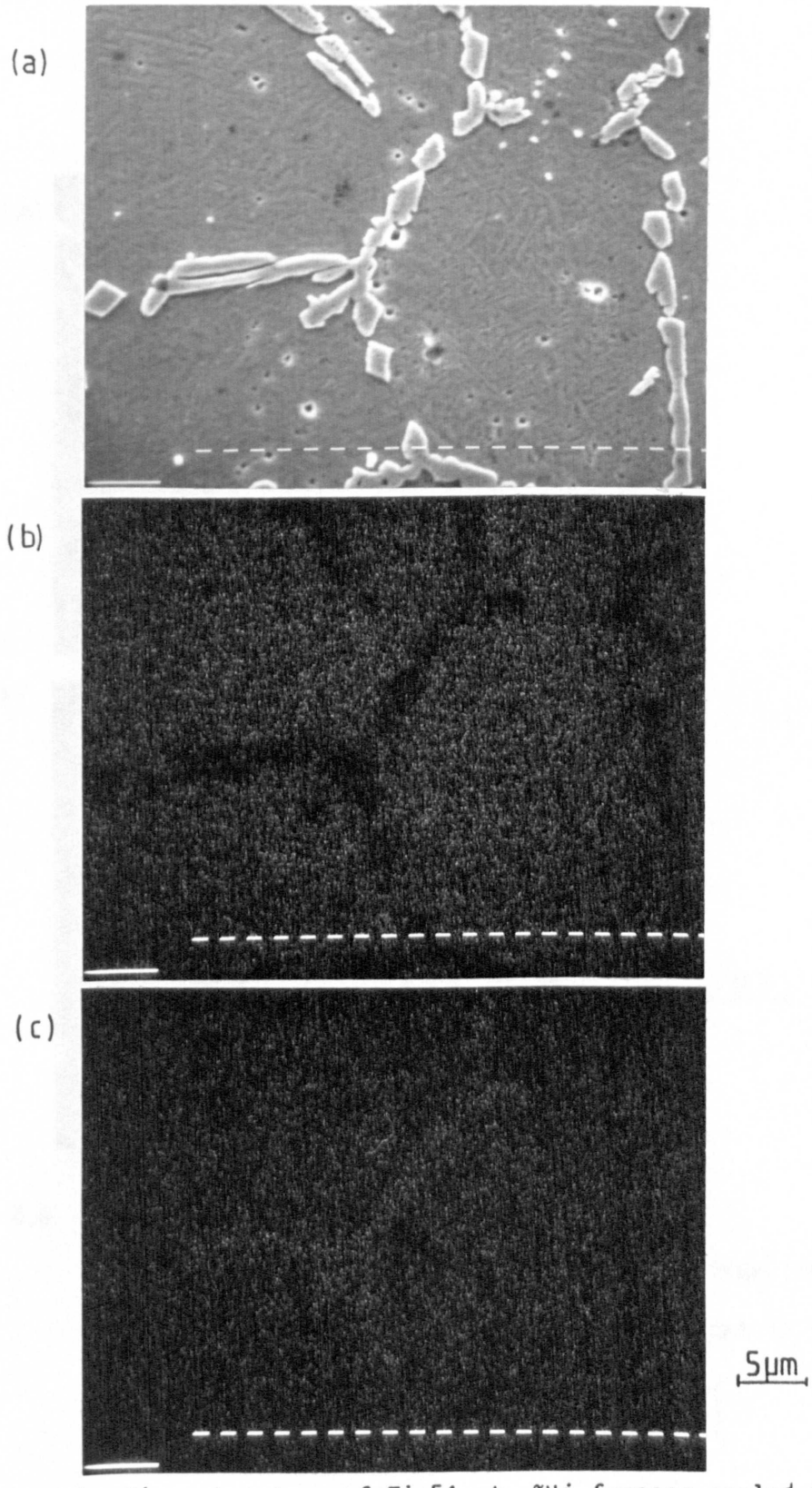

Figure 8.5 (a) Microstructure of Ti-54 at -%Ni furnace cooled from 1000°C;

(b) Ti X-ray image of (a);

(c) Ni X-ray image of (a).

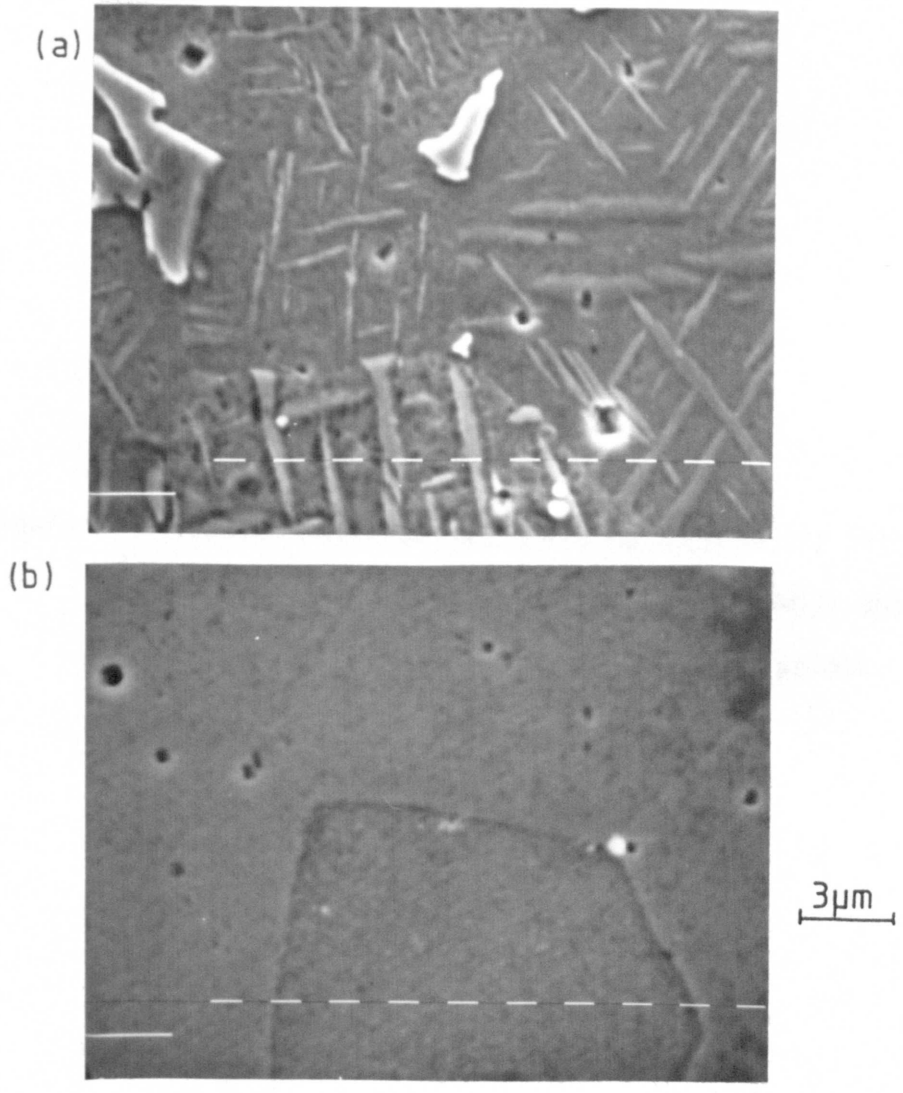

Figure 8.6 Microstructures of Ti-54 at -% Ni specimens

(a) furnace cooled and (b) water quenched from 1000°C showing the presence of martensite plates in the slowly cooled sample (a).

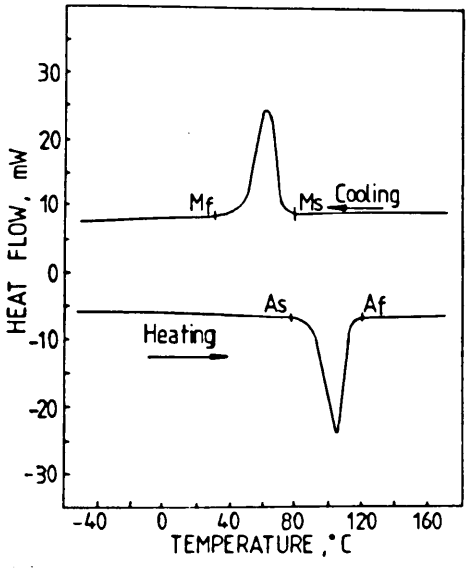

Figure 8.7 Typical differential scanning calorimetry curves for a pressed and sintered Ti-50 at -% Ni sample showing the reversible transformation temperature points.

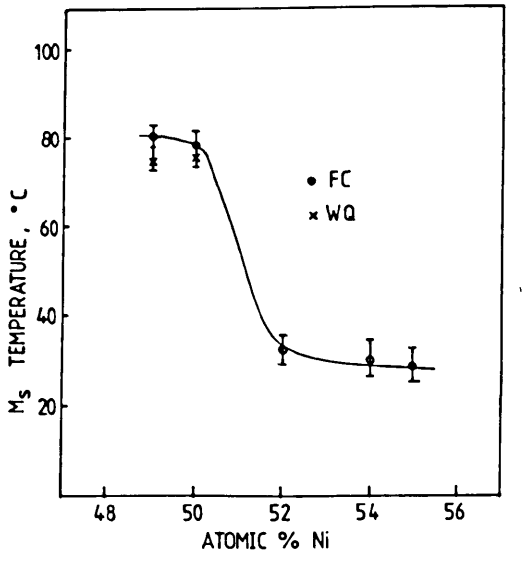

Figure 8.8 Effect of composition on the transformation temperature, M_s of specimens cooled from 1000°C by either water quenched (WQ) or furnace cooling (FC).

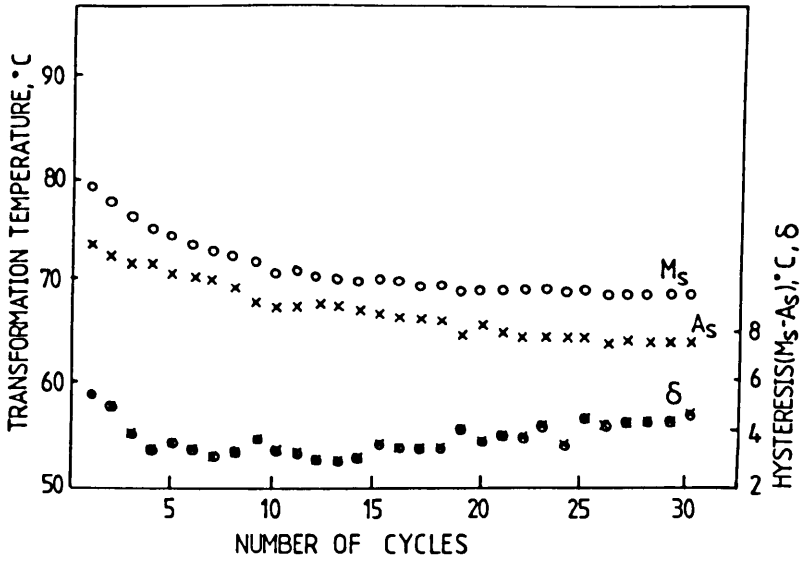

Figure 8.9 Influence of thermal cycling on the transformation temperatures, M_s and A_s, and the transformation hysteresis $(M_s - A_s)$.

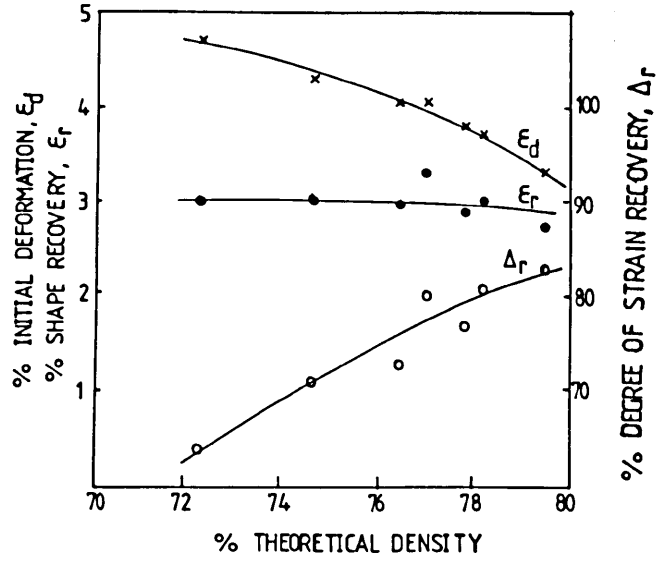

Figure 8.10 Variation of initial deformation, ε_d, strain recovered, ε_r and the degree of strain recovery, Δ_r with density for Ti-50 at -%Ni specimens compressed at 300 MPa and heated to 300°C.

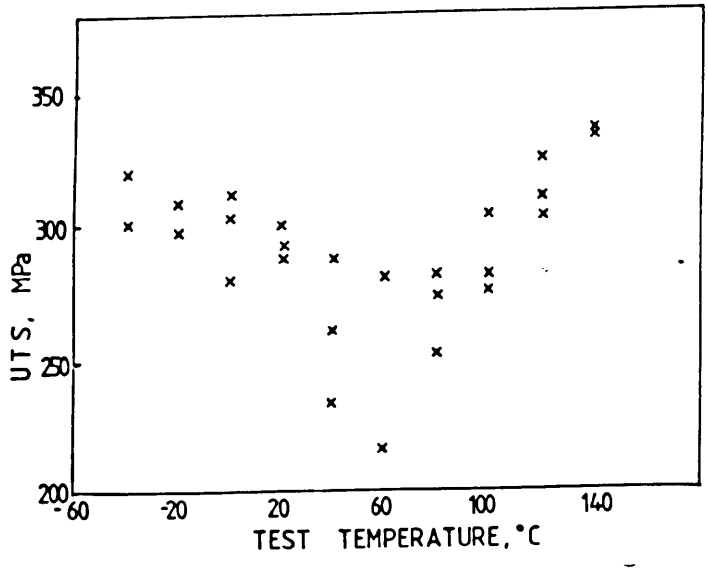

Figure 8.11 Dependence of tensile strength on test temperature.

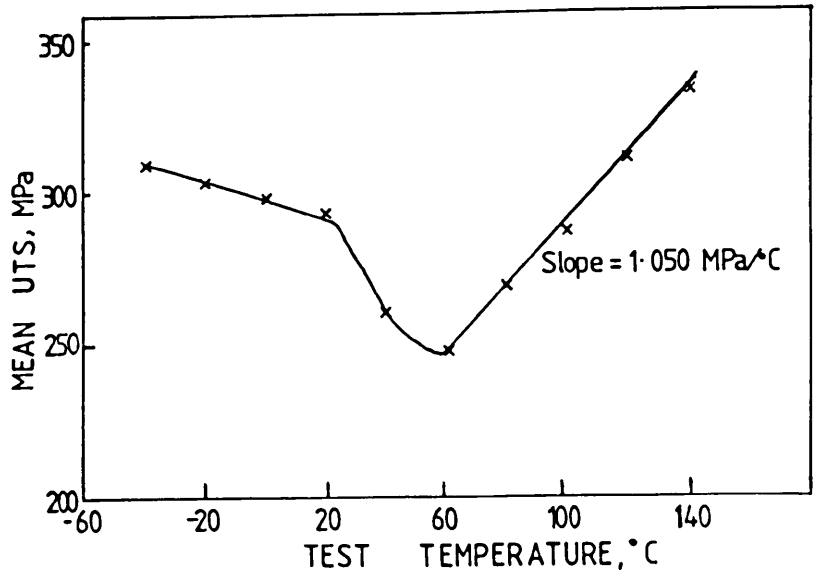

Figure 8.12 Plot of average tensile strength against test temperature for equiatomic TiNi samples.

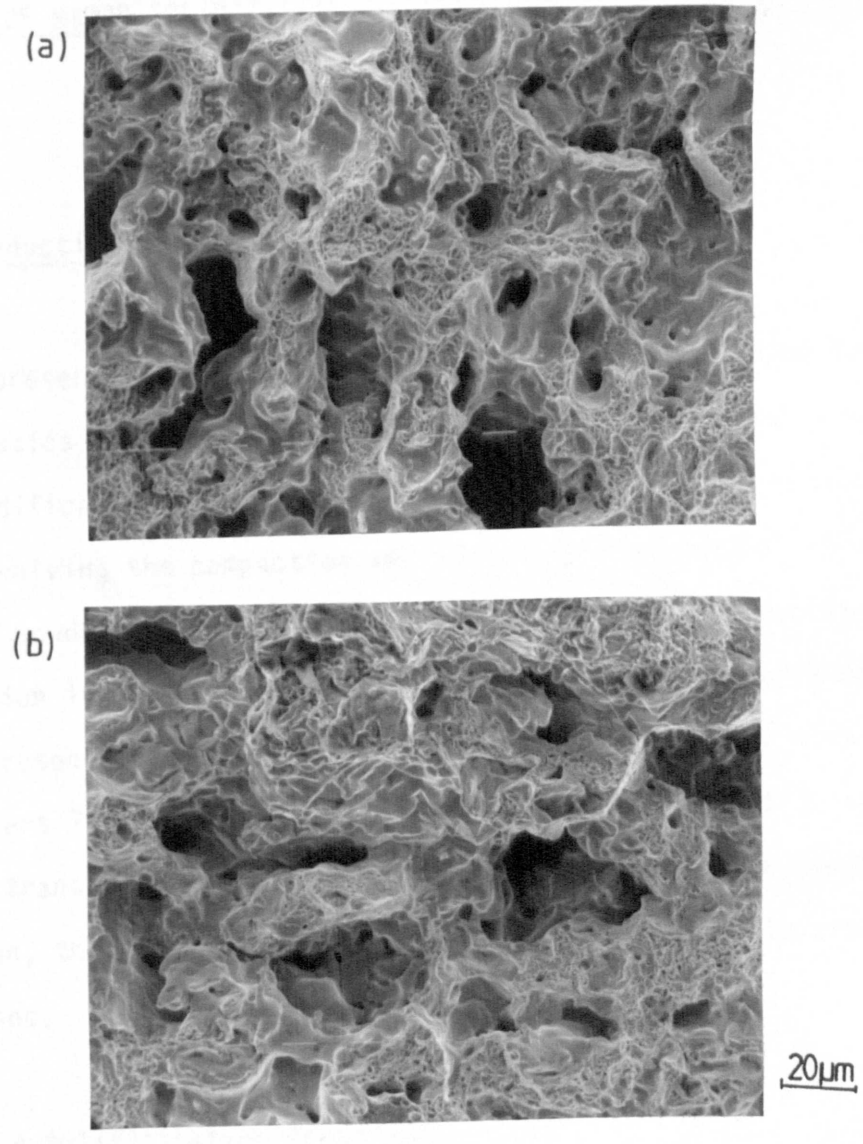

Figure 8.13 SEM fractographs of tensile pieces tested at (a) 140°C and (b) -60°C.

CHAPTER 9

EFFECT OF RAPID SOLIDIFICATION PROCESSING ON THE PROPERTIES OF EQUIATOMIC TiNi ALLOY

9.1 Introduction

The present research programme was set out to determine the characteristics of TiNi alloys produced by both powder metallurgy and rapid solidification techniques. In Chapter 7 and 8, the results from a study involving the compaction and sintering of elemental titanium and nickel powders were described. In this chapter the results of an investigation into the properties of rapidly solidified equiatomic TiNi are presented. Where necessary, a comparison is made with data from Chapters 7 and 8. The properties studied are microstructure, hardness, transformation characteristics and consolidation behaviour. In addition, the effects of heat treatment on some of these properties are examined.

9.2 Rapid Solidification Processing

The rapidly solidified material was prepared by the melt spinning technique which was described in Chapter 5.2. Powder compacts which had previously been made by compaction and sintering of elemental powders were melted and quenched onto a water cooled wheel with a peripheral speed of 27 ms^{-1}. The ribbon produced were about 3 mm wide and up to 50 μm in thickness. Full details of experimental conditions were described in Chapter 6.5.

9.3 Microstructures

9.3.1 Scanning Electron Microscopy

Microstructural observations on polished and etched samples were undertaken using a Philip 501 B scanning electron microscope (SEM). Typical microstructures of rapidly solidified ribbon in the longitudinal cross-section are shown in Figure 9.1. The structure consists predominately of columnar grains extending from the wheel contact surface through the entire thickness of thin ribbons (Figure 9.1a). In the case of thicker material, equiaxed grains are found near the top surface (Figure 9.1b).

The microstructures of an in-plane cross-section of spun ribbon and wrought sample are presented in Figure 9.2. The results demonstrate the significant grain refinement caused by rapid solidification. The mean grain size in spun alloy is about 4 μm which is at least an order of magnitude smaller than that which can be obtained in wrought products. The actual size of individual grains in the ribbon however varies considerably from 0.5 to 10 μm which is an indication of the high and non-uniform undercoolings within the ribbon during solidification. The influence of undercooling on grain size was considered in Chapter 5.3.1. It can also be observed that the structure of the wrought sample contains some second phase oxide particles which are frequently observed in TiNi alloy processed by ingot metallurgy methods (e.g. Ref. 36, 41). Alloys based on TiNi compound are conventionally produced by arc or induction melting

followed by mechanical working (hot and cold), and machining to final dimensions. During high temperature processing, oxygen pick-up frequently occurs. In contrast, the rapidly solidified material is free of oxide inclusions. Another notable difference between the two structures is that there are no martensite plates in the rapidly solidified ribbon. This means that the transformation temperature, M_s, is depressed by rapid solidification.

On ageing the spun ribbon at 900°C for five hours, the mean grain size increases to about 15 μm (Figures 9.3 and 9.4). The actual size of individual grains varied within ± 5 μm of the mean. The fraction of martensite plates present also grows with heat treatment time, suggesting a rise in M_s temperature. These results are consistent with the DSC data discussed in Section 9.4.

9.3.2 Transmission Electron Microscopy and Powder X-ray Diffraction

The structures of the phases present at room temperature were determined using transmission electron microscopy and powder X-ray diffraction techniques. Details of specimen preparation methods had been described in Chapter 6.8. The thinned foils were examined in a Philips 301 electron microscope. The applied voltage was 100 kV. A standard aluminium sample was employed to determine the camera constant. X-ray diffraction studies were undertaken in a Deby-Scherrer powder camera. Cu $K\alpha$ radiation was utilised with a Ni filter.

Figure 9.5 shows a bright field micrograph and a series of electron diffraction patterns of the phase observed in the rapidly solidified TiNi ribbon. The electron diffraction patterns could be indexed in terms of the bcc CsCl structure with a lattice parameter of a_o = 3.015 Å reported by Otsuka et al[42]. The patterns, Figure 9.5b, c, d, ,e, and f are respectively identified as $[100]_{B2}$, $[113]_{B2}$, $[110]_{B2}$, $[111]_{B2}$ and $[120]_{B2}$ zones of the crystal structure[163,164]. The patterns corresponding to $[110]_{B2}$, $[111]_{B2}$, and $[120]_{B2}$ exhibit the extra reflections at approximately 1/3 positions of the B2 reciprocal lattice spacings found by many investigators (e.g. Refs. 49, 165). According to the DSC data, the M_s temperature (16°C) of the ribbon is below room temperature. However, after cooling to the thinning temperature (-60°C) and allowing the foil to reheat to room temperature, some retained martensite would be expected to be present because of thermal hysteresis. This is evident in the bright field micrograph in Figure 9.5a and consequently some additional martensite spots such as the $[012]_M$ indicated in Figure 9.5d with lattice parameters a = 2.889 Å, b = 4.120 Å, c = 4.622 Å, β = 96.8°[42] are found.

The X-ray powder diffraction pattern of the as-spun ribbon is given in Figure 9.6a. The pattern obtained after heat treating the ribbon at 800°C for 5 hours is also shown for comparison (Figure 9.6b). For the as-quenched sample a number of extra weak reflections (e.g. 'X' in Figure 9.6a) are present in addition to the reflections corresponding to the high temperature B2 phase which could be indexed using the lattice parameter a = 3.015 Å. The extra reflections

could be indexed on the basis of a rhombohedral unit cell with the lattice parameters a = 6.02 Å and α = 90.7° proposed by Dautovich and Purdy[43]. The only exception being the very weak reflection 'y' (Figure 9.6a)which could neither be indexed in terms of a B2 cubic cell nor the rhombohedral type. Another salient feature that can be noted from the pattern is that some of the B2 reflections (e.g. $[011]_{B2}$) are split. This is in accord with the reports by other workers (e.g. Refs. 50, 51, Chapter 3.3). The splitting is the result of the distortion involved in the B2-rhombohedral transformation. The rhombohedral form is usually referred to as R-phase[43,48].

After heat treating the ribbon at 800°C for 5 hours, the intensities of the B2 reflections increase while the reflections corresponding to the rhombohedral phase virtually vanish (Figure 9.6b). The disappearance of the R-phase reflections is also accompanied by a reduction in splitting of the B2 reflections and a rise in M_s. The results from a DSC study showed that a sample taken from the same ribbon which was used for the X-ray investigation had an M_s of 14°C in the as-quenched conditions. The corresponding value after heat treatment was 18°C. Full details of the X-ray data obtained are shown in Tables 9.1 and 9.2 along with the calculated values. The d-spacing calculated are shown as d_{cal} while those observed are indicated as d_{obs}.

Table 9.1. X-ray powder diffraction data for as-spun Ti-50 at -%Ni Ribbon

Line	θ	d_{obs}	d_{cal}	hkl	Relative Intensity
1	19.64	2.294			w
2	21.22	2.130	2.131	$(110)_{B2}$	vs
3	22.56	2.010	2.018	$(212)_{R}$	s
4	30.80	1.506	1.507	$(200)_{B2}$	vs
5	34.00	1.330	1.320	$(421)_{R}$	w
6	38.78	1.231	1.231	$(211)_{B2}$	w
7	40.83	1.179	1.173	$(333)_{R}$	w
8	46.36	1.065	1.066	$(220)_{B2}$	vw
9	54.10	0.951	0.953	$(310)_{B2}$	w
10	55.87	0.931	0.940	$(206)_{R}$	w
11	60.91	0.882	0.881	$(136)_{R}$	vw
12	62.55	0.869	0.870	$(222)_{B2}$	vw
13	73.24	0.805	0.806	$(321)_{B2}$	s

order of intensities vs > s > w > vw

Table 9.2. X-ray powder diffraction data for heat treated (5 hr at 800°C) Ti-50 at -% Ni Ribbon

Line	θ	d_{obs}	d_{cal}	hkl	Relative Intensity
1	19.63	2.294			w
2	21.22	2.130	2.132	$(110)_{B2}$	vs
3	22.38	2.025	2.018	$(212)_{R}$	vw
4	30.60	1.514	1.508	$(200)_{B2}$	vs
5	38.49	1.239	1.231	$(211)_{B2}$	s
6	46.32	1.066	1.066	$(220)_{B2}$	w
7	54.05	0.951	0.953	$(310)_{B2}$	s
8	62.50	0.869	0.870	$(222)_{B2}$	vw
9	73.25	0.805	0.806	$(321)_{B2}$	s

order of intensities vs > s > w > vw

9.4 Transformation Characteristics

The transformation temperatures of specimens were determined using a DuPont 1090 differential scanning calorimeter (DSC) already described in Chapter 6.7. The results show that the martensitic start temperature (M_s) of equiatomic TiNi is depressed by rapid quenching. A mean M_s value for the as-spun ribbon is 16°C as compared with 79.2° for the sintered material from which the ribbon was produced. Typical DSC cooling curves are presented in Figure 9.7. In addition to the depression in M_s, another notable difference between the transformation behaviour of the two materials is that the exothermic peak associated with the martensitic reaction for the starting material is narrow and clearly defined while that for the rapidly soldified specimen is broad and appears in two steps.

On ageing the spun ribbon at different temperature up to 900°C, a sigmoidal increase in M_s is seen as the ageing temperature is raised through the order-disorder temperature range (600 - 700°C, Figure 9.8). Apart from the rise in M_s, the DSC curves for ribbons which were aged at high temperatures ($\geq$ 800°C display a one step exothermic peak (e.g. Figure 9.9) which is in contrast with the two steps observed for the as-spun sample. It is found that the M_s rises from 20 to 26°c as the ageing time at 900°C is increased from 1 to 5 hours (Figure 9.10). The energy of transformation also decreases with increasing treatment time and temperature (Figure 9.8, 9.10) suggesting that the martensite formation is becoming easier.

9.5 Hardness Determination

The microhardness values for aged equiatomic TiNi ribbons at different temperature are plotted in Figure 9.11. It is apparent that the hardness of this alloy is not affected by heat treatment. This result is consistent with the data for the heat treated sintered samples presented in Chapter 8.3 (Figure 8.3).

9.6 Powder Processing and Consolidation

In Chapter 5.4, it was mentioned that powder metallurgy techniques are commonly employed to consolidate rapidly solidified (RS) products into bulk engineering products. In this study, some of the RS ribbons were crushed and the consolidation response of the resulting pre-alloyed powder was examined and compared with that of elemental blends. The results obtained are given in the following sections.

9.6.1 Powder Characteristics

The morphology of the milled pre-alloyed powder is shown in Figure 9.12. The particles are of irregular shape with some evidence of deformation and cold welding, reflecting the ductility of the melt spun material. The particle size ranges from 5 to 150 μm. The apparent density, tap density and sieve analysis for a 100 g sample of the powder are given in Table 9.3.

Table 9.3 RS powder characteristics

Sieve analysis	Particle size	% retained
Apparent density	150	0
1.895 Mg m^{-3}	125	13.0
(29.4% of theoretical)	106	13.2
Tap density 2.176 Mg m^{-3}	90	13.6
(33.8% of theoretical)	75	10.1
	63	12.6
	38	14.0
	<38	23.5

9.6.2 Powder Consolidation

The compressibility curve of the pre-alloyed powder is plotted in Figure 9.13 and compared with that of elemental powders (Chapter 7.2.2). Every single experimental point shown constitutes a mean value obtained from three independent samples. It should be noted that the scatter between the density values determined for individual specimens was minimal. It can be seen that the green density of uniaxially compacted pre-alloyed powder sample is directly proportional to pressure over the range of compaction pressures employed. For a given pressing condition a lower green density is attained with milled particles. For instance, at a consolidation pressure of 774 MPa, the elemental blend achieves a green density of 81% of theoretical value using a uniaxial die press, while the equivalent amount for the pre-alloyed material is 66%. The difference in compaction behaviour is attributable to the inherent high hardness of the milled pre-alloyed particles.

The green density data are replotted in Figure 9.14 for comparison with the sintered density. It is apparent that while densification occurs during the sintering of pre-alloyed powder compacts, the sintered densities of elemental blend samples are in most cases lower than the green densities.

The variation of density and hardness of pre-alloyed powder compacts with sintering temperature is presented in Figure 9.15. Each macrohardness value plotted represents an average from three specimens using a 10 kg load. The scatter between separate readings was within ± 5 HV of the mean result. As would be expected, the density and apparent hardness rise with sintering temperature. The rate of increase is quite low at temperature below 1100°C ($\leq$ 1050°C), which is consistent with the microstructural observations described in the next section.

9.6.3 Microstructures of Sintered TiNi Alloy Compacts

The microstructures of pre-alloyed powder compacts pressed at 774 MPa and sintered at various temperatures for a standard time of 5 hours are presented in Figure 9.16. The corresponding results for the elemental blends are also given for comparison.

At 700°C (Figure 9.16a), interdiffusion of titanium and nickel occurs in the elemental specimens and compositional homogenisation is virtually complete at 1000°C (Figure 9.16c). The amount of porosity also increases with sintering temperature. In contrast , RS

pre-alloyed powder compacts shown no evidence of particle sintering even at 1050°C (Figure 9.16d). Only at 1100°C is interparticle neck growth observed leading to densification of the compact (Figure 9.16e-f). The increase in the total volume of porosity during sintering of elemental powder compacts has been related to the difference in interdiffusion rates of titanium and nickel, and the occurrence of a transient liquid phase at temperatures above the eutectic temperature (Chapter 7.3.2). A significant reduction in the level of porosity was achieved by hot isostatic pressing of the sintered elemental blend compacts at 950°C for 3 hours (Chapter 7.2.6).

Despite the need to sinter the RS powder at much higher temperatures, the grain size of the resulting compact is still smaller than that found in elemental blends. The grain diameter of the pre-alloyed compact sintered at 1120°C varies from 10 to 20 μm while that of elemental mixture sintered at 1000°C ranges from 20 to 40 μm (Figure 9.17).

9.7 Discussion of Results

9.7.1 Crystal Structures

It is well established that the high temperature phase of TiNi compound has the ordered bcc CsCl (B2) structure and upon cooling undergoes a diffusionless shear transformation either directly or through an intermediate rhombohedral phase to a martensitic product

(Chapter 3.3). Among other effects, the intermediate transition is characterised by extra diffraction spots at approximately 1/3 positions of the B2 reciprocal lattice[49], splitting in some of the B2, X-ray reflections[50,51], and a two-steps exothermic peak in differential thermal analysis plots during cooling (e.g. Refs. 52-54). The occurrence of these effects is confirmed in the present investigation (Figures 9.5, 9.6, 9.7).

It has been suggested[49,165] that the B2 cubic to rhombohedral transformation is reversible without hysteresis and of the second order type, involving incipient instability in the cubic lattice. In a second or higher order transition the X-ray reflections of the parent phase change continuously to that of the new phase resulting in shift, broadening and eventual splitting of the reflections[167]. This form of reaction is to be contrasted from that of first order (e.g. a martensitic transformation) in which both the parent and martensite phases remain intrinsically stable through the transition region[49]. In this case the lattice is discontinuous. Thus the parent phase reflections do not shift and martensite reflections appear discontinuously during the reaction.

The transition from the high temperature B2 phase through the R-phase to martensite is prompted by factors (such as thermal cycling or the substitution of Ni by a few percent of Co) which lower M_s relative to T_R (the rhombohedral transformation temperature)[48,49,165]. Of the two temperatures, M_s is more sensitive to processing conditions[48,166]. In the present work,

rapid solidification processing results in significant depression in M_s of equiatomic TiNi and effects (e.g. splitting of reflections, two-steps DSC transformation peaks) related to the rhombohedral reaction are observed. Upon ageing, the M_s rises, and a single step transition is found.

Although the martensitic transformation temperature M_s for the as-spun ribbon is below room temperature, the ribbon demonstrates a well defined shape memory behaviour (Figure 9.18). This is consistent with the reports by Nishida and Honma[168], and Ling and Kaplow[166] that the B2→R transition is thermoelastic and thus contributes to the shape recovery process.

9.7.2 Transformation Behaviour

The results from the differential scanning calorimetry study show that the martensitic reaction temperature, M_s of TiNi alloys is lowered by rapid solidification processing. Factors which could affect the transformation behaviour following rapid quenching include: the concentration of quenched-in vacancies and dislocation density, the degree of order, and grain size (Chapter 5.3).

Since the equilibrium concentration of vacancies increases exponentially with temperature, rapidly solidified alloys would be expected to have quenched in vacancy concentrations in excess of those found in materials that have been quenched from solid state[132] (Chapter 5.3.2). These excess vacancies tend to be attracted together

to form vacancy clusters which may subsequently collapse into dislocation loops (e.g. Refs. 134, 135). There is however, substantial experimental evidence (e.g. Refs. 130, 136) which shows that while the quench rate during the transformation from liquid to solid is quite high in rapid solidification processing, the subsequent cooling rate to ambient temperature can be relatively low. There is therefore the possibility that some of the excess vacancies could anneal out to a number of sinks (e.g. grain boundaries). In alloys which display the martensitic phase transformation, however, the presence of a high vacancy concentration would be expected to promote the reaction by reducing the driving force necessary for the transformation. Thus the M_s tends to rise (e.g. Ref. 130, Chapter 5.3.2). Since in the present case a decrease in M_s is observed, this factor may not be significant.

Another consequence of rapid solidification which could affect the transformation behaviour of martensitic alloys is the increase in dislocation density. The strain field associated with a dislocation can enhance martensitic formation and consequently raises the M_s by providing a favourable interaction with the strain field of a martensite nucleus[24]. Although, it is also likely that nuclei growth can be restricted by dislocations[21]. For instance, the results presented in Chapter 8.7.4 show that thermal cycling has the effect of lowering the M_s temperature of TiNi alloy. In specimens which have been subjected to such treatment, a considerable amount of microstructural evidence (e.g. Refs. 16, 33, 161, Chapter 8.7.4) of the generation of dislocations has been reported. Thus the increase

in dislocation density due to rapid solidification processing could be a contributing factor to the depression in M_s observed in the present investigation.

Wang et al[169, 170] reported that the equiatomic TiNi solidifies to form a disordered structure, which on further cooling undergoes an order-disorder reaction at temperatures between 600 and 700°C. This sequence of transformations was confirmed by Zijderveld et al[171], whereas Hirano and Ouchi[172] and Wasilewski et al[52] could not obtain any evidence of such a series of transitions. Instead, they reported that the liquid TiNi solidifies to form an ordered structure and does not experience additional order-disorder reactions during further cooling. Thus, the occurrence of an order-disorder transition in the solid state in TiNi remains controversial. However, if it exists, rapid quenching from the liquid state may suppress it since the reaction is diffusion controlled. Suppression of the ordering transformation in CuZnAl shape memory alloys as a result of rapid solidification has been reported by Perkins[138] (Chapter 5.3.3). In that instance, Perkins also observed that the M_s temperatures of the alloys studied increase with the degree of ordering. In the present investigation, the sigmoidal rise in M_s as the ageing temperature is raised through the apparent order-disorder region (Figure 9.8) tends to suggest that the state of order of the rapidly solidified TiNi ribbon is a contributing factor to the observed depression in M_s value. However, no evidence of the presence of superlattice reflections is found in the X-ray diffraction pattern of ribbon which had been aged for 5 hours at 800°C (i.e. above

the proposed ordering reaction range). It is therefore not certain whether the rise in M_s is the result of ordering in the present case.

Another parameter which could lower the transformation temperature is the refined grain size of the rapidly soldified ribbon. It is known that grain boundaries can act as barriers to martensitic transformation as a result of the extra energy required for complementary shear during the process[21]. Thus, fine grained ribbon with a higher grain boundary area would be expected to give a lower M_s than the coarse grained pre-sintered material. Evidence in support of this view is provided by the result from ageing treatments. It is observed that the M_s rises from 20 to 26°C (Figure 9.10) as the grain size changes from 4 to 15 μm (Figure 9.3). A depression in M_s as a result of grain refinement has also been reported by a number of workers (e.g. Refs. 128-130, Chapter 5.3.1).

In addition to processing variables, the martensitic transformation kinetics of TiNi alloys can be influenced by the presence of impurities such as oxygen contamination. A small rise in the oxygen content causes a significant fall in the transition temperature[52] and also drastically increases the hardness[173]. However, in the present case the microhardness measurements of the spun ribbon using a load of 100 g give a mean value of 300 HV which is not considerably different from the 289 HV for the pre-sintered compact which was used as the starting material for the spinning process. By comparison with the data for the elemental blend compact, the oxygen contaminated wrought specimen gives a higher hardnes value

(370 HV) and consequently a lower M_s temperature (37°C). This indicates that the change in oxygen content during melt spinning is minimal and is insufficient to account for the large decrease in M_s observed.

9.7.3 Consolidation Phenomena in Equiatomic TiNi Alloy

The results obtained from this investigation have shown that sintering activity is greater in elemental powder compacts as compared to pre-alloyed particle specimens. While a temperature as low as 1000°C is sufficient to cause compositional homogenisation in elemental blend samples, a temperature in excess of 1050°c is required for sintering pre-alloyed powder specimens. In pre-alloyed powder, the dominant mechanism for sintering is self diffusion where the driving force is a decrease in surface energy, whereas in the elemental mixture compact, there is additional driving force promoting alloy formation. In the present study, the magnitude of these two driving forces have been derived using equations 4.9 and 4.10 (Chapter 4.3.2). The results (Appendix 9.1) indicate that the alloy formation energy is about four orders of magnitude greater. This makes it possible to sinter the elemental powder at a lower temperature. In the case of pre-alloyed powder, the individual particles have the same composition as that of the desired final product, consequently the alloy formation energy is non-existent. Similar results have been reported by Savitskii[90] in TiAl, and by Abkowitz[91] in Ti-6Al-4V (Chapter 4.3.2).

The results (Figure 9.16) from metallographic studies show that rapidly solidified pre-alloyed powder compacts densify during sintering which is in contrast with the increase in the amount of porosity experienced by elemental blend specimens. This has been explained in terms of the unequal interdiffusion rates of Ti and Ni and the occurrence of a transient liquid phase during the sintering of elemental blend samples (Chapter 7.3.2). In spite of the higher sintering temperature needed for the rapidly solidified pre-alloyed powder compacts, a finer grain size is observed (Figure 9.17) when compared to elemental blend samples. These results are consistent with those of other workers (e.g. Refs. 139-141, Chapter 5.4) on the resistance of RS material to grain coarsening. This resistance to grain growth of rapidly solidified samples has been related to particle-pinning of grain boundaries. The particles are known to result from the decomposition of the metastable phases, produced by rapid soldification, during subsequent heat treatment. It is likely that the decomposition of metastable phases is not the only factor responsible for the suppression of grain coarsening observed in the present work, since the hardness of the as-spun equiatomic TiNi ribbon is not significantly different from those of samples aged at temperatures up to 900°C (Figure 9.11). By contrast, the hardness values obtained from the sintered samples are considerably higher than that of the starting spun material (Figure 9.15). For example, the milled pre-alloyed powder compact sintered at 1150°C with 94% of full density gives an apparent hardness value of 454 HV as compared with a mean microhardness value of 300 HV for the as-spun ribbon. This suggests that oxygen contamination of the material took place during

the milling process. Thus, the presence of oxide particles in the ball milled pre-alloyed powder compact could be a contributing factor to the resistance to grain coarsening. As a result of oxygen contamination, the M_s temperature of the pre-alloyed specimen decreases further below room temperature to -30°C as compared with 16°C for the as-spun ribbon.

9.8 Summary

The results presented in this chapter have demonstrated that the melt spinning technique can be used to produce rapidly soldified equiatomic TiNi ribbons which are capable of being consolidated by cold compaction and sintering operations. Rapid solidification results in significant refinement of grain size due to the high undercooling experienced during solidification.

The high temperature phase of TiNi has the bcc CsCl structure with a lattice parameter a_o = 3.015 Å. The transformation temperature, M_s of the alloy is considerably depressed by rapid solidification processing, thus revealing the intermediate rhombohedral phase. The decrease in M_s has been correlated with the refined grain structure. It is also thought that the high dislocation density resulting from rapid solidification could be a contributing factor. The existence of an order-disorder reaction in equiatomic TiNi and its effect on M_s temperature have not been unambiguously confirmed. The M_s can be raised by ageing treatment. The occurrence of the cubic→rhombohedral transition near room temperature allows the spun ribbon to display a well defined shape memory behaviour.

The inherent high hardness of the RS material makes it impossible to produce compacts with green density levels comparable to those achieved with elemental blends. However, unlike the RS pre-alloyed powder compacts which densify during sintering, the densities of elemental powder samples decrease. This phenomenon is related to the difference in interdiffusion rates of Ti and Ni, and the occurrence of a transient liquid phase during the sintering of elemental blend compacts.

Due to the high magnitude of the alloy formation energy in TiNi, lower sintering temperature can be employed for elemental blends, which is in contrast to pre-alloyed powder. However, despite the need for a higher sintering temperature for RS pre-alloyed particles, the resulting grain size is finer.

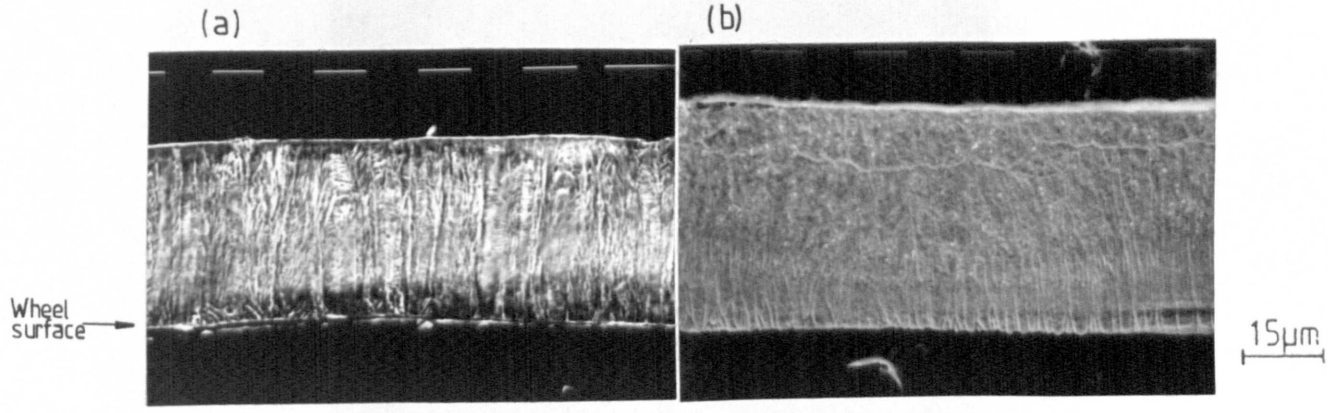

Figure 9.1 Scanning electron micrographs of rapidly soldified TiNi ribbon in the longitudinal cross-section.

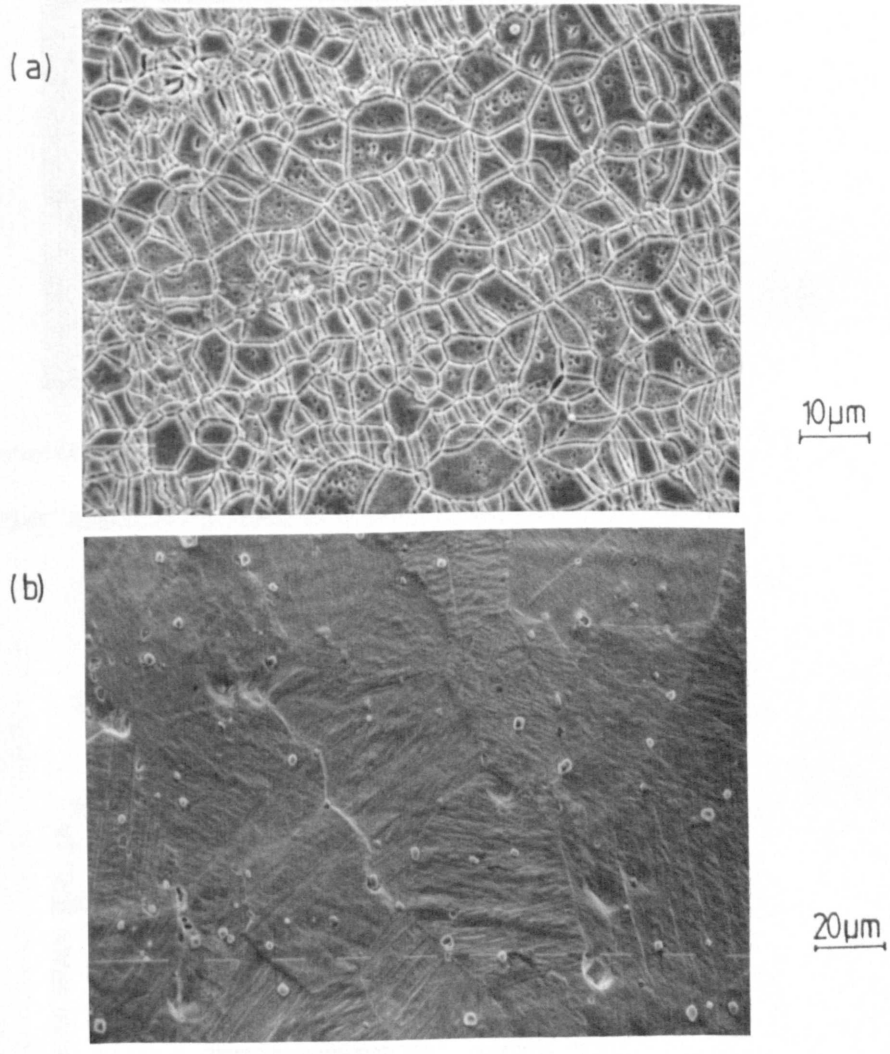

Figure 9.2 Microstructure of (a) a cross-section near the bottom surface of a spun TiNi ribbon and (b) wrought sample.

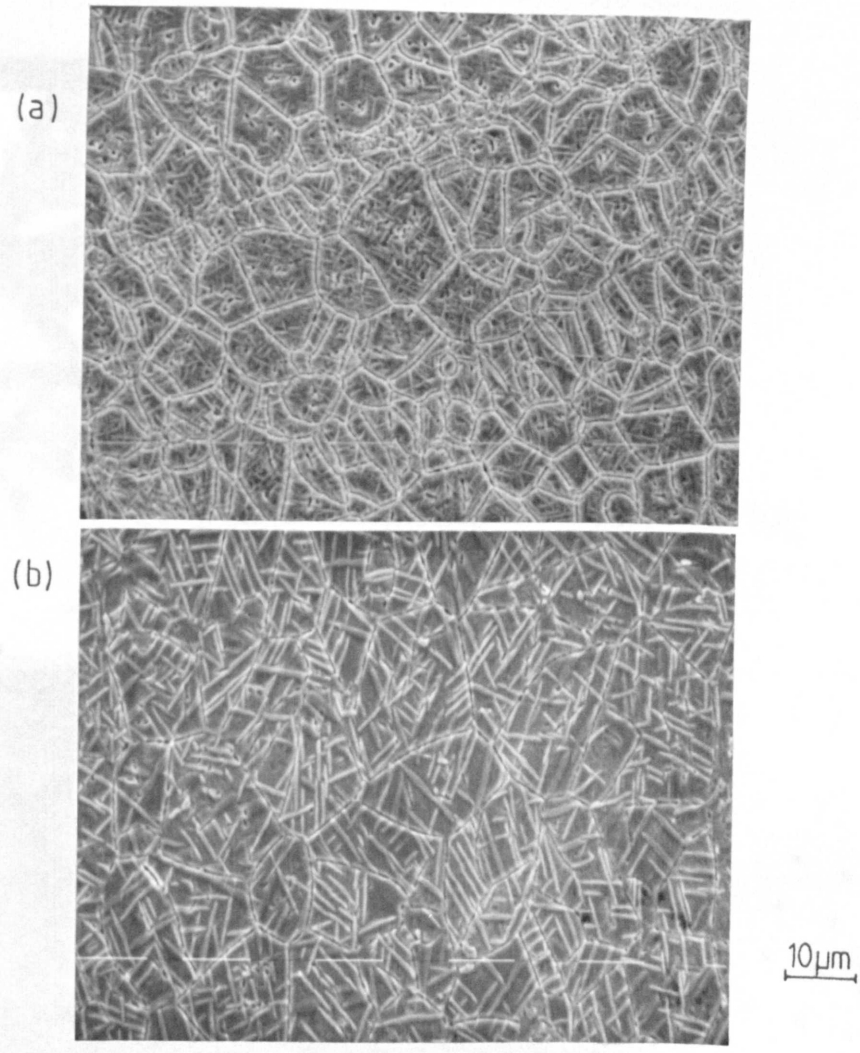

Figure 9.3 Microstructures of melt spun ribbon aged at 900°C for (a) 1 hour and (b) 5 hours.

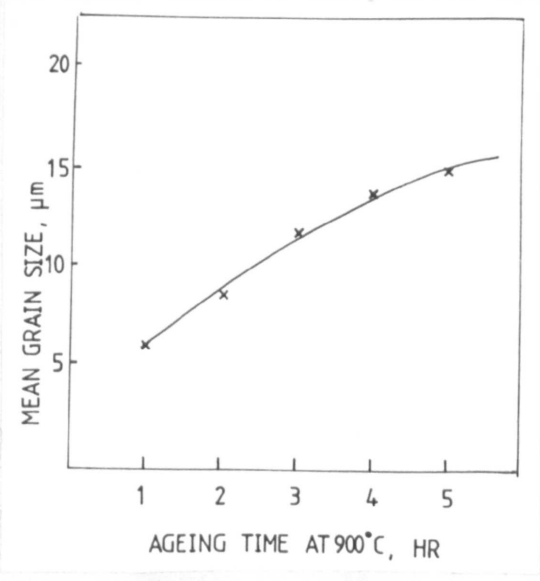

Figure 9.4 Variation of grain size with ageing time at 900°C for spun TiNi ribbon.

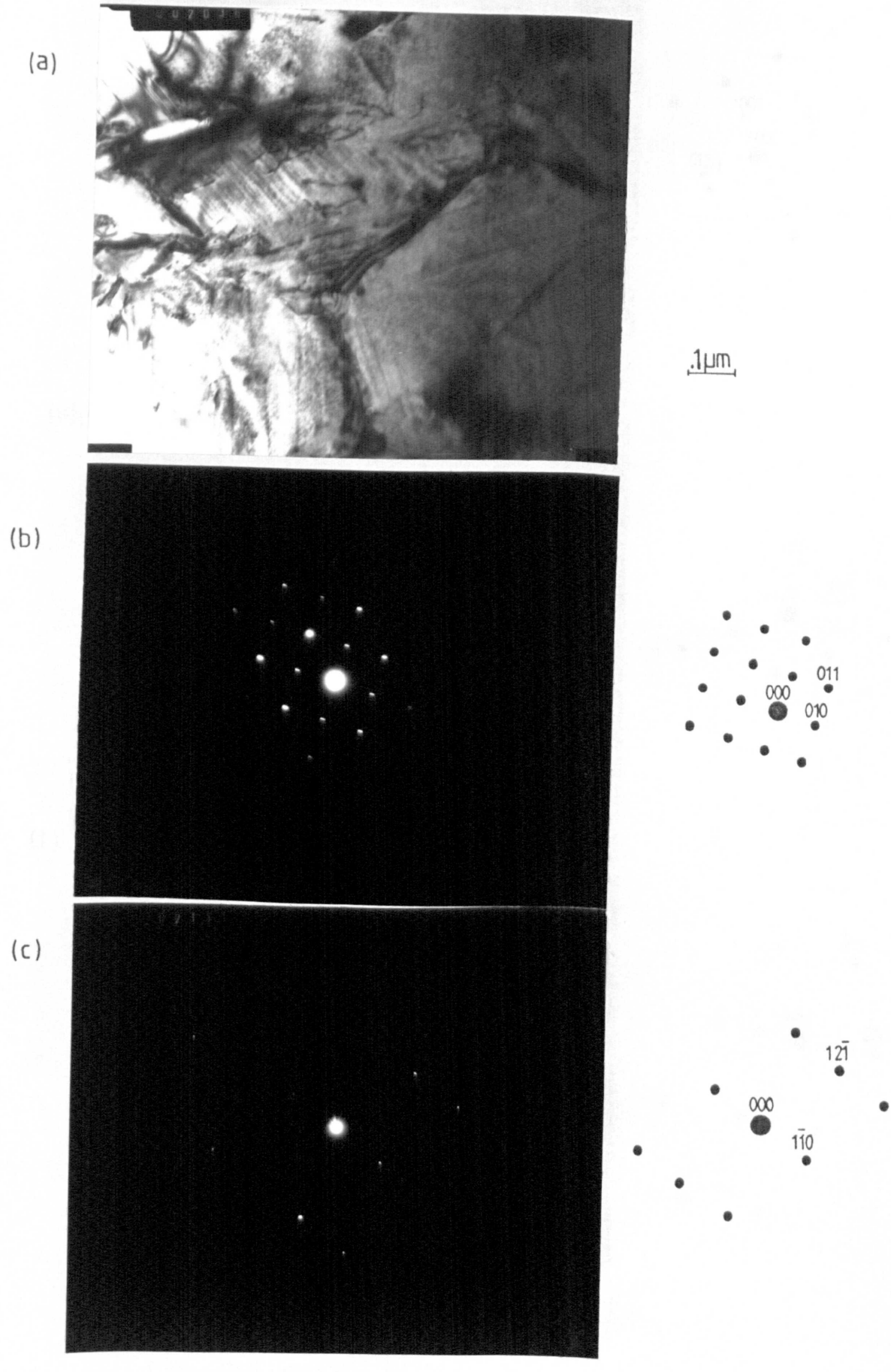
(a)
.1μm
(b)
011
000
010
(c)
12$\bar{1}$
000
1$\bar{1}$0

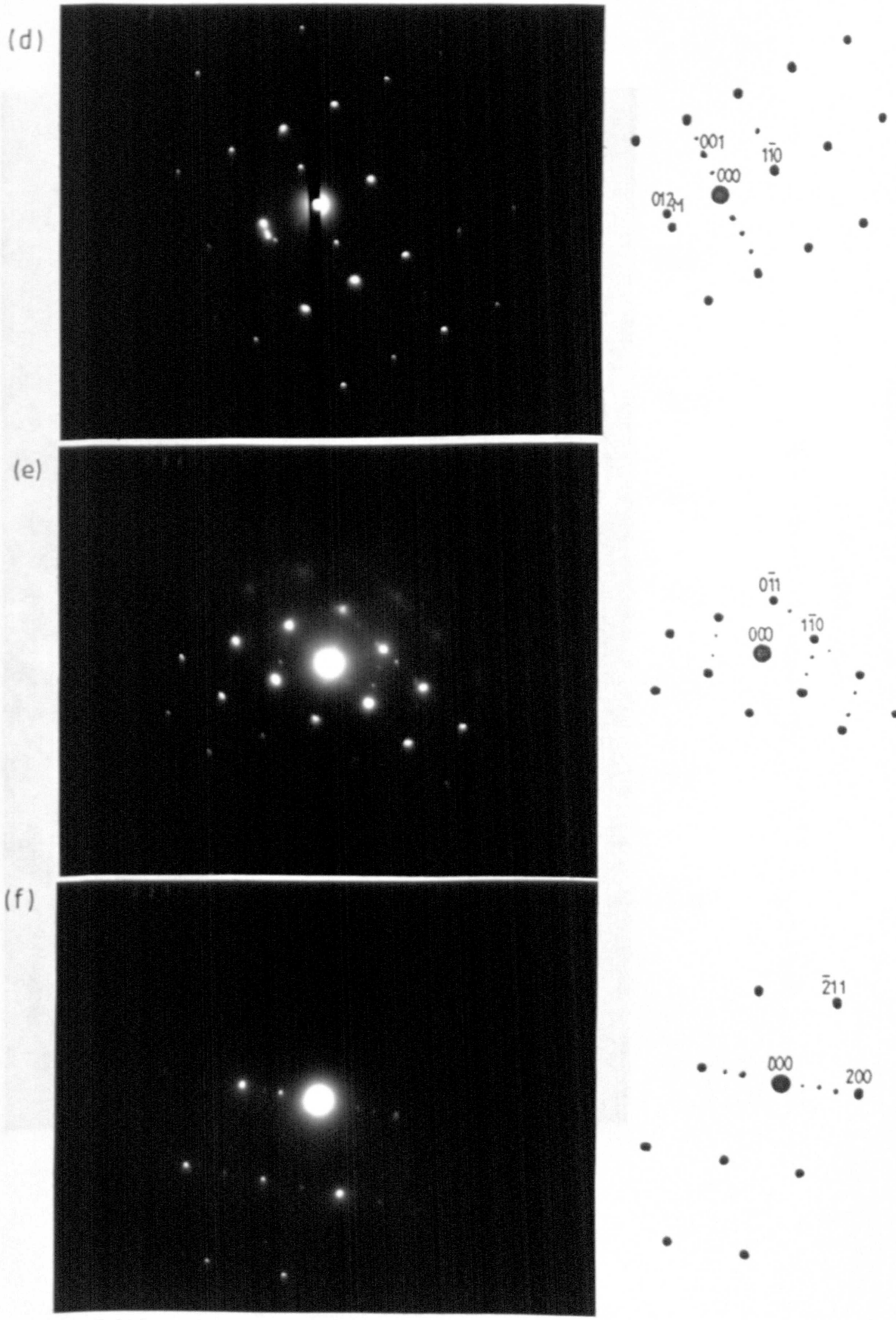

Figure 9.5 Bright field micrograph and electron diffraction patterns of rapidly solidified TiNi ribbon. The patterns b, c, d, e and f are respectively identified as $[100]_{B2}$, $[113]_{B2}$, $[110]_{B2}$, $[111]_{B2}$ and $[120]_{B2}$ zones of the CsCl type structure. The patterns corresponding to $[110]_{B2}$, $[111]_{B2}$ and $[120]_{B2}$ display some extra reflections indicating the presence of more than one phase.

Figure 9.6 X-ray powder diffraction patterns of

(a) as-spun TiNi ribbon, and

(b) heat treated (5 hr at 800°C) ribbon.

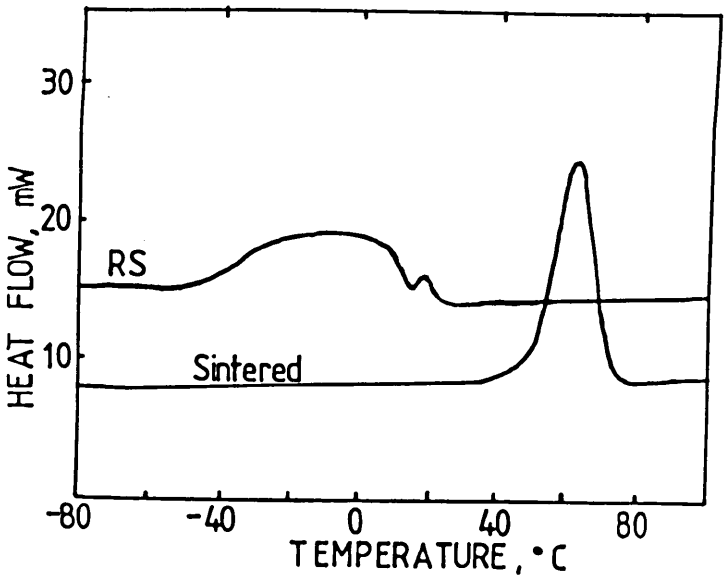

Figure 9.7 Differential scanning calorimetry cooling curves for spun ribbon and sintered specimen.

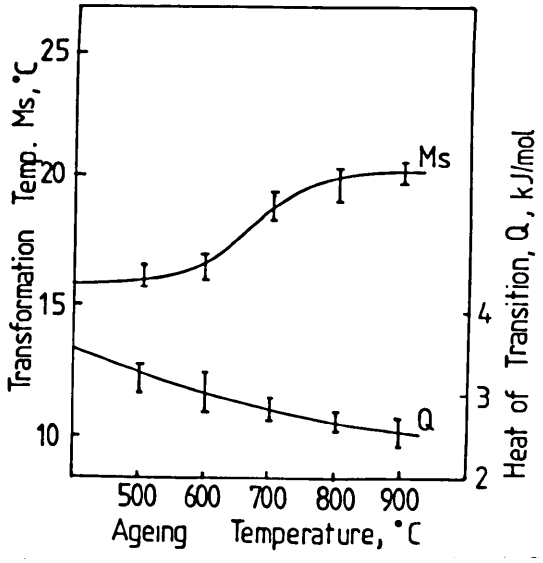

Figure 9.8 Effect of ageing temperature on the transformation temperature and heat of transformation of spun ribbon (ageing time - 1 hour).

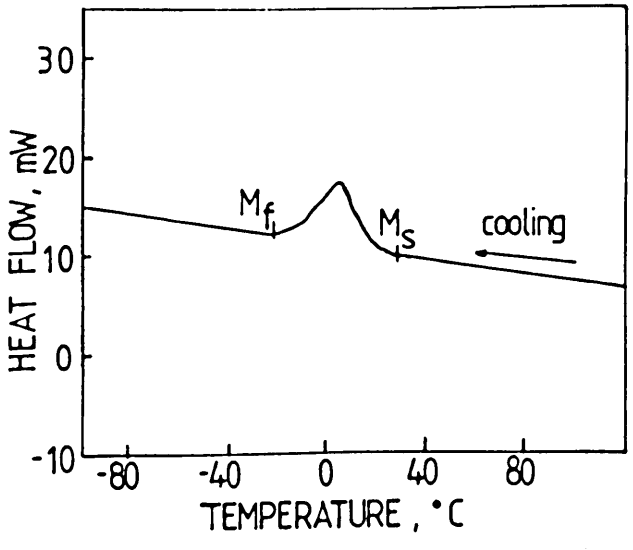

Figure 9.9 Differential scanning calorimetry curves for ribbon aged at 900°C for 1 hour.

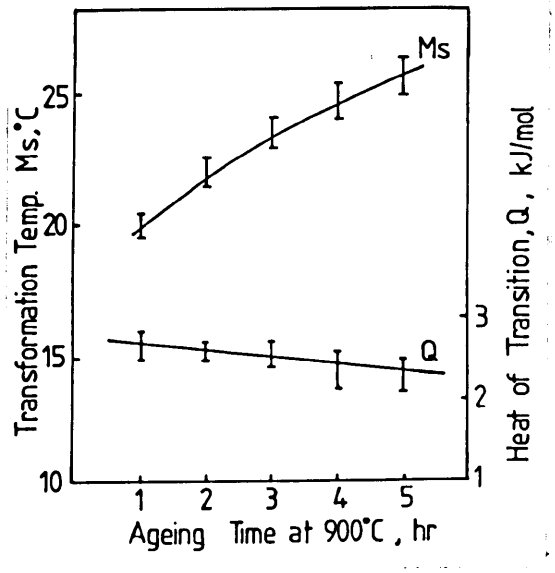

Figure 9.10 Effect of ageing time on the transformation temperature and heat of reaction of spun ribbon (ageing temperature 900°C).

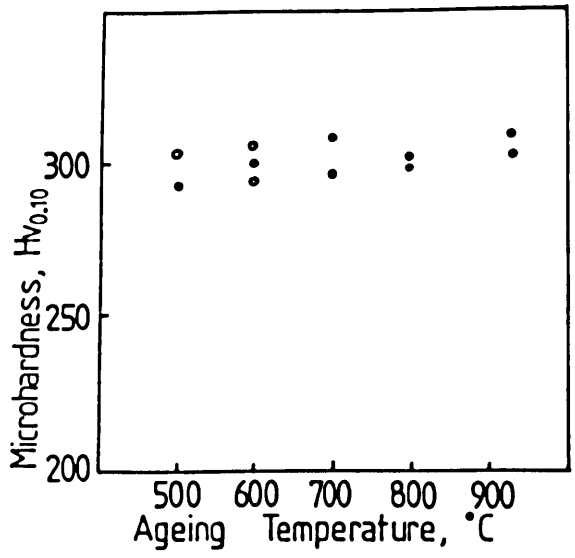

Figure 9.11 Influence of ageing temperature on the hardness of ribbon (ageing time - 1 hour).

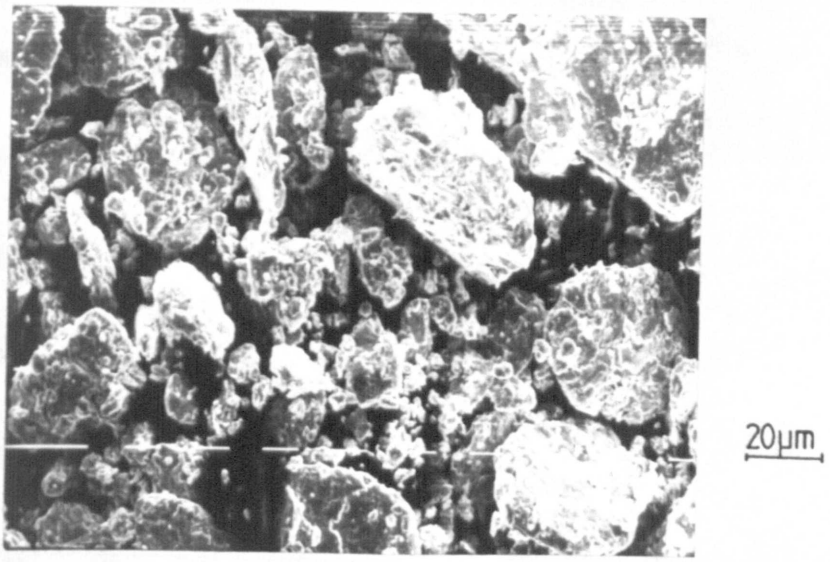

Figure 9.12 Scanning electron micrograph of milled powder.

(a) (b)

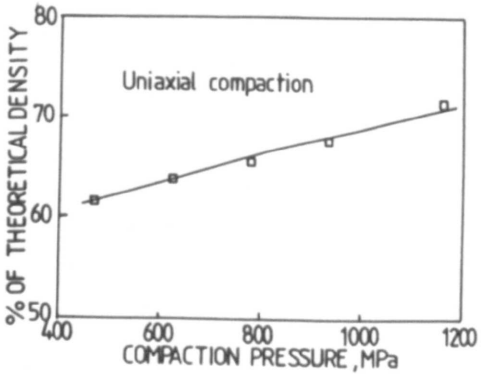

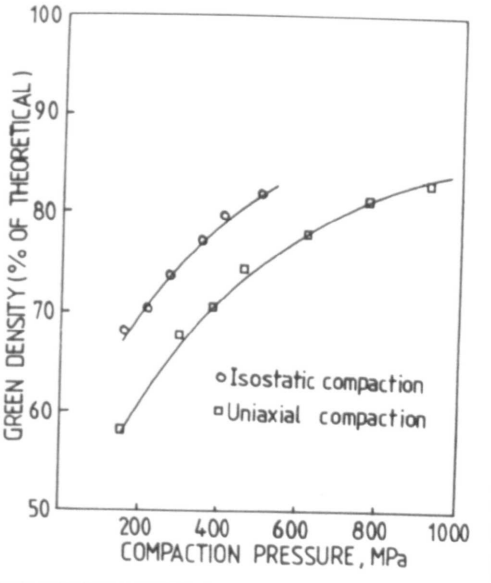

Figure 9.13 Compressibility curves for Ti-50 at-%Ni

(a) RS prealloyed powder prepared by uniaxial compaction

(b) elemental powder mixture processed by uniaxial and isostatic pressing.

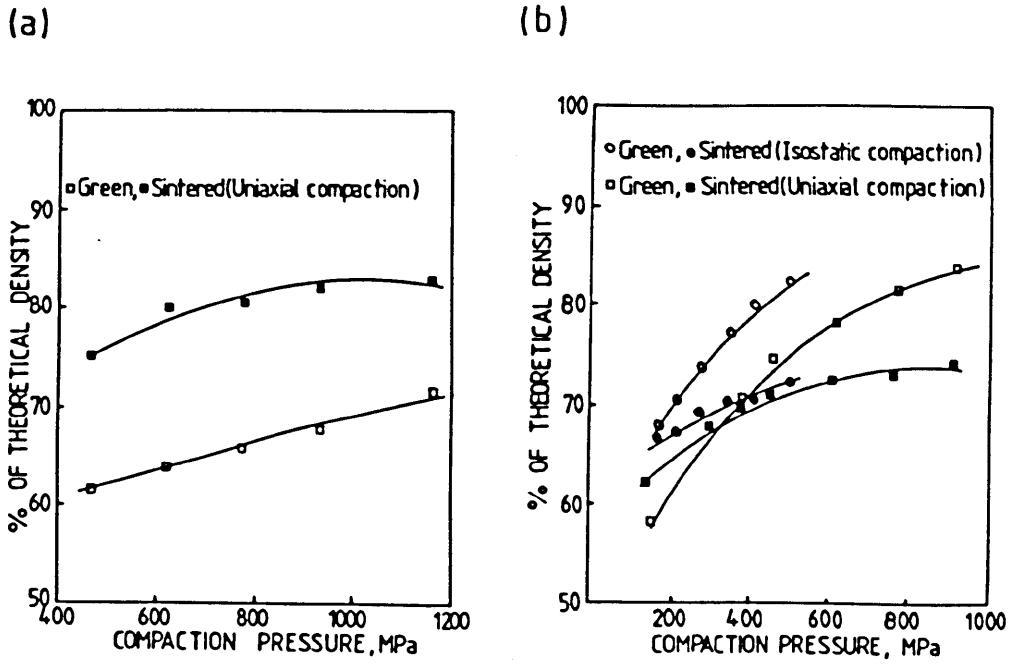

Figure 9.14 Comparison of green and sintered density curves for

(a) prealloyed particle compacts, 5 hours sintering at 1100°C

(b) elemental blend compacts, 5 hours sintering at 1000°C.

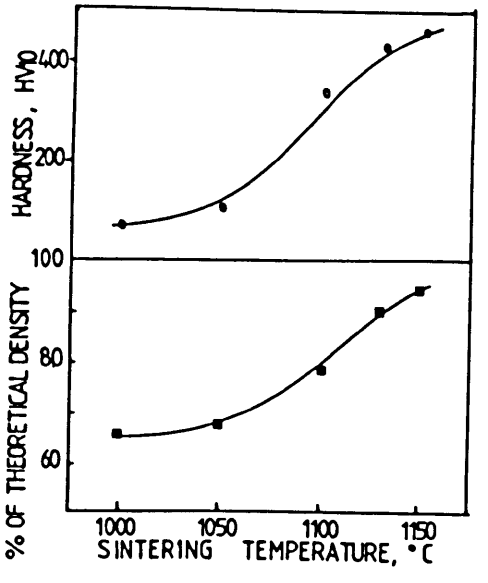

Figure 9.15 Variation of density and hardness with sintering temperature for prealloyed powder compacts pressed at 774 MPa and sintered for 5 hours.

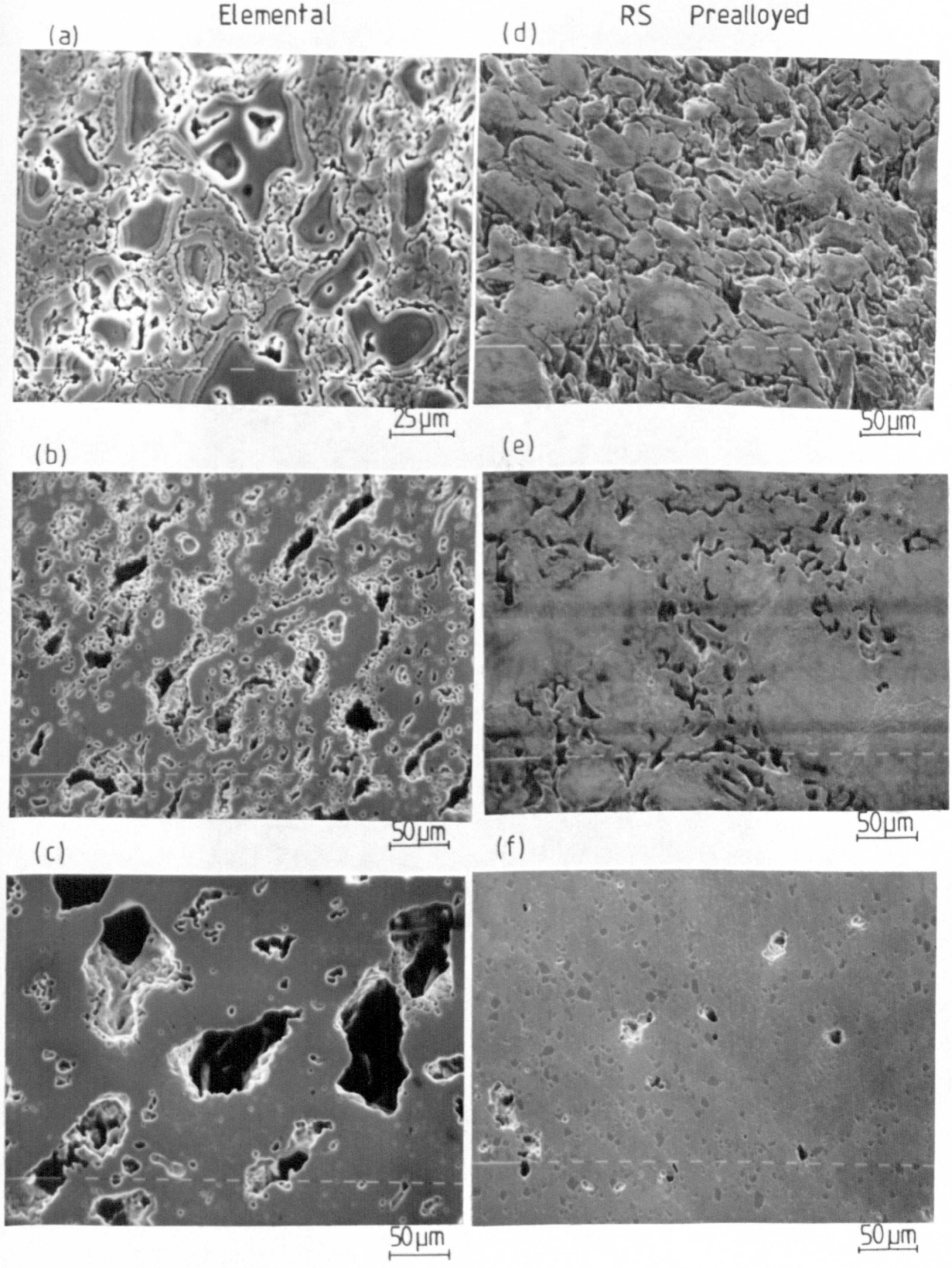

Figure 9.16 Microstructures of elemental powder compacts sintered at (a) 700°C, (b) 900°C, (c) 1000°C and prealloyed particle compacts sintered at (d) 1050°C, (e) 1100°C and (f) 1150°C.

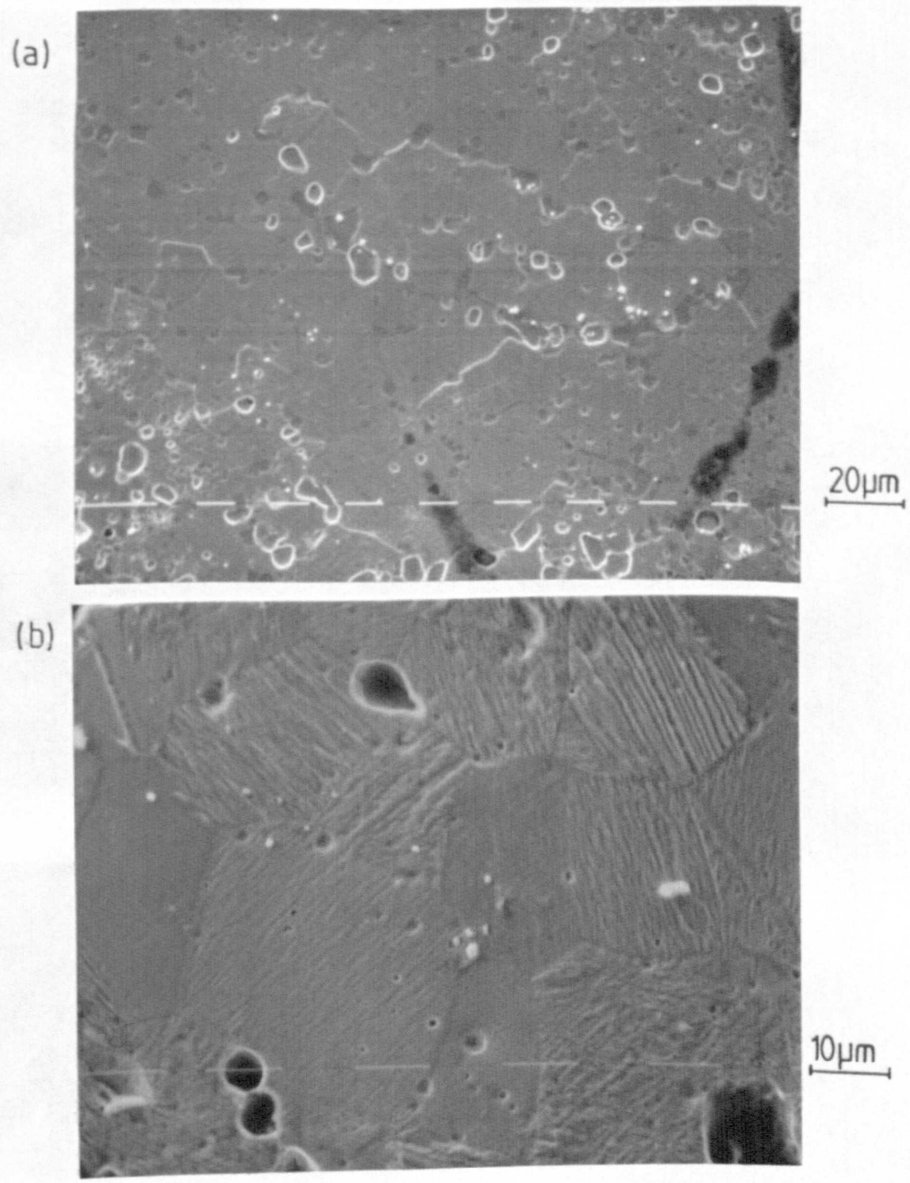

Figure 9.17 Scanning electron micrographs of (a) prealloyed (5 hours at 1120°C) and (b) elemental blends (5 hours at 1000°C) compacts showing the difference in grain size.

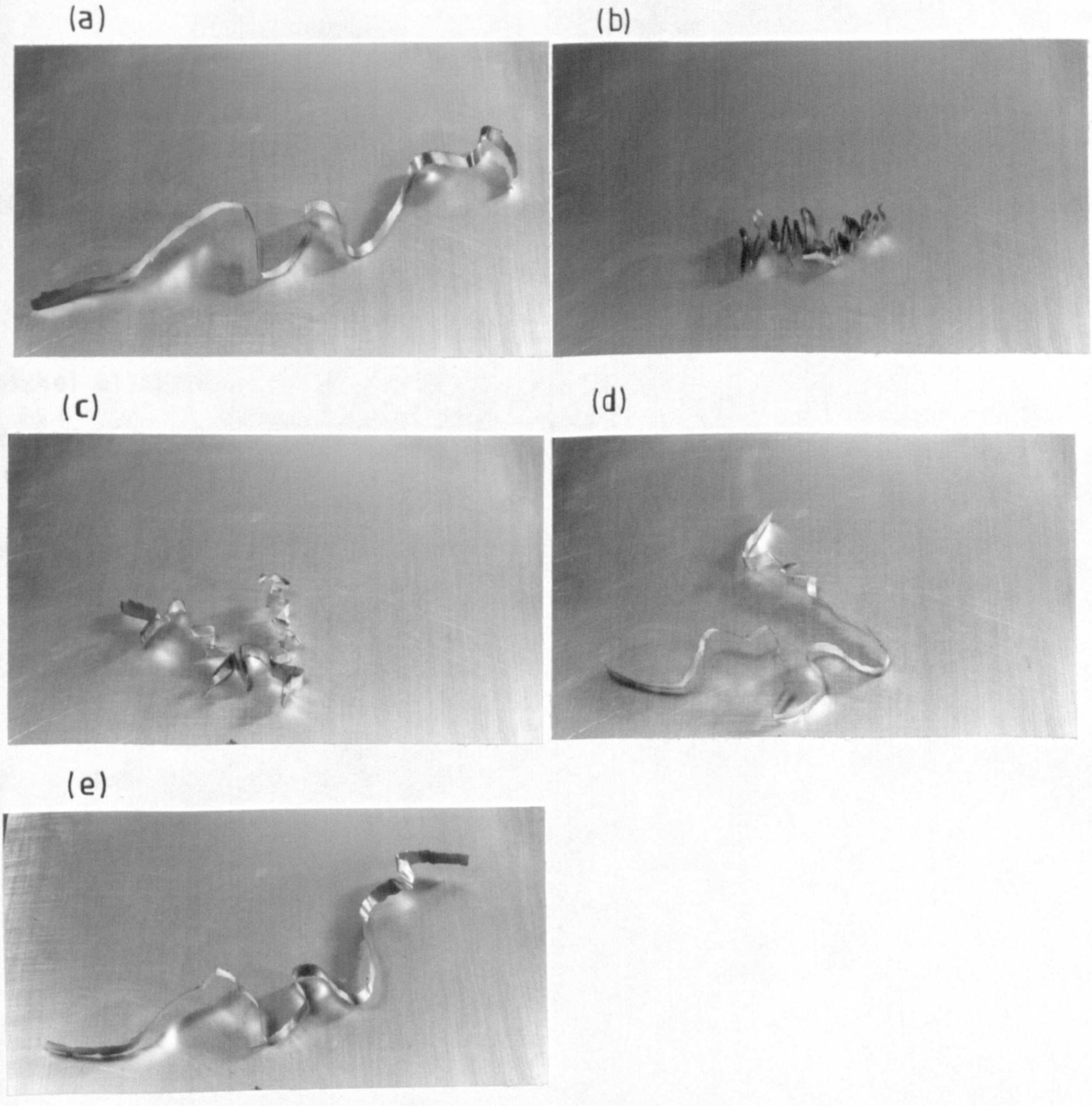

Figure 9.18 Photographs of melt spun TiNi ribbon showing the shape memory behaviour after deformation at room temperature and heating to about 120°C

(a) original shape

(b) deformed at room temperature and then heated to

(c) 65°C, (d) 90°C, and (e) 120°C.

CHAPTER 10

CONCLUSIONS AND SUGGESTIONS FOR FUTURE WORK

10.1 Conclusions

The results obtained in the present investigation on titanium-nickel alloys prepared by powder metallurgy and rapid solidification techniques allow the following deductions to be made:

1. Within a comparable range of compaction pressures higher green densities are achieved by cold isostatic pressing compared with uniaxial die compaction.

2. When there is a significant difference between the particle sizes of elemental powders, extensive segregation of particles occurs in uniaxial pressing, which can affect the nature of dimensional change experienced by the compact during the subsequent sintering operation.

3 As a result of the unequal interdiffusion rates of Ti and Ni greater porosity is formed in the sintered compacts compared to that in the as-pressed condition.

4. If sintering of an elemental Ti and Ni compact is performed in the presence of a transient liquid phase, the amount of porosity increases drastically, and the pore size is directly

proportional to the titanium particle diameter. Consequently the sintered density of compact decreases as the titanium particle size is raised.

5. Densification to near full density can be achieved by subjecting the elemental blend sintered compacts to hot isostatic pressing.

6. TiNi compound has a wide homogeneity range (49-54 at -% Ni) at high temperature (about 1000°C), but decreases as the temperature is lowered. Hence alloys of nickel rich composition can be quenched hardened.

7. The transformation temperatures of TiNi alloys containing excess amount of nickel are highly sensitive to cooling rate after solid state heat treatment. This is in contrast with specimens of equiatomic concentration. The transition temperature of TiNi alloy is lowered by thermal cycling.

8. An increase in the volume fraction of pores in pressed and sintered compacts reduces the equivalent load bearing cross section. Hence for a given load, TiNi specimens with a larger volume of pores will deform to a greater extent compared with a sample of higher density. Consequently the proportion of this strain (initial strain) recovered during heating through the reverse martensitic transformation temperature decreases with density.

The actual transformation strain of porous TiNi material normalised for differences in density is, however, not significantly different from that of wrought samples. The degree of strain recovery of the initial deformation can be enhanced by prestraining.

9. The chill block melt spinning technique can be employed to produce rapidly solidified TiNi ribbons which display the shape memory behaviour.

10. Rapid solidification results in significant grain refinement due to the high undercooling experienced by the material before solidification. The grain size of melt spun TiNi ribbon varies from 0.5 to 10 μm with a mean value of about 4 μm, indicating the high and non-uniform undercoolings within the ribbon during solidification. This is at least an order of magnitude smaller than those found in wrought samples.

11. The Martensitic transformation, M_s of TiNi alloy is significantly depressed by rapid solidification processing when compared to that of the pressed and sintered material which was used as the starting material for melt spinning. The decrease in M_s allows the intermediate rhombohedral phase to be observed. The M_s can be raised by heat treatment. This behaviour has been correlated with the refined grain structure of the spun ribbon.

12. The existence of a solid state order-disorder reaction in equiatomic TiNi and its effect on M_s have not been unambiguously confirmed in the present study.

13. The spun ribbons can be subsequently crushed to powder and consolidated into compacts by cold compaction and sintering operations. However, the inherent high hardness of the rapidly solidified materials makes it impossible to achieve similar green densities comparable to those of elemental blends over a comparable range of compaction pressures.

14. The milled RS prealloyed powder requires higher sintering temperatures than those necessary for elemental powders. The difference in sintering response of both materials has been related to the large magnitude of the TiNi alloy formation energy which is not applicable during the sintering of prealloyed powder compacts.

15. In spite of the need to sinter the RS powder compacts at much higher temperatures the grain size of these specimens is smaller than those found in elemental blend samples.

16. Prealloyed TiNi powder compacts densify during sintering whereas in the case of elemental blend samples the density decreases.

10.2 Suggestions for Future Work

The present work was designed to investigate the characteristics of Ti-Ni alloys produced by both powder metallurgy and rapid solidification techniques. The properties studied include the transformation behaviour, grain size, consolidation response, mechanical properties and the shape memory effect.

The results obtained have shown that extensive porosity remained in TiNi compacts prepared by compaction and sintering of elemental powders. The level of porosity was significantly reduced by HIPing the sintered compacts.

The work has also demonstrated that rapidly solidified prealloyed particulate of TiNi produced by melt spinning technique can be employed to process fine grained compacts with a low M_s temperature and fewer pores. In view of the ductile nature of the spun ribbon, however, only a fraction of the charge could be comminuted to powder. Improvements in the ribbon-powder conversion process yield would, in future perhaps, be best made by using the hydriding-dehydriding method described in Chapter 4.4. Ball milling in an inert atmosphere would minimize oxygen contamination.

An important feature observed in the RS prealloyed material is the relatively high hardness which prevented cold compaction to high green densities similar to those attainable with elemental powders. Also, since the individual particles of the prealloyed powder had the same composition as that of the desired final product, the absence of the energy for alloy formation means that a higher sintering temperature is required as compared with those for elemental blends. A possible alternative approach in the consolidation of the RS material would be to employ other techniques such as hot isostatic pressing, hot extrusion or dynamic compaction which allows processing at lower temperatures. Dynamic compaction and HIPing are similar in that there is very little mixing of the particles during

consolidation. By comparison, hot extrusion permits considerable interparticle mixing, and often results in a material with strong preferred crystallographic orientation. It would be most interesting to compare the consolidation characteristics of spun TiNi ribbons using these three processes.

The depression in M_s due to rapid solidification processing is significant since in some shape memory applications (such as the aircraft hydraulic coupling described in Chapter 3.1, M_s = -120°C[174]), it is desirable to produce materials with low M_s temperatures. Although a decrease in M_s can be achieved by increasing the nickel content in TiNi, it has been found that the presence of $TiNi_3$ in nickel rich alloys interferes with the shape memory performance of the material, hence this approach is not usually adopted[36]. Currently, the most common method of lowering the transformation temperature, of TiNi is the addition of small alloying elements such as Fe and Co[36,175].

Since RS processing can decrease the M_s temperature of TiNi without the need for alloying additions, further investigations into this area deserve attention. There are a number of processing parameters (e.g. wheel speed) which can influence the microstructure and properties of melt spun ribbon. For the purpose of the present work, all experimental variables were kept constant. It would be of interest to undertake a systematic study with the aim of determining the relationship between rapid solidification process variables and transformation characteristics of TiNi. Such work has been performed

by Wood and Shingu[130] on Cu-base shape memory alloys. The full potential of RS processing of TiNi alloys can be expected to be realised only when the effect of processing variables can be evaluated.

Annealing studies on spun TiNi ribbon at temperatures ranging from 500 to 900°C show that the M_s increases with time and temperature. At about 700°C, which is close to the apparent order-disorder temperature, a step-wise change is observed. However, since no superlattice reflections could be identified in the X-ray powder diffraction pattern for the ribbon which had been aged at temperatures above the ordering temperature range, it is not certain whether the observed rise in M_s is connected with ordering. It is anticipated that future work in this field would examine in further detail the effect of the degree of ordering on M_s temperature. It is known that electron diffraction is often more capable of detecting weak diffraction scattering than X-ray diffraction[42,179]. Hence subsequent work on ordering would perhaps be undertaken using a scanning transmission electron microscope equipped with a cooling stage such as the type employed by Hwang et al[164] on Ti-Ni-Fe alloys. Since the intensities of the extra diffraction spots relating to the rhombohedral phase in TiNi increase with a fall in temperature (Chapter 3.3), the use of a microscope with a cooling stage would allow the presence of any superlattice spot, due to ordering, to be unambiguously determined.

FIGURE CAPTIONS

Figure 2.1 Temperature dependence of the free energies of the parent (p) and martensitic (m) phases[13].

Figure 2.2 Schematic representation of the volume percentage of martensite as a function of temperature, showing transformation hysteresis loop[16].

Figure 2.3 Typical stress-strain curve for a shape memory alloy deformed at a temperature above A_f, showing pseudoelastic behaviour[13].

Figure 2.4 Variation of stress necessary to form martensite ($\sigma_{p \rightarrow m}$) and stress for plastic deformation of the matrix phase (σ_p) with temperature in CuZn single crystals[27].

Figure 2.5 Schematic stress-strain curve for a shape memory specimen deformed at a temperature below M_s.

Figure 3.1 Equiatomic region of Ti-Ni equilibrium diagram
(a) Duwez and Taylor, 1950[37]
(b) Margolin et al, 1953[39]
(c) Purdy and Parr, 1961[40]
(d) Wasilewski et al, 1971[41]

Figure 4.1 Schematic illustration of
(a) uniaxial die compaction
(b) cold isostatic compaction[64]

Figure 4.2 Typical pressure-density curve (uniaxial)[61].

Figure 5.1 Dependence of dendrite tip velocity on undercooling in nickel melts[116].

Figure 5.2 Chill block melt spinning.

Figure 5.3 Ribbon cross-sectional area A_r as a function of $d^2P^{1/2}V_s^{-1}$ for melt spun crystalline Sn-Pb and Al-(Fe, Mn)[119].

Figure 5.4 The dependence of eutectic cell spacing λ on growth velocity V_g for Al-Al_2Cu[116].

Figure 5.5 Dendrite arm spacing (o) for dendritic specimens and grain size (•) for both dendritic and non-dendritic specimens vs. degree of undercooling for Ni-25 wt % Cu-0.2 wt % Ni - 25 wt % Cu-0.2 wt % alloy[127].

Figure 5.6 Variation of M_s temperature and austenite grain size with austenitizing temperature for Fe-0.33%C-3.26%Ni-0.85%Cr-0.09%Mo alloy[128].

Figure 5.7 Quenched-in vacancy concentration as a function of inverse quenching temperature T for lead.

Figure 5.8 Yield and ultimate tensile strength of consolidated RS Ti-6Al-4V-1B and conventional Ti-6Al-4V as a function of temperature.

Figure 6.1 Geometry of tensile test piece
A = 3.44 ± 0.02, B = 20 ± 0.5, C = 54 ±0.5, W = 5.2 ± 0.5, R_1 = 15, R_2 = 2.6 (all dimensions in mm), (area = 23.65 mm^2).

Figure 7.9 Variation of dimensional change with titanium particle size for uniaxially processed compacts (774.4 MPa) and sintered at 1000°C for 5 hours.

Figure 7.10 Microstructures of (a) uniaxially pressed green compact showing extensive segregation of powder particles and (b) isostatically compacted specimen showing almost uniform distribution of powder particles. (c) Cross-section of metallographic observations.

Figure 7.11 Scanning electron micrographs of compacts sintered for 5 hours at (a) 600°C, (b) 700°C, (c) 800°C, (d) 900°C, and (e) 1000°C, illustrating the effect of sintering below ($\leq$ 900°C) and above (1000°C) the eutectic temperature on the morphology and distribution of pores.

Figure 7.12 Scanning electron micrographs of samples pressed at 774.4 MPa and sintered for 5 hours at 1000°C, showing the effect of titanium particle size on porosity. Mean particle size include (a) 82.5 μm, (b) 50 μm, and (c) 27.5 μm.

Figure 7.13 Variation of pore size with titanium particle size in compacts pressed at 774.4 MPa and sintered at 1000°C for 5 hours.

Figure 7.14 (a) Microstructure of Ti-Ni diffusion couple, annealed at 900°C for 72 hours, illustrating the presence of diffusional porosities in nickel rich region of diffusion zone;

(b) Concentration profile for Ni across the diffusion zone.

Figure 7.15 Scanning electron micrograph of HIPed compact.

Figure 7.16 A proposed model for describing the mechanism of dimensional changes during sintering below eutectic temperature.

(a) Schematic representation of segregated powder particles in uniaxially pressed compact;

(b) Expansion of compact due to diffusion of nickel atoms into titanium particles, and creation of diffusional porosities in prior nickel region (large arrows indicate direction of net flux of atoms and small arrows for expansion);

(c) Final structure illustrating the presence of skeleton pore network at prior nickel sites giving rise to radial expansion and densification in axial direction as a result of growth of necks between touching titanium particles

Figure 7.17 Schematic diagram of the sintering mechanism above the eutectic temperature

(a) Net nickel diffusion into titanium particles as in Figure 7.16 leaving diffusional porosity.

(b) After the formation of a transient liquid phase, penetration of liquid into capillaries occurs, causing overall expansion of compact, leaving pores behind on prior sites of titanium particles.

Figure 8.1 Variation of macrohardness with sintering temperature of compacts pressed at 503 MPa (isostatic) and 774.4 MPa (uniaxial) and sintered for 5 hours.

Figure 8.2 Dependence of hardness on titanium particle size for compacts pressed at 774.4 MPa and sintered for 5 hours at 1000°C.

Figure 8.3 Variation of microhardness with composition of water quenched (WQ) and furnace cooled (FC) Ti-Ni specimens.

Figure 8.4 Scanning electron micrographs of

(a) equiatomic TiNi specimen furnace cooled from 1000°C

(b) equiatomic TiNi specimen water-quenched from 1000°C

(c) Ti-54 at -%Ni sample furnace cooled from 1000°C

(d) Ti-54 at -%Ni sample water-quenched from 1000°C.

Figure 8.5 (a) Microstructure of Ti-54 at -%Ni furnace cooled from 1000°C;

(b) Ti X-ray image of (a);

(c) Ni X-ray image of (a).

Figure 8.6 Microstructures of Ti-54 at -% Ni specimens

(a) furnace cooled and (b) water quenched from 1000°C showing the presence of martensite plates in the slowly cooled sample (a).

Figure 8.7 Typical differential scanning calorimetry curves for a pressed and sintered Ti-50 at -% Ni sample showing the reversible transformation temperature points.

Figure 9.5 Bright field micrograph and electron diffraction patterns of rapidly solidified TiNi ribbon. The patterns b, c, d, e and f are respectively identified as $[100]_{B2}$, $[113]_{B2}$, $[110]_{B2}$, $[111]_{B2}$ and $[120]_{B2}$ zones of the CsCl type structure. The pattern corresponding to $[110]_{B2}$, $[111]_{B2}$ and $[120]_{B2}$ display some extra reflections indicating the presence of more than one phase.

Figure 9.6 X-ray powder diffraction patterns of
(a) as-spun TiNi ribbon, and
(b) heat treated (5 hr at 800°C) ribbon.

Figure 9.7 Differential scanning calorimetry cooling curves for spun ribbon and sintered specimen.

Figure 9.8 Effect of ageing temperature on the transformation temperature and heat of transformation of spun ribbon (ageing time - 1 hour).

Figure 9.9 Differential scanning calorimetry curves for ribbon aged at 900°C for 1 hour.

Figure 9.10 Effect of ageing time on the transformation temperature and heat of reaction of spun ribbon (ageing temperature 900°C).

Figure 9.11 Influence of ageing temperature on the hardness of ribbon (ageing time - 1 hour).

Figure 9.12 Scanning electron micrograph of milled powder.

Figure 9.13 Compressibility curves for Ti-50 at-%Ni

(a) RS prealloyed powder prepared by uniaxial compaction

(b) elemental powder mixture processed by unixial and isostatic pressing.

Figure 9.14 Comparison of green and sintered density curves for

(a) prealloyed particle compacts, 5 hours sintering at 1100°C

(b) elemental blend compacts, 5 hours sintering at 1000°C.

Figure 9.15 Variation of density and hardness with sintering temperature for prealloyed powder compacts pressed at 774 MPa and sintered for 5 hours.

Figure 9.16 Microstructures of elemental powder compacts sintered at (a) 700°C, (b) 900°C, (c) 1000°C and prealloyed particle compacts sintered at (d) 1050°C, (e) 1100°C and (f) 1150°C.

Figure 9.17 Scanning electron micrographs of (a) prealloyed (5 hours at 1120°C) and (b) elemental blends (5 hours at 1000°C) compacts showing the difference in grain size.

Figure 9.18 Photographs of melt spun TiNi ribbon showing the shape memory behaviour after deformation at room temperature and heating to about 120°C

(a) original shape

(b) deformed at room temperature and heated to

(c) 65°C, (d) 90°C, and (e) 120°C.

APPENDICES

APPENDIX 8.1

The relationship between stress and temperature is given by:

$$\frac{d\sigma}{dT} = \frac{\rho \Delta H}{\varepsilon_t T_o} \qquad \text{(Equation 2.5, Chapter 2)}$$

From the slope of stress-temperature data in Figure 8.11 (Chapter 8), $\frac{d\sigma}{dT}$ is found to be 1.050×10^6 Pa K^{-1}.

$$T_o = \frac{1}{2}(M_s + A_f) \qquad \text{(Equation 2.3, Chapter 2)}$$

The respective values of M_s, A_f and ΔH for sintered equiatomic TiNi are 79.2°C, 122°C and 3610 J mol^{-1} (data for the first cycle in Tables 8.1 and 8.2).

$\therefore$ T_o = 100.6°C i.e. 373 °K

The sintered density of sample = 4959 kg m^{-3}. Hence ε_t = 0.046 or 4.6%.

APPENDIX 9.1

For a binary system, the surface energy, G_s, in the green compact can be determined from

$$G_s = 3\left[\frac{M_a\gamma_a}{\rho_a r_a} + \frac{M_b\gamma_b}{\rho_b r_b}\right] \qquad \text{(Equation 4.9, Chapter 4)}$$

where M_a and M_b are the masses of the pure powders in moles; γ_a and γ_a, the surface free energies; ρ_a and ρ_b, the densities of the pure metals; and r_a and r_b, the particle radii.

For TiNi equiatomic composition with[176,177]
$\gamma_{Ti} = 1.7$ J m^{-2}, $\rho_{Ti} = 4.508$ Mg m^{-3}, mean particle radius,
$r_{Ti} = 32.5 \times 10^{-6}$ m, Atomic weight = 47.9
$\gamma_{Ni} = 1.86$ J m^{-2}, $\rho_{Ni} = 8.907$ Mg m^{-3}, $r_{Ni} = 2.5 \times 10^{-6}$ m,
Atomic weight = 58.71 (1 erg = 1×10^{-7} J).

$$\underline{G_s = 16.4 \text{ J mol}^{-1}}$$

From equation 4.10, the free energy of mixing, G_{mix} in a two-component system is given by:

$$\Delta G_{mix} = \Delta H - T\Delta S$$

For TiNi equiatomic alloy[178]
at 1200°K, $\Delta H = -14.27$ kJ mol^{-1}, $\Delta S = 131.4$ mol^{-1} K^{-1}
(1 cal = 4.186 J)

$$\underline{G_{mix} = 172 \text{ kJ mol}^{-1}}$$

REFERENCES

1. Buehler, W.J., Glifrich, J.V. and Wiley, R.C.:
J. Appl. Phys. 34 (1963), p.1475.

2. Chang, L.C. and Read, T.A.:
Trans. Met. Soc. AIME, 191 (1951), p.47

3. Burkart, M.W. and Read, T.A.:
Trans. Met. Soc. AIME, 197 (1953), p.1516.

4. Otsuka, K and Shimizu, K.:
Scripta Metall., 4 (1970), p.469.

5. Wayman, C.M.:
Scripta Metall., 5 (1971), p.489.

6. Tas, H., Delaey, L. and Deruyttere, A.:
Scripta Metall., 5 (1971), 1117.

7. Au, Y.K., and Wayman, C.M.:
Scripta Metall., 6 (1972), p.1209.

8. Dunne, D.P. and Wayman, C.M.:
Metall. Trans., 4A (1973), p.137.

9. Shimizu, K., and Otsuka, K.:
in "Shape Memory Effects in Alloys" (Ed. J. Perkins), Plenum Press, N.Y., 1975 p.59-87.

10. Wayman, C.M.:
in "Shape Memory Effects in Alloys" (Ed. J. Perkins), Plenum Press, N.Y., 1975, p.1-27.

11. Wayman, C.M.:

J. of Met., June (1980), p.129-137.

12. Burke, J.:

The Kinetics of Phase Transformations in Metals, Pergamon Press, London, 1965, p.196-213.

13. Delaey, L., Krishnan, R.V., Tas, H., and Warlimont, H.

J. Mat. Sci., 9 (1974), p.1521, 1536, 1545.

14. Dunne, D.P. and Wayman, C.M.:

Metall. Trans., 4A (1973), p.147.

15. Patel, J.R. and Cohen, M.:

Acta. Metall., 1 (1953), p.531.

16. Perkins, J., Edwards, G.R., Such, C.R., Johnson, J.R. and Allen, R.R.:

in "Shape Memory Effects in Alloys" (Ed. J. Perkins) Plenum Press, N.Y., 1975, p.273-303.

17. Wasilewski, R.J.:

Met. Trans., 6A (1975), p.1405

18. Kaufman, L., and Cohen, M.:

Prog. Metal. Phys. 7 (1958) p.165.

19. Tong, H.C. and Wayman, C.M.:

Acta. Metall. 22 (1974), p.887.

20. Warlimont, H.:

Mat. Sci. Eng. 25 (1976) p.139.

21. Nishiyama, Z.:
'Martensitic Transformation', Academic Press, London, 1978, p.232-336.

22. Cohen, M., and Wayman, C.M.:
in "Metallurgical Treatises", (Ed. J.K. Tien and J.F. Elliott), AIME, Warrendale, Pa. 1981, p.445-468.

23. Kurdjumov, G.V. and Khandros, L.G.:
Dokl, Acad. Nauk. USSR., 16 (1949) p.211.

24. Porter, D.A. and Easterling, K.E.:
Phase Transformation in Metals and Alloys, Alden Press, Oxford, 1981, p.382-440.

25. Owen, W.S.:
in Shape Memory Effects in Alloys (Ed. J. Perkins), Plenum Press, N.Y. 1975, p.305-325.

26. Nakanishi, N.:
in Shape Memory Effects in Alloys (Ed. J. Perkins), Plenum Press, N.Y., 1975, p.145-175.

27. Rodriguez, C. and Brown, L.C.:
in Shape Memory Effects in Alloys (Ed. J. Perkins), Plenum Press, N.Y., 1975, p.29-58.

28. Krishnan, R.V. and Brown, L.C.:
Metall. Trans. 4A (1973) p.432.

29. Perkins, J.:
Mat. Sci. Eng., 51 (1981) p.181.

30. Takei, F., Miura, T., Miyazaki, S., Kimura, S., Otsuka, K., and Suzuki, Y.:
Scripta. Metall. 17 (1983) p.987.

31. Mohamed, H.A. and Washiburn, J.:
J. Mat. Sci. 12 (1977) p.469.

32. Baker, C.:
Met. Sci. J., 5 (1971), p.92.

33. Wasilewski, R.J.:
in Shape Memory Effects in Alloys (Ed. J. Perkins), Plenum Press, N.Y. (1975), p.245-271.

34. Wayman, C.M., and Shimizu, K.:
Met. Sci. J. 6 (1972), p.175.

35. Buehler, W.J., and Wiley, R.C.:
Trans. ASM. 55 (1962) p.269.

36. Buehler, W.J. and Wang, F.E.:
Ocean Eng. 1 (1968), p.105.

37. Duwez, P. and Taylor, T.L.:
Trans. AIME., 188 (1950), p.1173.

38. Poole, D.U. and Hume-Rothery, W.:
J. Inst. Metals., 83 (1955), p.473.

39. Margoline, H., Ence, E., and Nielson, J.P.:
Trans. AIME., 197 (1953), p.243.

40 Purdy, G.R., and Parr, J.G.:
Trans. Met. Soc. AIME., 221 (1961), p.636.

41. Wasilewski, R.J., Butler, S.R., Hanlon, J.E., and Worden, D.:
Metall. Trans., 2A (1971) p.229.

42. Otsuka, K., Sanamura, T., and Shimizu, K.:
Phys. Stat. Sol. (A) 5 (1971), p.457.

43. Dautovich, D.P., and Purdy, G.R.:
Can. Met. Quart. 4 (1965), p.129.

44. Marcinkowski, M.J., Sastri, A.S., and Koskimaki, D.:
Phil. Mag. 18 (1968), p.945.

45. Hehemann, R.F. and Sandrock, G.D.:
Scripta. Metall. 5 (1971) p.801.

46. Michal, G.M. and Sinclair, S.:
Acta. Cryst. 37B (1981), p.1803

47. Buhrer, W., Gottardt, R., Kulik, A., Mercier, O. and Staub, F.:
J. Phys. F. Met. Phys. 13, (1983), p.77.

48. Ling, H.C. and Kaplow, H.:
Metall. Trans. 11A (1980) p.77.

49. Chandra, K., and Purdy, G.R.:
J. Appl. Phys., 39 (1968), p.2176.

50 Salamon, M.B., Meichle, M., Wayman, C.M., and Hwang, C.M.:
in "Modulated Structures - 1979", (Eds. J.M. Cowley, J.B.

Cohen, M.B. Salamon, and B.J. Wuensch) AIP. Con. Proc. Hawaii, No. 53, 1979, p.223.

51. Khachin, V.N., Paskal, Yu. I., Gunter, V.E., Monasevich, A.A., and Sivokha, V.P.:
Phys. Met. Metall. 46, (1979), p.49.

52. Wasilewski, R.M., Butler, S.R., and Hanlon, J.E.:
Met. Sci. J., 1 (1967), p.104.

53. Johnson, W.A., Domingue, J.E., and Reichman, S.H.:
in Proc. Int. Conf. on ICOMAT, (Eds. L. Delaey and M. Chandrasekaran), Leuven, Belguim, 1982, p.285.

54. Mukherjee, K., Sinclair, S., and Dahotre, N.B.:
Mat. Sci. Eng. 74 (1985), p.75.

55. Wang, F.E., De Savage, B.F., Buehler, W.J., and Hosler, W.R.:
J. Appl. Phys. 39, (1968), p.2166.

56. Sandrock, G.D., Perkins, A.J., and Hehemann, R.F.:
Metall. Trans., 2A (1971), p.2769.

57. Wayman, C.M., Cornelis, I., and Shimizu, K.:
Scripta. Metall. 6, (1972), p.115.

58. Samans, C.H.:
in "Metal Handbook", 1948 Edition (Ed. T. Lyman), 1948, p.47.

59. Plotkin, S. Ya., and Fridman, G.L.:
Sov. Powder Metall. Met. Ceramics, 13 (1974), p.1026.

60. Roll, K.M.:
in "Metals Handbook", Ninth Edition, Volume 7, ASM, Metals Park, Ohio, 1984, p.14.

61. Sands, R.L. and Shakespeare, C.R.:
"Powder Metallurgy - Practice and Applications", George Newnes, London, 1966, p.1-107.

62. Wollaston, W.H.:
Phil. Trans. Roy Soc. 119 (1829) p.1.

63. Lenel, F.V. and Ansell, G.S.:
in "Metallurgical Treatises" (Ed. J.K. Tien and J.F. Elliott), Warrendale, Pa., AIME 1981, p.345-360.

64. Lenel, F.V.:
"Powder Metallurgy - Principles and Applications": Princeton, New Jersey, 1980, p.99-307.

65. Shapiro, I., and Kolthoff, I.M.:
J. Phys. Colloid Chem. 51 (1947) p.215.

66. Heckel, R.W.:
Trans. Metl. Soc. AIME 221 (1961) p.1001.

67. Nazmy, M.Y., and Abdel-Azim, M.S.:
Powder Metall. 17 (1974) p.13

68. Morgan, V.T. and Sand, R.L.:
Metallurgical Reviews - J. Inst. Met. 134 (1969), p.87.

69. Marshall, P.R.:
Metals and Materials with Metallurgical Reviews 2 (1968), p.183.

70 Hewitt, R.W., Wallace, W., and De. Malherbe, M.C.:
Powder Metallurgy 17 (1974), p.1.

71. Hausner, H.H.:
in "Sintering - New Developments", (Ed. M.M. Ristric), Elsevier, N.Y., 1979, p.1.

72. Kaysser, W.A., Huppman, W.J., and Petzow, G.:
Powder Metall. 23 (2) (1980) p.86.

73. Tabeshfar, K. and Chadwick, G.A.:
Powder Metall. 2 (1) (1984) p.19.

74. Kuczynski, G.C.:
in "Proc. Inter. Conf. in Powder Metallurgy" (W. Leszynski), Interscience, N.Y., 1960, p.11-30.

75. Avner, S.H.:
"Introduction to Physical Metallurgy", McGraw-Hill, London, p.605-632.

76. Frenkel, J.J.:
Physics, USSR, 9 (1945), p.385.

77. Nabarro, F.R.N.:
"Report on a Conference on the Strength of Materials, The Physical Soc., London, 1948, p.75.

78. Kuczynski, G.C.:

J. Appl. Phys. 20 (1949) p.1160.

79. Kuczynski, G.C.:

Trans. AIME 185 (1949) p.169.

80. Moser, J.B., and Whitmore, D.H.:

J. Appl. Phys. 31 (1960) p.488.

81. Kingery, W.D., and Berg, M.:

J. Appl. Phys. 26 (1955) p.1205.

82. Herring, C.:

J. Appl. Phys. 21 (1950) p.437.

83. Alexander, B.H., and Baluffi, R.W.:

Acta. Metall. 5 (1957) p.666.

84. Ashby, M.F.:

Acta. Metall. 22 (1974) p.275.

85. Friedrich, E. and Schatt, W.:

Powder Metall. 23 (1980) p.193.

86. Brett, G.J. and Seigle, L.:

Acta. Metall. 14 (1966) p.575.

87. Hirth, J.P.:

in "Proceedings of the Conference on the Relation Between Structure and Mechanical Properties of Metals", London, 1963, p.218.

88. Roman, O.V., Kumar, J.V., Vityaz, P.A., Fridmann, G.R. and Smirnova, T.A.:
in Sintering - New Developments (Ed. M.M. Ristic) Elsevier, N.Y., 1979, p.82.

89. Smigelskas, A.D., and Kirendall, E.O.:
Trans. Am. Inst. Mining Met. Engrs. 171 (1947) p.130.

90. Savitskii, A.P.:
Poroshk. Metall. 7 (1980) p.62.

91. Abkowitz, S.:
in "Progress in Powder Metallurgy", Vol. 30, 1974, Metal Powder Industries Federation, Princeton, N.J.

92. Kingery, W.D.:
J. Appl. Phys. 30, (1959), p.301.

93. Fleming, R.P.H.:
in "Modern Dev. in Powder Metall." (Ed. H.H. Hausner) vol. 12, 1980, p.439.

94. Huppmann, W.J. and Riegger, H.:
Acta. Metall. 23 (1975) p.965.

95. Hansen, M. and K. Anderko:
in "Constitution of Binary Alloys" McGraw-Hill, N.Y., 1958.

96. Price, G.H.S., Smithells, C.J., and Williams, S.W.:
J. Inst. Met. 62 (1938) p.239.

97. Yoon, D.N., and Huppman, W.J.:
Acta. Metall. 27 (1979) p.973.

98. Froes, F.H., Eylon, D., Eichelman, G.E., and Burte, H.M.:
J. Met., Feb. 1980, p.47.

99. Kelto, C.A., Kosmal, B.A., Eylon, D., and Froes, F.H.:
J. Met., Aug. 1980, p.17.

100. Froes, F.H. and Smugeresky, J.E. (Ed.)
"Titanium Powder Metallurgy", Warrendale, PA, AIME, 1980.

101. Roberts, P.R. and Loewenstein, P.:
in "Titanium Powder Metallurgy", (Ed. F.H. Froes, and J.E. Smugeresky), Warrendale, Pa, AIME, 1980, p.21.

102. Pond, R.B., Maringer, R.E. and Mobley, C.E.:
in "New Trends in Materials Processing", ASM, Metals Park, Ohio, 1974, p.128-164.

103. Froes, F.H. and Eylon, D.:
in "Metal Handbook", 9th Edition, Vol.7, ASM, 1984, p.164.

104. Froes, F.H., and Pickems, J.R.:
J. Met. Jan., 1984, p.14.

105. Petrunko, A.N., Galitsky, N.V., Pampushko, N.A.:
in "Titanium 80 - Science and Technology" (Eds. F.H. Froes, and J.E. Smugeresky), AIME, Warrendale, Pa, 1980, p.189.

106. Mahaja, Y., Eylon, D. and Froes, F.H.:
in "Titanium Powder Metallurgy" (Eds. F.H. Froes, and J.E. Smugeresky), AIME, Warrendale, Pa, 1980, p.189.

107. Boyer, R.R., Magnuson, J.E., and Tripp, J.W.:
in "Titanium Powder Metallurgy", (Eds. F.H. Froes, and J.E. Smugeresky), AIME, Warrendale, Pa, 1980, p.203.

108. Abkowitz, S.:
in "Titanium Powder Metallurgy", (Eds. F.H. Froes, and J.E. Smugeresky), AIME, Warrendale, Pa, 1980, p.291.

109. Andersen, P.J., and Eloff, P.C.:
in "Titanium Powder Metallurgy" (Eds. F.H. Froes, and J.E. Smugeresky), AIME, Warrendale, Pa, 1980, p.175.

110. Duwez, P., Willens, R.H., and Klement, W.:
J. Appl. Phys, 31, (1960), p.1136.

111. Boettinger, W.J., Coriell, S.R. and Sekerka, R.F.:
Mat. Sci. Eng. 65, (1984), p.27.

112. Flemings, M.C. and Schiohara, Y.:
Mat. Sci. Eng. 65 (1984), p.157.

113. Jones, H. and Suryanarayana, C.:
J. Mat. Sci. 8 (1973), p.705.

114. Jones, H.:
J. Mat. Sci. 19 (1984), p.1043.

115. Jones, H.:
in "Rapid Solidification Processing, Principles and Technologies' (Eds. R. Mehrabian, Kear, B.H. and Cohen, M.), Baton Rouge, Claitors, 1977, p.28.

116. Jones, H.:
"Rapid Solidification of Metals and Alloys", Monograph 8, The Institution of Metallurgists, Whetstone, London, 1982.

117. Boettinger, W.J., and Perepezko, J.H.:
in "Proc. of Symposium on Rapidly Solidified Crystalline Alloys", Northeast Regional Meeting of TMS - AIME, Morristown, N.J., 1985.

118. Cohen, M., Kear, B.H. and Mehrabian, R.:
in "Rapid Solidification Processing: Principles and Technologies, II", (Eds. R. Mehrabian, B.H. Kear, and M. Cohen), Baton Rough, Claitor's, 1980, p.1.

119. Charter, S.J.B., Mooney, D.R., Cheese, R. and Cantor, B.:
J. Mat. Sci. 15 (1980) p.2658.

120. Davis, H.A.:
in "Rapidly-Quenched Metals III", Ed. B. Cantor, The Metal Society, London, 1978, Vol.1, p.1-22.

121. Maringer, R.E., and Mobley, C.E.:
in "Rapid Solidification Processing: Principles and Technologies", (Ed. R. Mehrabian et al) Baton Rouge, Claitors, 1977, p.208.

122. Liebermann, H.H.:
Mat. Sci. Eng. 43 (1980), p.203-210.

123. Chattopadhyay, K., Ramineni, A.P., and Ramachandrarao, P.:
J. Mat. Sci. 15 (1980), p.797.

124. Anantharaman, T.R., and Suryanarsyana, C.:
J. Mat. Sci. 6 (1971), p.1111.

125. Mehrabian, R.:
in "Rapid Solidification Processing: Principles and Technologies" (eds. R. Mehrabian et al), Baton Rouge, Claitors, 1977, p.9.

126. Walker, J.L.:
in "Physical Chemistry of Process Metallurgy", (Ed. G.R. St. Pieere), AIME, N.Y., 1961, p.845-853.

127. Skolianos, S., Liu, P.S., and Kattamir, T.Z.:
in "Proc. Conf. on Grain Refinement in Castings and Welds", (Eds. Abbaschian and S.A. David), Metallurgical Society of AIME, Warrendale, Pa, 1983, p.97-116.

128. Sastri, A.S. and West, D.R.F.:
J. Iron and Steel Inst., 203, (1965), p.138.

129. Inokuti, Y. and Cantor, B.:
J. Mat. Sci. 12 (1977), p.946.

130. Wood, J.V. and Shingu, P.H.:
Metall. Trans. 15A (1984) p.471.

131. Henderson, B.:
Defects in Crystalline Solids, Edward Arnold, London, 1972, p.136-161.

132. Rastogi, P.K. and Mukherjee, K.:
Metall. Trans. 1 (1970), p.2115.

133. Thomas, G., and Willens, R.H.:
Acta. Metall. 12 (1964), p.191.

134. Wood, J.V., and Honeycombe, R.W.K.:
J. Mat. Sci. 9 (1974) p.1183.

135. Smallman, R.E.:
"Modern Physical Metallurgy", Butterworths, London, 1970, p.375-387.

136. Wood, J.V., Mills, P.F., Bingham, J.K., and Bee, J.V.:
Metall. Trans. 10A (1979), p.575.

137. Tadaki, T. and Shimizu, K.:
Trans. JIM 11 (1970) p.44.

138. Perkins, J.:
Metall. Trans. 13A (1982) p.1367.

139. Suga, M., Goss, J.L., Olson, G.B., and Vander Sande, J.B.:
in "Rapid Solidification Processing: Principles and Technologies II", (Eds. R. Mehrabian, Kear, B.H., and Cohen, M.) Baton Rouge, Claitors, 1980, p.364.

140. Slaughter, E.R. and Das, S.K.:
ibid, p.364.

141. Gagg, C., Bee, J.V. and Wood, J.V.:
in "Rapidly Quenched Metals", (Eds. S. Steeb and H. Warlimont), Elsevier, N.Y., 1985, p.1747.

142. Ray, R. and Clemm, R.:
Metal Powder Report, April 1986, p.261.

143. Haynes, R.:
in "Reviews on the Deformation Behaviour of Materials", Freund, London, 1981, p.9-101.

144. Nazmy, M.Y., and Abdel-Azim, M.S.:
Powder Metall., 19 (2), (1976), p.60.

145. Cyunczyk, A.:
Powder Metall. Int., 11 (1979), p.162.

146. Tabesfar, K. and Chadwick, G.A.:
Powder Metall. 27 (1) (1984) p.19.

147. James, B.A.:
Powder Metall. 28 (3) (1985) p.121.

148. Majima, K. and Sohama, Y.:
J. Jpn. Soc. Powder Metall. 29 (1982), p.127.

149. Aksenov, G.I., Drozdov, I.A., Sorokin, A.M., Chernov, D.B., and Atyakshev, Yu.A.:
Powder Metall. Met. Ceram. 20 (5) (1981) p.340.

150. Kuczynski, G.C. and Zaplatynski, I.:
J. Met. 8 (1956) p.215.

151. Taylor, H.G.:
Powder Metall. (6) (1960) p.87.

152. Lindskog, P.:

Powder Metall. 19 (2) (1976) p.79.

153. Sevensson, L.E., and Engstrom, U.:

Powder Metallurgy (4) (1979) p.165.

154. Khaleghi, M. and Haynes, R.:

Powder Metall. 28 (4) (1985), p.217.

155. Elliott, J.E.:

Metallurgia, January (1959), p.17.

156. Berner, D., Exner, H.E. and Petzow, G.:

in "Modern Developments in Powder Metallurgy", (Eds. H.H. Hausner, and W.E. Smith), Metal Powder Industries Federation, Princeton, N.J., 1974, p.237.

157. Melton, K.N., and Mercier, O.:

Acta Metall. 29 (1981), p.393.

158. Pascoe, K.J.:

"An Introduction to the Properties of Engineering Materials", Van Nostrand, Reinhold, London, 1978, p.205.

159. Hamiuddin, M.:

Powder Metallurgy International 16 (6) (1984), p.257.

160. Suzuki, T. and Uehara, S.:

in "Titanium 80", Ed. H. Kimura and O. Izumi, AIME, Warrendale, Pa, 1980, p.1255.

161. Suzuki, T.:

Trans. Jap. Inst. Met. 14 (1973), p.31.

162. Perkins, J., and Muesing, W.E.:

Met. Trans, 14A (1983), p.33.

163. Nirsch, P.B., Howie, A., Nicholson, R.B., Pashley D.W. and Whelan, M.J.:

Electron Microscopy of Thin Crystal, Robert E. Krieger, New York, 1977, p.516.

164. Hwang, C.M., Meichle, M., Salamon, M.B., and Wayman, C.M.:

Phil. Mag. 47A (1983) p.9.

165. Zijkstra, S.R., Beijer, J. and Klostermann, J.A.:

J. Mat. Sci. 9 (1974), p.145.

166. Ling, H.C. and Kaplow, R.:

Metall. Trans. 12A (1981), p.101.

167. Otsuka, K. Sawamura, T., Shimizu, K and Wayman, C.M.:

Metall. Trans. 2A (1971), p.2583.

168. Nishida, M. and Honma, T.:

Scripta. Metall. 18 (1984), p.1293.

169. Wang, F.E., Buehler, W.J., and S.J. Pickart.:

J. Appl. Phys, 36 (1965) p.3232.

170. Wang, F.E.:

J. Appl. Phys. 44 (1973), p.3010.

171. Zijderveld, J.A., de Lange, R.G. and Verbraak, C.A.:
Mem. Sci. Rev. Met. 63 (1966), p.885.

172. Hirano, K. and Ouchi, K.:
J. Japan Inst. Metals. 32 (1968), p.613.

173. Roger, S.E.:
Powder Metall. 7 (1961), p.249.

174. Schetky, L.M.:
Scientific American 241 (5) (1979) p.74.

175. Eckelmeyer, K.H.:
Scripta. Metall. 10 (1976), p.667.

176. Jones, H.:
Met. Sci. J. 5 (1971), p.15.

177. Kubaschewski, O., Evans, E.L.L., and Alcock, C.B.:
"Metallurgical Thermochemistry", Pergamon, London, 1967, p.220-237.

178. Barin, I., Knacke, O, and Kubaschewski, O.:
"Thermochemical Properties of Inorganic Substances-Supplement", Dusseldorf, Germany, 1977, p.484.

179. Michal, G.M., Moine, P., and Sinclair, R.:
Acta Metall. 30 (1982) p.125.